4-2016

Double optical feedback and PT-symmetry breaking induced nonlinear dynamics in semiconductor lasers

Joseph S. Suelzer
Purdue University

PURDUE UNIVERSITY
GRADUATE SCHOOL
Thesis/Dissertation Acceptance

This is to certify that the thesis/dissertation prepared

By Joseph Sean Suelzer

Entitled
Double Optical Feedback and PT-Symmetry Breaking Induced Nonlinear Dynamics in Semiconductor Lasers

For the degree of Doctor of Philosophy

Is approved by the final examining committee:

Gautam Vemuri Chair	Zhe-Yu Ou
David D. Nolte	
Le Luo	
Yogesh N Joglekar	

To the best of my knowledge and as understood by the student in the Thesis/Dissertation Agreement, Publication Delay, and Certification Disclaimer (Graduate School Form 32), this thesis/dissertation adheres to the provisions of Purdue University's "Policy of Integrity in Research" and the use of copyright material.

Approved by Major Professor(s): Gautam Vemuri

Approved by: Horia I. Petrache 4/14/2016

Head of the Departmental Graduate Program Date

DOUBLE OPTICAL FEEDBACK AND PT-SYMMETRY BREAKING INDUCED NONLINEAR DYNAMICS IN SEMICONDUCTOR LASERS

A Dissertation

Submitted to the Faculty

of

Purdue University

by

Joseph S. Suelzer

In Partial Fulfillment of the

Requirements for the Degree

of

Doctor of Philosophy

May 2016

Purdue University

West Lafayette, Indiana

To my parents and my wife Deanna

ACKNOWLEDGMENTS

First I would like to thank my advisor, Gautam Vemuri, who has given me both the freedom and the support to mature as a scientist. He has continually reminded me that each "problem" in lab, whether expected or unexpected, is an opportunity to learn. This advice has extended outside of the lab - helping me to acquire the skills and the outlook for my profession after graduation. It has been a real joy working with him.

It has also been a pleasure collaborating with and learning from Yogesh Joglekar. His meticulous approach to problems and genuine interest in student's questions has inspired me. I am grateful for his patience and attention when responding to any of my questions.

I would like to thank Le Luo, David Nolte, and Jeff Ou for serving as my committee members and providing helpful feedback over the years.

I am indebted to Ricardo Decca for all of his help over the years. His encouragement and advice reinforced my decision to continue my graduate work toward a Ph.D. degree. I have been grateful (most of the time) ever since.

I am grateful for all the administrative help, in particular Juli Craft who has helped in more ways than I can name.

The friendships with graduate students here at IUPUI were an unexpected joy. This motley crew has helped in so many areas - from physics discussion, to building garden beds, to borrowing lab equipment, and offering so many opportunities for laughter. I almost forgot to mention the "excellent" Indian and Chinese food. I would like to thank the senior students (Prashant, Derek, and Merrell) for their advice which was (sometimes) heeded and those who started with me or continue to accompany me (Edwin, Brad, Wen, Ji, Leo, Xiaoling, Andy, Jake, and Muchuan). I

am also grateful for the assistance in our lab, especially Blake Johnson and all of the high school students.

I would like to thank Horia Petrache for his inspiring PHYS600 course and engaging philosophical discussions. Whether or not I agreed with the "conclusions" of these discussions, they were an impetus to return to my research with a renewed vigor and wonder. I always enjoyed Marvin Kemple's courses, which were not only entertaining but a reminder that our work is fun. Most of all I am grateful for his question, "how's life?".

Without Bruce Ray the "basement" would not function. I cannot count the number of times I locked myself out of the lab and found Bruce still in his office. In particular, his service to the department and students is inspiring.

I apologize to anyone who I have forgotten. There have been so many people who have helped me to live this adventure more intensely and for that I am extremely grateful.

Finally, I want to thank the homestead - my wife Deanna and children. Not once did Deanna ask me when I was going to graduate and find a "real" job... Actually, I regret not tracking the frequency of this question to determine its bounded value. Truly without her this journey would not have been so beautiful. She has supported and encouraged me, while raising three children - currently 1, 3, and 4 years old. I am still unsure how she survived. At this point, I would like to thank our friends and neighbors (Floyd, Jess, Esme, and Jemima) for reminding us that we are taken care of and loved. I would like to thank Leo and Silvia who told me to "have fun" as I walked out the door for work. Theresa whose curiosity and boldness to try new things is an inspiration. Lastly, the baby to come who has encouraged me to hurry up and graduate.

TABLE OF CONTENTS

Page

LIST OF TABLES vii

LIST OF FIGURES viii

SYMBOLS xiii

ABBREVIATIONS xiv

ABSTRACT xv

1 Introduction to Optical Feedback 1
1.1 Historical Introduction 1
1.2 Characteristics of the SCL and optical feedback 3
1.3 Fundamental studies and applications of SCL dynamics 5
1.3.1 Applied Research 6
1.4 Our Contribution 7
1.5 Outline 9

2 Rate equations for a semiconductor laser subject to optical feedback . . . 10

3 Semiconductor Laser subject to two filtered optical feedbacks 13
3.1 Introduction 13
3.2 Experimental Setup 15
3.3 Detection of frequency fluctuations 17
3.4 Theoretical model 18
3.5 Experimental and numerical results 20
3.5.1 Controlled frequency oscillations 20
3.5.2 Bifurcation analysis 29
3.6 Conclusions 30

4 Effects of Quantum Noise on the Dynamics 32
4.1 Introduction 32
4.2 Model 33
4.3 Results: a period doubling route to chaos 36
4.3.1 Influence of noise 40
4.4 Effects of the filter bandwidth on the dynamics 49
4.4.1 Feedback from an intermediate and narrow filter 50
4.4.2 Feedback from an intermediate and wide filter 55
4.5 Discussion and conclusion 59

Page

5 Parity-Time Symmetry Breaking in Delay Coupled SCLs 62
5.1 Introduction 62
5.2 Rate Equations 66
5.3 Theoretical Results 68
5.3.1 $\tau = 0$ 68
5.3.2 $\tau = 100$ and $\theta\tau = 2\pi m$ 72
5.3.3 $\tau = 100$ and $\theta\tau$ varies 74
5.4 Experimental Design 76
5.5 Experimental Procedure 78
5.5.1 Temperature Variation 78
5.6 Experimental Results 79
5.6.1 Varying the coupling strength 85
5.7 PT-transition and Phase Locking 87
5.8 Pump Current Variation 92
5.9 Conclusion 97

6 Summary 99

REFERENCES 102

VITA 109

LIST OF TABLES

Table Page

4.1 The parameter values for a typical SCL which are used in the simulations (unless otherwise specified). 37

5.1 The parameter values for a typical SCL that are used in the simulations (unless otherwise specified). 67

LIST OF FIGURES

Figure Page

1.1 Representation of the transmission function of a spectral filter: a change in frequency represented by $\Delta\nu$ results in a change in the intensity represented by ΔI 8

3.1 Schematic of the experimental set-up. DL: diode laser; BS: beam splitter; OI: optical isolator; M: mirror; G: glass plate; HWP1, HWP2: half-wave plates; PBS: polarizing beam-splitter; PDA, PDB, PDC: Photodiodes. . 16

3.2 Experimentally measured RIN spectra when the feedback is provided by only (a) cavity 1, and (b) cavity 2. 21

3.3 Experimentally measured RIN spectra depicting the change in frequency oscillations as the ratio of feedbacks from the cavities is varied. Spectra recorded (a) at approximately equal feedback strengths from the two cavities, (b) when the feedback strength from cavity 1 is larger than that from cavity 2, and (c) when the feedback strength from cavity 2 is larger than that from cavity 1. 22

3.4 With the fundamental cavity frequencies $f_{\text{ext1}} = 75$ MHz and $f_{\text{ext2}} = 131.4$ MHz and at equal feedback strengths from the two cavities, a weighted average frequency between the second harmonic of cavity 1 and the fundamental frequency of cavity 2 is seen in the experimentally observed spectrum with feedback rates $\kappa_1 = \kappa_2 = 0.0045$, time delays $\tau_1 = 1250$, $\tau_2 = 680$, filter bandwidths $\Lambda_1 = \Lambda_2 = 0.012$, and detunings $\Delta_1 = \Delta_2 = -0.007$. 24

3.5 With the fundamental cavity frequencies $f_{\text{ext1}} = 70.2$ MHz and $f_{\text{ext2}} = 189.3$ MHz, and at equal feedback strengths from the two cavities, a weighted average frequency between the third harmonic of cavity 1 and the fundamental frequency of cavity 2 is seen in the experimentally observed spectrum with feedback rates $\kappa_1 = \kappa_2 = 0.0045$, time delays $\tau_1 = 1341$, $\tau_2 = 445$, filter bandwidths $\Lambda_1 = \Lambda_2 = 0.012$, and detunings $\Delta_1 = \Delta_2 = -0.007$. 25

3.6 For the laser subject to a single FOF, (a) experimentally measured frequency spectrum, and (b) numerically simulated matching spectrum, with feedback rate $\kappa_1 = 0.01$, time delay $\tau_1 = 1248$, filter bandwidth $\Lambda_1 = 0.012$ and detuning $\Delta_1 = -0.013$. 26

Figure Page

3.7 For the laser subject to two FOFs, experimentally measured spectrum at the feedback ratio $\kappa_2 : \kappa_1 = 1 : 4$ 26

3.8 Frequency spectra showing period doubling of the weighted average frequency: experimentally measured with time delays $\tau_1 = 862$, $\tau_2 = 740$, filter bandwidths $\Lambda_1 = \Lambda_2 = 0.01$, detunings $\Delta_1 = \Delta_2 = -0.007$, and feedback rates $\kappa_1 = 0.016$, $\kappa_2 = 0.008$. 27

3.9 Frequency spectra showing a weighted average at 110.2 MHz between the fundamental of one cavity and the period doubled frequency of the other cavity: experimentally observed with feedback rates $\kappa_1 = 0.003$, $\kappa_2 = 0.0018$, time delays $\tau_1 = 734$, $\tau_2 = 222$, filter bandwidths $\Lambda_1 = 0.012$, $\Lambda_2 = 0.003$, and detunings $\Delta_1 = \Delta_2 = -0.007$. 28

3.10 With time delays $\tau_1 = 1333$, $\tau_2 = 793$, feedback rate $\kappa_2 = 0.003$, filter bandwidths $\Lambda_1 = \Lambda_2 = 0.005$, detunings $\Delta_1 = \Delta_2 = -0.007$, and asymmetry parameter $\eta = 1$, the spectral bifurcation diagram of the two-FOF laser as the feedback rate κ_1 is varied: (a) the three-dimensional view, and (b) the density map of the combined laser intensity spectra. 29

4.1 The schematic shows a semiconductor laser (SCL) subject to optical feedback from two external cavities. The outer cavity (1) is formed by the SCL and the mirrors (M1, M2, and M3). The inner cavity (2) is formed by the SCL, beam splitters (BS2 and BS3), and mirror (M3). Each cavity contains a Fabry-Perot resonator acting as a spectral filter, which can be modified by changing the reflectivity or spacing of the filter mirrors. This in turn changes the bandwidth, Λ. The detuning, Δ, is altered by adjusting the pump current. The delay-times, τ_1 and τ_2, are increased or decreased by lengthening or shortening the cavities. 34

4.2 Deterministic (a) and stochastic [(b),(c)] density plots of the period doubling route to chaos when the feedback strength κ_1 from cavity 1 is increased. The bandwidth and detuning are fixed at $\Lambda_1 = 1$ GHz and $\Delta = -0.5$ GHz, otherwise all other parameters are recorded in Table 5.1. f_{I-IV} are the frequencies discussed in this text which differ significantly in the stochastic period doubling route. Note that (c) contains the stochastic spectra extended out to 5 GHz. 39

4.3 Deterministic (a) and stochastic (b) plots of the frequency $\omega(t)$ time-series (1), the phase-plane of ω_n and η (2), and the rf spectrum (3) showing a fundamental frequency of $f_{fun} \approx 123$ GHz. The plots are calculated when the feedback is injected solely from cavity 2 ($\kappa_1 = 0$ GHz). The rf spectra (a4) and (b4) are extended out to 6 GHz in order to depict the undamping of the ROs seen in the time-series (b1). 41

Figure Page

4.4 Deterministic (a) and stochastic (b) plots of the frequency $\omega(t)$ time-series (1), the phase-plane of ω_n and η (2), and the RIN spectrum (3) when the feedback strength is κ_1 =0.32 GHz. The deterministic time-series captures a transient behavior toward a steady-state behavior. 42

4.5 First return maps for feedback strength of κ_1 =0.32 GHz showing both the stochastic (red triangle) and deterministic (blue circle) locations of ω_{max}. 44

4.6 Deterministic (a) and stochastic (b) plots of the frequency $\omega(t)$ time-series (1), the phase-plane of ω_n and η (2), and the rf spectrum (3) when the feedback strength is κ_1 =0.97 GHz. The deterministic time-series and phase-portrait show periodic behavior with a frequency of $f_{RO} \approx 2.5$ GHz, which is shown in the extended spectra (a4) and (b4). 46

4.7 Deterministic (a) and stochastic (b) plots of the frequency $\omega(t)$ time-series (a1 and b1), the phase-plane of ω_n and η (a2 and b2), and the rf spectrum (a3 and b3) when the feedback strength is κ_1 =4.52 GHz. 47

4.8 First return maps for feedback strength of (a) κ_1 =4.52 GHz, (b) κ_1 =4.84 GHz, and (c) κ_1 =5.16 GHz showing both the stochastic (red triangle) and deterministic (blue circle) values. 48

4.9 Deterministic (a) and stochastic (b) density plots of the amplitude of the spectrum as a function of changing bandwidth, Λ_1. The density plots correspond to the spectra for (1) $I_L(t)$, (2) $I_{F_1}(t)$, (3) and $I_{F_2}(t)$. Λ_2 is fixed at 1 GHz and the two feedback rates are kept constant at $\kappa_1 = 3$ GHZ and $\kappa_2 = 0.8$ GHz. 51

4.10 (1) Intensity time series $I_L(t)$, (2) phase portraits (η, P), and (3) rf spectrum in the absence of noise (a) and in the presence of noise (b) for a bandwidth of $\Lambda_1 \approx 32$ MHz and detuning $\Delta_1 = -32$ MHz. 53

4.11 (1) Intensity time series $I_L(t)$, (2) phase portraits (ω_n, η), and (3) rf spectrum in the absence of noise (a) and in the presence of noise (b) for a bandwidth of $\Lambda_1 = 50$ MHz and detuning $\Delta_1 = -50$ MHz. 54

4.12 Deterministic (a) and stochastic (b) density plots of the amplitude of the spectrum as a function of the increasing feedback rate, κ_1. The spectra are calculated with the with the parameters mentioned in Table 5.1 except the following: $\Lambda_1 = 20$ GHz and $\Delta_1 = -5$ GHz. (1) Spectra of the intensity of light from laser, $I_L(t)$ and (2) spectra from the light through filter 2, $I_{F_2}(t)$. 56

Figure Page

4.13 Three subplots are produced using the intensity of light through filter 2, $I_{F_2}(t)$. The times series (1), phase portrait $\omega_n, \eta(t)$ (2), and rf spectrum (3) are calculated for the feedback rates [(a) and (b)] $\kappa_1 = 0$ GHz and [(c) and (d)] $\kappa_1 = 1.7$ GHz. 58

5.1 (a) Trajectories of the eigenvalues when $\kappa = 0.1$ for zero delay ($\tau = 0$). (b) Simulations of the SCL intensities (I_1 and I_2) when $\kappa = 0.02$ and $P_1 = P_2 = 0.01$ for zero delay ($\tau = 0$). The solid blue line represents the instantaneous intensities of SCL1 and SCL2 (same). The solid red line is a rolling time average over 10 ns of the instantaneous intensities. 70

5.2 Spectrogram of instantaneous intensity oscillations taken from the $\tau = 0$ case in which $\kappa = 0.1$. 71

5.3 (a) Trajectories of the eigenvalues when $\kappa = 0.1$ for finite delay of $\tau = 0$ and constant phase $\theta\tau = 2\pi n$. (b) Simulations of the SCL intensities (I_1 and I_2) for $\kappa = 0.02$, $P_1 = P_2 = 0.01$, and $\tau = 100$ with constant (πn) phase. 73

5.4 (a) Trajectories of the eigenvalues when $\kappa = 0.1$ for finite delay of $\tau = 100$ and varying phase $\theta\tau$. (b) Simulations of the SCL intensities (I_1 and I_2) for $\kappa = 0.02$, $P_1 = P_2 = 0.01$, and $\tau = 100$ with varying phase $\theta\tau$. . . . 75

5.5 Experimental set-up. SCL: semiconductor laser, GS: glass slide, M: mirror, VND: variable neutral density filter (mounted on a translation stage), L3: laser used to quantify experimental coupling strength, PD: photodiodes, $P_{1,2}$: pump current controller 77

5.6 Profiles recorded for a cavity length $L = 27\,\text{cm}$, $P_1 = 41.5\,\text{mA}$, $P_2 = 45.1\,\text{mA}$, and VND at 260° 81

5.7 Profiles recorded for a cavity length $L = 51\,\text{cm}$, $P_1 = 41.5\,\text{mA}$, $P_2 = 45.1\,\text{mA}$, and VND at 260° 82

5.8 Profiles recorded for a cavity length $L = 74\,\text{cm}$, $P_1 = 41.5\,\text{mA}$, $P_2 = 45.1\,\text{mA}$, and VND at 220° 84

5.9 Simulated intensity profiles and eigenvalues for varying coupling strenth κ. The solid colored lines in (a) correspond to the intensity profiles which are simulated for five different $\Delta\omega$ of 0.01 (red), 0.02 (yellow), 0.03 (green), 0.04 (blue), and 0.05 (purple). The dashed vertical lines indicate the onset of growth predicted by the PT-symmetric model. 85

5.10 Varying κ and keeping $\Delta\omega$ fixed 86

Figure Page

5.11 Simulated phase plane of the inversion N_1 and intensity I_1, intensity time-series, and phase relationship time-series for identical pump currents ($P_1 = P_2 = 0.012$) and zero delay ($\tau = 0$). All parameters are fixed. The top row corresponds to $|\Delta\omega| = 0.020 > \kappa = 0.015$ and the bottom row when $|\Delta\omega| = 0.020 < \kappa = 0.025$ 89

5.12 Simulated intensity profiles for fixed pump currents ($P_1 = P_2 = 0.015$) when only the frequency mismatch $\Delta\omega$ is scanned from -0.05 to 0.05. The intensity, inversion, and phase profiles are simulated for a coupling strength, $\kappa = 0.025$. The red vertical line represents the theoretical $\mathcal{PT}$transition. 91

5.13 Experimental (top row) and numerical (bottom row) intensities of SCL1 (blue) and SCL2 (green) when the coupling strength is $\kappa = 0.0027$ (a,c) and $\kappa = 0.014$ (b,d). The pump current P_2 is decreased from $P_2 = 1.3$ to $P_2 = 0.8$. The vertical lines indicated the location when $\Delta\omega = \kappa$ (black dashed) and when phase breaking occurs $\dot{\phi}(t) = \Delta\omega' \neq 0$ (red solid). . 93

5.14 Experimental plot of the pump current value where the onset of growth begin for increasing coupling strength κ values, which are marked with red diamonds. The blue circles correspond to the simulated location where phase locking is broken ($\dot{\phi}(t) \neq 0$). The green stars represent the theoretical PT-transition ($\kappa = |\Delta\omega|$). 94

5.15 Same parameters as Fig. 5.13. Evolution of eigenvalues for the two coupling strength $\kappa = 0.003$ (a) and $\kappa = 0.017$ (b). The color profile corresponds to the pump current P_2 which is directly proportional to the frequency mismatch $\Delta\omega$. Each eigenvalue, λ_1 and λ_2, is shown depicted separately in (a2,b2) and (a3,b3), respectively, and the superposition is found in (a1,b1). Note that the avoided crossing in (a), which occurs for a pump current of $P_1 \approx 1.05$, occurs at $\lambda \approx 0$, thus indicating PT-symmetry breaking. 96

SYMBOLS

$E(t)$	slowly varying amplitude of complex electric field
α	linewidth enhancement factor
μ	index of refraction
χ	material susceptibility
ν_{RO}	frequency of the relaxation oscillations

ABBREVIATIONS

SCL	semiconductor laser
COF	conventional optical feedback
RO	relaxation oscillations
LK	Lang-Kobayashi
FOF	filtered optical feedback
FO	frequency oscillations
HWHM	half width at half maximum

ABSTRACT

Suelzer, Joseph S. PhD, Purdue University, May 2016. Double Optical Feedback and PT-symmetry Breaking Induced Nonlinear Dynamics in Semiconductor Lasers. Major Professor: Gautam Vemuri.

A central aim of this research is to probe the nonlinear dynamics that arise in a semiconductor laser due to optical feedback. We investigate two schemes of optical feedback. The first scheme subjects the laser to optical feedback from two external cavities (or two loops), wherein each cavity contains a spectral filter. Using two filtered optical feedbacks, we experimentally demonstrate the ability to elicit and control unique dynamics in the optical emission frequency (wavelength) of the laser. These results are compared to a deterministic model describing the evolution of the complex electric field and carrier density of the laser. As the feedback rate from one cavity is increased, we observe a period doubling route in the frequency dynamics. To determine the influence of quantum noise on the period doubling route, we examine an augmented model of the rate equations which includes the effects of spontaneous emission and shot noise. One of the more surprising results is that in the presence of noise a larger feedback strength is required to induce chaotic dynamics. We find that noise drives the system toward stable attractors and the effects of the time-delay on the periodic dynamics are more pronounced.

The second scheme we use is a system consisting of two time-delayed, optically coupled semiconductor lasers. We show that coupled lasers are an excellent test-bed to study parity (P) and time-reversal (T) symmetry breaking. Not only do optically coupled SCLs capture many of the characteristic signatures of PT symmetry breaking, but the time-delay between the lasers introduces novel and surprising features. We develop a simple PT model (analogous to a 2x2 Hamiltonian) that includes the effects of the time-delay. By examining the eigenvalues of the PT model, we can predict the

intensity fluctuations by scanning the PT parameter, i.e. the frequency difference between the lasers. We experimentally observe the intensity fluctuations and find excellent agreement with the rate equation model which includes the dynamics of the carrier inversion and optical field.

1. Introduction to Optical Feedback

This chapter gives a brief introduction to optical feedback in semiconductor lasers by outlining the historical development for this field. Following this development, it becomes clear how the original motivations, which were quite pragmatic, evolved to broader and more fundamental studies. In particular, by using optical feedback in semiconductor lasers, we discuss the ability to probe fundamental attributes of nonlinear dynamics. We outline some investigations that foster important applications in photonics, and discuss how the content of our research fits within the fundamental and applied studies.

1.1 Historical Introduction

The conception and development of the laser is a remarkable story. The statue of Charles Townes commemorating his reflections on a park bench in 1951, the race to build the first laser (along with ensuing legal wars), and the technological fruits of the laser are fascinating reminders of the adventures within science. The story serves, especially for the purpose of this thesis, as an illustrative example of how applied and fundamental science can mutually foster progress on both sides. Shortly after Mainman's demonstration of the first optical laser, his assistant, Irnee D'aenens, described the laser "as a solution looking for a problem." Indeed, scientists have discovered many "problems" over the last 60 years, and a testament to this is the number of Nobel Prizes (19) related to the laser [1]. Irnee's statement serves as an overarching theme of this dissertation. In particular, the "problem" we investigate is nonlinear dynamics, and the "solution", or test-bed, we use to explore this field is semiconductor lasers (SCLs) subject to optical feedback. As we review the important

characteristics of SCLs and the features introduced because of optical feedback, it will become clear why this system provides an excellent tool to probe nonlinear dynamics.

In 1962, a group from General Electric Research Laboratory published the first observation of coherent infrared radiation from a GaAs p-n junction [2]. Less than a month later, IBM researchers reported stimulated emission of radiation from the same semiconductor material [3]. In the SCL, the optical gain was provided by electron-hole recombination in the active region of the p-n junction. In this region, the gain is controlled by the carrier density which is externally supplied by injecting current across the semiconductor material. The ends of the semiconductor are cleaved to create an optical cavity, thus providing the two necessary ingredients - gain and feedback - for amplified stimulated emission. At this time, practical use of these SCLs were limited. To achieve lasing, the semiconductor materials were immersed in liquid nitrogen and supplied with a pulsed current lasting between 1 μs to 20 μs, which were required because of the large threshold currents (> 8.5 kA/cm^2) [2, 3].

Over the next decade, scientists and engineers were spurred by the demand to improve commercial viability and laser performance [4]. In particular, successful efforts were concentrated on developing cw emission at room temperature and increasing efficiency. Much of the success is attributed to improvements on the design of the SCL structure [1, 5]. The design improvements increased carrier confinement in the active region and introduced a waveguide for the optical field [5]. This resulted in lasers with an efficiency $> 50\%$ and an active region with dimensions on the order of $10\,\mu$m [6]. Indeed, we shall see that these two characteristics contribute to the SCL's large gain per unit length, which is responsible for the extreme sensitivity to external perturbations and incidentally makes it an excellent candidate to elicit nonlinear dynamics. Before we turn to this point, we look at fundamental characteristics of the SCL that play a significant role in determining the dynamics which arise in SCLs due to optical feedback.

1.2 Characteristics of the SCL and optical feedback

In 1982, Charles Henry developed the theory of the linewidth of SCLs. At this time, experimental measurements of the linewidth were found to be 30 times greater than explained by current theories. Henry elegantly demonstrated that the linewidth of a SCL is enhanced by the multiplicative factor $1 + \alpha^2$ [7]. The α parameter, also called the Henry factor, quantifies the coupling between the phase and amplitude of the laser field. For a typical semiconductor laser, this value ranges between 2 and 7. Henry showed that $\alpha = \Delta\mu_R/\Delta\mu_I$, where $\Delta\mu_R$ is the change in the real part of the refractive index and $\Delta\mu_I$ is the change in the imaginary part of the refractive index [7]. The changes in $\Delta\mu_I$ and $\Delta\mu_R$ are coupled through the carrier density which affects both the gain and index of refraction. The dependence on the carrier inversion n, can be expressed by,

$$\alpha = -\frac{d\chi_R(n)/dn}{d\chi_I(n)/dn}, \tag{1.1}$$

where χ is the complex susceptibility and the subscripts R and I correspond to the real and imaginary parts. Not only does α play a significant role in the spectral characteristics, but it has a profound influence on the dynamics of SCLs.

To understand the effects that a non-zero α has the dynamics, we examine a SCL subject to conventional optical feedback (COF). An experimental design using COF consists of external reflector situated a distance L from the laser facet. The reflector returns (or re-injects) a portion of the laser emission back to the SCL cavity. Feedback temporarily increases the number of photons inside the laser cavity. The additional photons in the active region of the SCL change the carrier density, or inversion number. The change in carrier density affects both $\Delta\mu_I$ and $\Delta\mu_R$, and changes the gain, $g(n)$, since the gain is directly proportional to $\Delta\mu_I$. Recalling that μ_R is the real part of the refractive index, it should not surprise us that the phase is altered due to $\Delta\mu_R$. We now examine the evolution and time-scales of these processes in greater detail.

Before the SCL returns to steady-state emission, the intensity and inversion undergo damped relaxation oscillations (RO) that correspond to an exchange in energy between the photons and carrier density inside the laser cavity. The period of the RO typically last between 100 ps and 1 ns, corresponding to a frequency, ν_{RO}, between 10 GHz and 1 GHz. A linear stability analysis of the laser rate equations allows us to express the RO frequency in terms of intrinsic SCL and operating parameters [8], written as

$$\nu_{RO} = \frac{1}{2\pi}\sqrt{\frac{\xi I_s}{\tau_p}}, \tag{1.2}$$

where ξ is the gain coefficient, τ_p is the photon lifetime, and I_s is the intensity at steady-state. We note that ξ and I_s depend on the operating parameters, in particular the injection current. The RO are damped with a rate given by

$$\Gamma_{RO} = \frac{1}{\tau_e} + \xi I_s, \tag{1.3}$$

where τ_e is carrier lifetime [8]. The RO and damping rate are two important timescales of the SCL. The photon and carrier lifetimes not only determine ν_{RO} and Γ_{RO}, but become an integral part of dimensional analysis of the rate equations that are described in the next chapter. The RO represent one of the two important time-signatures exhibited by COF dynamics.

The second signature, the time-delay τ, is present because of the finite propagation length which is external to the SCL cavity, i.e. $\tau = 2L/(\mu c)$, where L is the distance between the laser facet and external reflector and μ is the refractive index. From a mathematical perspective this renders the system infinitely dimensional. This can be understood in the following way:

- at time t, the SCL "feels" a field that was emitted at time τ earlier;
- at time $t - \tau$, the SCL "felt" a field emitted at τ earlier;
- at time $t - 2\tau$, the SCL "felt"... ad infinitum

In addition to adding unique features to a nonlinear system (i.e. SCL), the time-delay introduces a degree of complexity in which some typical tools used in nonlinear

analysis can no longer be applied. The ability to easily change the time-delay τ or add multiple delays makes the system an excellent test-bed to probe time-delayed dynamics. Up to this point we have discussed the dynamics in a general sense. To better understand the contributions of our research to this field, it is helpful to examine some of the fundamental and applied investigations that have acted as a springboard for future studies.

1.3 Fundamental studies and applications of SCL dynamics

As early as the 1970's systematic studies of SCLs subject to optical feedback began to emerge [9–11]. Influenced by the rapidly developing field of telecommunications, special attention was given to the stability properties of SCL with optical feedback [12–17]. However, it was soon recognized that optical feedback provided the ability to elicit and sustain optical microwave oscillations, whose frequencies were characterized by two time-signatures, the RO frequency and time-delay [10, 11, 14]. Several investigations demonstrated the presence of a dominant frequency that was inversely proportional to the cavity length L [10,11]. By altering the length of an optical fiber from 10 cm to 2 km, Ikushima and Maeda showed for a particular feedback strength that the fundamental frequency was determined only by the round-trip time, i.e. the fundamental frequency is $f = c/2nL$ [11]. Although the investigations were able to relate the observed microwave frequencies to the parameters of the external cavity and SCL, no simple theory existed which allowed for an analytical analysis.

This changed in 1980 when Lang and Kobayashi (LK) extended the compound cavity laser rate equations, which describe the complex electric field ($E(t)$) and carrier inversion number ($N(t)$), to include an additive term accounting for the delayed feedback field ($E(t-\tau)$) [18]. Before we describe the LK-model in Chapter 2, we would like to briefly discuss some of the fruits that arose from this study. In addition to providing a rate equation model describing optical feedback, this seminal study demonstrated that various phenomenon, including multistability and hysteresis, arise

due to the interference between the cavity and feedback fields [18]. The effects were analogous to those found in nonlinear Fabry-Perot resonators [18]. Although Lang and Kobayashi only demonstrate a small number of features which are general to nonlinear systems, this study opened an avenue which still continues to be a field of intense study.

An example of this continued interest is a study from 1986 when Tkach and Chraplyvy (TC) provided a systematic investigation classifying the effects of feedback for varying feedback strength and cavity lengths [19]. The feedback strength was varied over 8 orders of magnitude from -80 dB to -8 dB, and five regimes were found with well-defined transitions [19]. From a our standpoint, the most interesting regimes are the middle three wherein different dynamics can be induced. These dynamics range from mode-hopping to coherence collapse [19]. Recently, the TC classification has been revisited by Donati and co-workers. Because of the vast (and growing) number of applications, Donati and co-workers were prompted to depict the regimes wherein particular applications lie [20]. We will now look at some of the applied research that has emerged from optical feedback.

1.3.1 Applied Research

The ability to probe different dynamical regimes using simple injection and optical feedback schemes enables a wide range of applications from laser characterization and linewidth reduction [21–23] to microwave generation [24–28]. Another dynamical regime wherein optical feedback provides rich test-bed for applied and fundamental research is chaotic waveforms. [29–31]. In particular, there has been a concentrated effort on exploiting chaotic waveforms in two areas: random bit generation and chaotic synchronization.

Random bit generation from a SCL is attractive because the “randomness” is generated from a physical process. The random numbers generated by software, unlike chaotic SCLs, employ sophisticated algorithms, which given the same initial

kernel would produce an identical sequence of random numbers. A typical (simplified) experiment induces chaotic dynamics via optical feedback and uses an analog to digital converter to generate a sequence of bits. The "quality" of randomness and speed (bits/s) can be improved by focusing on the feedback scheme or post-processing [31]. Using optical feedback, several studies have demonstrated random bit generation with bit rates exceeding 100 Gb/s [31].

The second area of focus, chaotic synchronization, continues to remain attractive both as means for encryption and to study the fundamental properties of time-delayed synchronization [32–38]. Many interesting features have grabbed the attention of researchers including a desire to increase the bandwidth of the chaotic signal [37, 39], observe anticipated synchronization [34, 36], and distinguish between general and complete synchronization [40, 41]. The generation stable chaotic synchronization has shown great promise for applications outside of laboratory settings. An example is the realization of chaotic synchronization over a 120-km optical fiber utilizing the injection of semiconductor lasers. [42]. To make this a viable candidate for random number generation or encryption, performance improvements are sought by increasing the bandwidth and the stability of the chaotic signal.

1.4 Our Contribution

Optical feedback continues to provide a rich system for the study of nonlinear dynamics. However one is essentially limited to two control parameters, the feedback strength and external cavity length. Motivated by the desire for greater control over the dynamics, one can manipulate the optical feedback using various schemes. A promising and intensely studied procedure involves spectrally filtering the optical feedback. Filtered optical feedback (FOF) achieves control over the feedback which is external to the laser. The filter's response function is highlighted in Fig. 1.1. Examining Fig. 1.1, the key feature is that the transmission (or feedback intensity) is frequency dependent. In addition, two key parameters emerge with the introduc-

tion of the filter, viz. the bandwidth and detuning (indicated by the frequency span between the dashed vertical lines). Here the detuning is defined as the difference be-

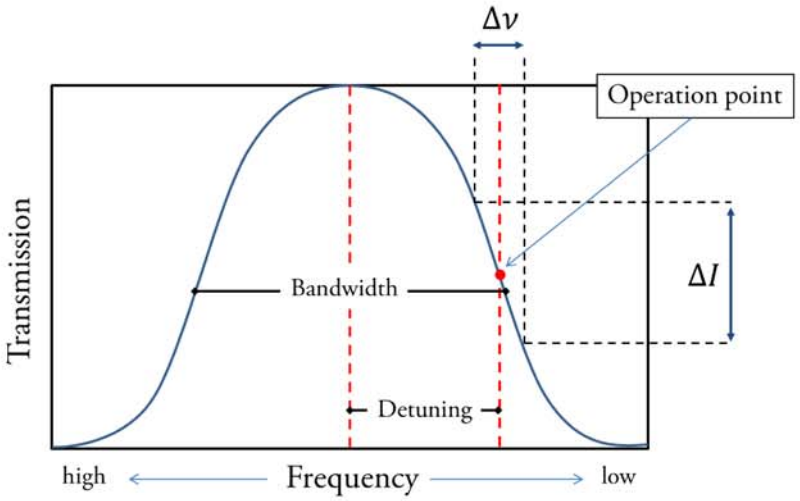

Figure 1.1. Representation of the transmission function of a spectral filter: a change in frequency represented by $\Delta\nu$ results in a change in the intensity represented by ΔI

tween the optical frequency of the laser (solid red circle marked as "operation point") and the center frequency of the filter (the centered dashed vertical red line). Several studies have shown that the dynamics significantly depend on the bandwidth and the detuning [34, 43, 44]. A unique feature of FOF is the ability to elicit dynamics in the optical frequency (wavelength) of the emission while the intensity remains almost constant [45]. This is a surprising result because of the strong coupling between the phase and amplitude (α-parameter) of the laser field. However, it is possible to elicit frequency oscillations (FO) by a judicious choice of the filter and feedback parameters, in which the filter dispersion compensates for the amplitude-phase coupling [46, 47]. Predicting the FOs are difficult, and typically a numerical bifurcation analysis is necessary determine the parameter windows wherein the FOs occur [48].

Not only does the filter influence the stability of the periodic dynamics but also the "quality" of the chaotic waveforms generated in this manner. The time-delay

signatures are an essential characteristic in determining the "randomness" of the chaotic signal. Ideally, for a truly random signal any time-delayed (or periodic) features would be fully suppressed. In particular, it was recently demonstrated that filtered optical feedback suppresses the time-delay signatures of the chaotic waveforms [49]. The key to this suppression lies in the chromatic dispersion associated with the filter since filters can provide not only a frequency dependent loss but also a frequency dependent feedback delay [49]. In both examples, performance improvements are sought by increasing the bandwidth and the stability of the chaotic signal. Thus, a better understanding of the dynamics and the ability to achieve robust control over optically-coupled systems is a main focus of our work. We demonstrate how a second feedback cavity containing a spectral filter achieves greater control as well as introducing some surprising features due to the second time-delay. We call this system two FOF, since each of the two external cavities contain a spectral filter.

1.5 Outline

The bulk of our work can be divided into three parts: (i) experimental investigations of frequency dynamics from two FOF, (ii) theoretical study of the effects of quantum noise on the dynamics from two FOF, and (iii) experimental realization of parity and time-reversal symmetry breaking using two mutually coupled SCLs. We introduce the rate equations for optical feedback in Chapter 2, which provides the "backbone" for the model of two FOF and the model of two optically coupled SCLs. The experimental and numerical investigations are discussed in Chapter 3 and Chapter 4, respectively. In Chapter 5, we introduce the context, PT symmetry breaking, in which we study mutually coupled SCLs. We develop a model for time-delayed PT symmetry breaking which anticipates surprising results due to the presence of time-delay. The experimental observation of these results are discussed. Finally, a summary and synthesis of our work is provided in Chapter 6.

2. Rate equations for a semiconductor laser subject to optical feedback

To obtain the SCL field rate equation, the starting point is Maxwell's equations. For most SCL materials, the material response is assumed instantaneous, since the relaxation time ($\sim 0.1\,\mathrm{ps}$) of the polarization $\mathcal{P}$ is much faster than the photon and carrier lifetimes. The polarization response is adiabatically eliminated. The complex envelope $E(t)$ of the optical field $\mathcal{E}(t) = E(t)e^{-i\omega t}$ varies slowly so that the higher order derivatives can be neglected. In addition, for many SCL designs it is appropriate to assume a single transverse and lateral mode. Following the above prescription [5], the single mode rate equation of the complex slowly varying electric field may be written as

$$\frac{dE}{dt} = \frac{1}{2}(1 + i\alpha)\xi N(t)E(t), \tag{2.1}$$

where ξ is differential gain coefficient expressed in units of s^{-1} and $N(t)$ is the carrier density ($n(t)$) minus the threshold carrier density (n_{thr}). To express the field rate equation in this form, we have assumed the semiconductor material gain depends linearly on the carrier density [17].

The first term in Eqn. (2.1) accounts for growth or decay of the field depending on the sign of the adjusted carrier density $N(t)$. The second term causes a phase shift of the field due to the linewidth enhancement factor α. We recall that α quantifies amplitude-phase coupling of the field which is expressed in Eqn. (1.1).

Lang and Kobayashi (LK) were the first to augment the field rate equation (Eqn. (2.1)) to account for time-delayed feedback [18]. The LK rate equations can be expressed by

$$\frac{dE}{dt} = \frac{1}{2}(1 + i\alpha)\xi N(t)E(t) + \kappa e^{-i\omega\tau}E(t - \tau). \tag{2.2}$$

The coupling term includes the explicit time-delay ($E(t-\tau)$) as well the phase accumulation $e^{-i\omega\tau}$ of the feedback field. The feedback rate is expressed by $\kappa = \zeta/\tau_{in}$, where ζ^2 is the power reflected by the external cavity relative to the power reflected by the laser facet and τ_{in} is the round-trip time in the laser cavity.

We have not described the rate equation for the population inversion which is expressed through the carry density $N(t)$. The rate equation for $N(t)$ is given by

$$\frac{dN}{dt} = J - J_{thr} - \frac{N(t)}{T_1} - [\Gamma_0 + \xi N(t)]|E(t)|^2, \tag{2.3}$$

where the difference between the pump rate and threshold is $J - J_{thr}$. T_1 is the carrier lifetime, and Γ_0 is the photon decay rate. The first term, $J - J_{thr}$, adds carriers due to the pump current; the second and third terms account for spontaneous decay and depletion due to stimulated emission, respectively.

We now turn our attention to the effects on Eqn. (2.2) when the feedback field is spectrally filtered. The primary function of the filter is a frequency dependent reflectivity (or transmission). The response function, $r(\omega)$, of the filter is typically assumed Lorentzian [43], i.e.

$$r(\omega) = \frac{\Lambda}{\Lambda + i(\omega - \Delta)}, \tag{2.4}$$

where ω is the instantaneous optical frequency, Λ is the half width at half maximum (HWHM) of the filter and Δ is the detuning of the solitary laser frequency from the center frequency of the filter. To determine the rate equation for the feedback field, we outline the procedure described in Ref. [43]. First, the response $r(\omega)$ operates on the Fourier components of the electric field $E(\omega)$. After this operation, the inverse Fourier transform is applied in order to determine the time dependence of the feedback $F(t)$. This results in an integral expression of the field which is differentiated with respect to time and the rate equation for the spectrally filtered feedback field is expressed by

$$\frac{dF}{dt} = \Lambda E(t-\tau)\mathrm{e}^{-i\omega_0\tau} + (i\Delta - \Lambda)F(t). \tag{2.5}$$

The feedback term $\kappa e^{-i\omega\tau}E(t-\tau)$ in Eqn. (2.2) is replaced by filtered field $F(t,\tau)$ that is now described by Eqn. (2.5).

Finally, to include the effects of quantum noise, the rate equations require a further modification. This modification is an additive Langevin term that accounts for the spontaneous emission and shot noise terms. These terms are described by $L_E(t)$ and $L_N(t)$, respectively. Both noise sources are assumed to be Gaussian with zero mean. Their autocorrelation functions are given by,

$$\langle Re(L_E(t))Im(L_E(t'))\rangle = 0, \tag{2.6a}$$

$$\langle Re(L_E(t))Re(L_E(t'))\rangle = \langle Im(L_E(t))Im(L_E(t'))\rangle = R_{sp}\delta(t-t'), \tag{2.6b}$$

$$\langle L_N(t)L_N(t')\rangle = D\delta(t-t'). \tag{2.6c}$$

The rate of spontaneous emission is written as $R_{sp} = \beta_{sp}CN^2$, where β_{sp} is the fraction of spontaneous emission coupled into the dominant mode and C is a radiative recombination rate [5]. The shot noise diffusion rate is given by D. The noise sources L_E and L_N are derived quantum mechanically in order to arrive at their explicit form and statistical properties [50]. Although the noise sources are correlated in a SCL [50], we found that correlating sources resulted in no significant difference when compared to uncorrelated noise [51]. Therefore, the analysis in Chapter 4 is done with uncorrelated noise.

The final form of the rate equations are given by

$$\frac{dE}{dt} = \frac{1}{2}(1+i\alpha)\xi N(t)E(t) + \kappa F(t,\tau) + L_E(t), \tag{2.7a}$$

$$\frac{dN}{dt} = J - J_{thr} - \frac{N(t)}{T_1} - [\Gamma_0 + \xi N(t)]|E(t)|^2 + L_N(t), \tag{2.7b}$$

$$\frac{dF}{dt} = \Lambda E(t-\tau)\mathrm{e}^{-i\omega_0\tau} + (i\Delta - \Lambda)F(t). \tag{2.7c}$$

These equations form the backbone of the model describing feedback from two spectrally filtered external cavities. This system is discussed in the next two chapters. To describe optical coupling from a second SCL, which is found in Chapter 5, we rely on a similar model that replaces the feedback term with a coupling term accounting for the field from the neighboring SCL.

3. Semiconductor Laser subject to two filtered optical feedbacks

Main results of this chapter have been published in Ref. [52]

3.1 Introduction

Semiconductor lasers subject to optical feedback continue to fascinate researchers across many disciplines. This attraction exists because the semiconductor laser is a paradigm for nonlinear systems - capable of capturing a myriad of nonlinear dynamical behaviors [53] (see references therein). Recently, there has been an interest in using double or multiple optical feedbacks in which each feedback contains a different time-delay [54–59]. The time-delays are produced by arranging the external optics such that each cavity has a different length. Although multiple time-delays are an interesting theoretical question, pragmatically more than two cavities is difficult to implement. To induce dynamics a certain amount feedback strength is required [19]. A feedback system with multiple cavities introduces more optical elements and with the additional elements greater losses occur. The attenuation of the feedback makes it difficult to elicit dynamics. However, the implementation of two external cavities has shown great promise [55, 56]. A second time-delay has demonstrated the ability to suppress time-delay signatures in the optically induced dynamics [58]. This is of particular interest for those who wish to apply the chaotic signal for encryption or random number generation. For this reason, the ability to suppress the time-delay, FOF has also gained attention.

As we mentioned in the Introduction of this dissertation, FOF primarily acts as frequency dependent optical attentuator. In addition to the unique dynamics (FOs) introduced because of the nonlinear response of the filter, the filter provides the ability

to control sustained microwave oscillations [46]. In particular, the period of FOs can be tuned by changing the bandwidth of the spectral filter [47]. The spectral filter in Ref. [47] consists of a Fabry-Perot etalon made up of two plane mirrors with a separation distance d. Since the bandwidth is expressed by $\delta_f = c/2df$, changing the separation between the filter's mirrors inversely changes the bandwidth and hence the frequency of the FO. This can be understood by noting that d (along with the finesse f) increases the total time of the feedback field spent outside the SCL. The additional control gained from the spectral filter, along with the features introduced by a second cavity (i.e. second time-delay), motivated us to combine these two schemes. We experimentally investigate a SCL subject to feedback from two external cavities each containing a spectral filter. We call this system two FOF.

The inclusion of the second FOF provides the technical advantage of an extra set of control parameters for the purpose of engineering and applications mentioned earlier. In the frequency-oscillation regime, our system shows a rich control over the frequency dynamics of the laser light. Our results show that the period of frequency oscillations of the laser light is determined by the two time scales related to the two feedback loops, and the frequency corresponding to this period is given by the average of the fundamental frequencies of cavity 1 and cavity 2. The average frequency is dependent on the relative feedback strength from the two cavities and corresponds to the weight between them. A proper adjustment of the cavity lengths and other related parameters leads to the oscillations at the frequency which represents the average of the higher harmonics of cavity 1 and the fundamental frequency of cavity 2. The amplitudes of the frequency components in the single FOF can be controlled by adding a second FOF, and in particular the amplitude of fundamental frequency can be suppressed while the amplitude of the second harmonic becomes larger than that of the fundamental frequency. A cascade of period doubling bifurcations leads the dynamics to a chaotic state.

This chapter is organized as follows. The experimental set-up used to study the laser dynamics with two FOFs is presented in Section 3.2, and the experimental proce-

dure for the detection of the frequency fluctuations is given in Section 4.3. Section 3.4 contains the theoretical model and numerical details for describing the dynamics of the two-FOF laser. The experimental and numerical results of controlled oscillations in the frequency of the laser light are presented in Section 3.5. A period doubling route to chaos through bifurcation analysis is also discussed. The summary of the work is presented in Section 3.6.

3.2 Experimental Setup

The light is emitted by a commercial (Sharp LT027) Fabry-Perot (FP) type diode laser (DL) with an average power of 7 mW at an operating current of 65 mA. When the DL is free running, i.e., with no feedback, it is a single mode laser emitting at 780 nm. Beginning at the DL and following the path of light in Fig. 3.1, the light is initially reflected by the beam splitter (BS1). The optical isolator (OI) provides an isolation of approximately -28 dB, ensuring that undesired reflections do not return to the laser facet. The first glass plate (G) reflects a portion of the light through the diagnostic filter to a (Thorlabs DET10A) silicon photodiode (PDA) with a 1-ns rise time. The diagnostic filter is used to convert frequency fluctuations into intensity fluctuations. The half-wave plate (HWP1) and polarizing beam-splitter (PBS) allow us to control the fraction of light that enters each cavity. HWP2 is introduced so that light returning to the final OI has the same polarization as the emitted laser light in order to achieve maximum feedback. The frequency selective FP filters consist of two plane mirrors separated by a distance d. Each external cavity contains a glass slide to reflect a portion of the light to PDB and PDC; both are silicon diodes (Thorlabs DET210) with a 1-ns rise time. The light transmitted through the glass slides is directed through the final OI before it is coherently fed back into the laser.

As mentioned in Section 3.1, there are three regimes depending on the value of the spectral filter bandwidth relative to the relaxation oscillation frequency and the external cavity mode spacing. The regime of maximum interest is where the spectral

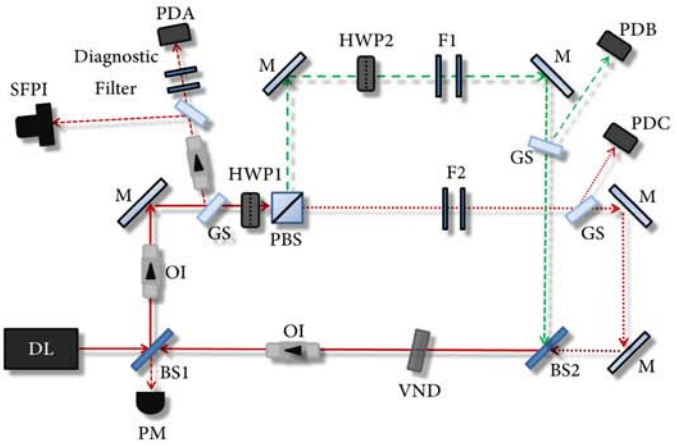

Figure 3.1. Schematic of the experimental set-up. DL: diode laser; BS: beam splitter; OI: optical isolator; M: mirror; G: glass plate; HWP1, HWP2: half-wave plates; PBS: polarizing beam-splitter; PDA, PDB, PDC: Photodiodes.

filter bandwidth lies between the external cavity mode spacing and the relaxation frequency. The mirror reflectivity determines the finesse f, which is estimated by counting the number of reflections when the mirrors are slightly misaligned. The spectral filter bandwidth, $\delta\nu_f = \frac{c}{2df}$, is varied by changing either the mirror reflectivity or spacing. The mirror reflectivity is changed by replacing one or both mirrors and the spacing is modified by moving a translation stage which contains one of the mirrors. The bandwidth of the spectral filters determines the permissible time-scale of dynamics. In our experiments, the lengths of our external cavities are typically between 400 cm and 150 cm, resulting in an external cavity mode spacing ranging from 75 MHz to 200 MHz (and filter bandwidth which ranges from 0.75 GHz to 2 GHz). This is done to have approximately ten external cavity modes within our spectral filter profile and in order to filter out the relaxation oscillations of the laser which have a frequency of 4 GHz.

In addition to studying the frequency dynamics, the signals from the two photodiodes, PDB and PDC are sent to an oscilloscope. This allows us to view both filter profiles simultaneously in order to compare the bandwidths and the free spectral ranges.

3.3 Detection of frequency fluctuations

In order to observe the frequency dynamics, the laser light is directed to a photodiode, PDA in Fig. 3.1. As mentioned in Section 3.2, the diagnostic filter converts frequency fluctuations into intensity fluctuations. The diagnostic filter consists of two plane mirrors with reflectivities that range between 70% to 90%. The diagnostic filter is designed so that the bandwidth is approximately five times larger than the cavity filters bandwidth. The larger bandwidth increases the likelihood that the optical frequency of the laser will fall on the flank of the diagnostic filter profile. In turn this provides a near linear conversion from frequency to intensity. The electronic signal is amplified by a low noise amplifier (Mini-Circuits ZFL-500LN) and sent to an

oscilloscope (Lecroy 9450A) with a 10 GS/s sampling rate which allows us to observe the frequency dynamics in real time. The signal is also sent to a spectrum analyzer (HP 8590B) allowing us to view the relative intensity noise (RIN) spectrum.

The frequency dynamics are first observed for each solitary cavity. We then look for dynamics when two feedbacks are present. The dynamics are found by controlling the amount of feedback, κ_1 and κ_2, and the detuning between the solitary laser frequency and the filter center frequency, Δ_1 and Δ_2. The amplitude of the feedback field to the DL is modified by placing a variable neutral density filter after the last optical isolator. To vary the detuning, we note that once the DL is above a threshold current, approximately 50 mA, there is a linear relationship between the current applied and the optical frequency of the laser. We use an external ramp to scan the pump current to the DL, thus controlling the optical laser frequency and hence the detuning. In practice, once the range of current is roughly identified where dynamics occur, the external ramp is turned off and we manually adjust the current to search for other dynamics such as period doubling. Other parameters, such as cavity lengths and the detuning between the filter center frequencies, are systematically explored to determine distinct dynamics, shown in Figs. 3.2-3.8.

3.4 Theoretical model

In Chapter 2, we described the rate equations of a semiconductor laser with FOF from a single cavity given by Eqn. (2.7). Our set-up (Fig. 3.1) consists of two external

cavities each containing a Lorentzian filter, thus the normalized rate equations are modified to include the second FOF and can be written as

$$\begin{aligned}
\frac{dE}{dt} &= (1+i\alpha)N(t)E(t) + \kappa_1 F_1(t,\tau_1) \\
&\quad +\kappa_2 F_2(t,\tau_2), && (3.1)\\
T\frac{dN}{dt} &= J_0 - N(t) - (1+2N(t))|E(t)|^2, && (3.2)\\
\frac{dF_1}{dt} &= \Lambda_1 E(t-\tau_1)\mathrm{e}^{-i\omega_0\tau_1} + (i\Delta_1 - \Lambda_1)F_1(t), && (3.3)\\
\frac{dF_2}{dt} &= \eta\Lambda_2 E(t-\tau_2)\mathrm{e}^{-i\omega_0\tau_2} + (i\Delta_2 - \Lambda_2)F_2(t), && (3.4)
\end{aligned}$$

where α is the amplitude phase coupling, and J_0 is the injection current (with the threshold value subtracted out). κ_1 and κ_2 are the feedback rates, T is the ratio of carrier lifetime to the photon lifetime, τ_1 and τ_2 are the delay times taken by the light to cover the distance in the cavities 1 and 2, respectively. $E(t-\tau_1)$ and $E(t-\tau_2)$ are the fields delayed by time τ_1 and τ_2, respectively. Λ_1 and Λ_2 are the half-width at half-maximums of the two filters. Δ_1 and Δ_2 are the detunings of the filters center frequencies with respect to the solitary laser frequency. $\omega_0\tau_{1,2}$ are the feedback phases of the fields accumulated during the propagation of light in the cavities 1 and 2. For simplicity, the interaction between the two filters is ignored. The optical feedbacks can be controlled either by changing the feedback rates κ_1 and κ_2 or by tuning Δ_1 and Δ_2. Time t is measured in units of the photon life-time, which is taken to be 10 ps for a typical semiconductor laser. The introduction of time delay in the system makes it infinite dimensional, therefore an analytical study is very difficult. Thus to explore the dynamics of two FOF laser, we perform numerical simulation. Numerical integration of the above equations is done using the Runge-Kutta fourth-order scheme with a step size = 0.014 (in units of cavity photon life-time, equivalent to 0.14 ps) [**?**]. A small asymmetry has an effect similar to a change in the feedback rate, and in the following, we set $\eta \approx 1$. The scaled parameter values used in the simulation, corresponding to the experimental conditions, are $\alpha = 5$, $T = 100$, $J_0 = 3.5$, and $\omega_0\tau_{1,2} = -6\pi$.

In order to study the frequency oscillations of the laser dynamics, we write the complex envelopes of the laser and feedback fields in the form

$$E(t) = \sqrt{I_L(t)}\, e^{i\phi_L(t)}, \tag{3.5}$$

$$F_{1,2}(t) = \sqrt{I_{F_{1,2}}(t)}\, e^{i\phi_{F_{1,2}}(t)}, \tag{3.6}$$

where I_L and $I_{F_{1,2}}$ are the laser and feedback field intensities, and ϕ_L and $\phi_{F_{1,2}}$ are their phases, respectively.

3.5 Experimental and numerical results

3.5.1 Controlled frequency oscillations

Experimentally, the length of each cavity is determined from the recorded RIN spectra by allowing the feedback from each solitary cavity separately. Figures 3.2(a) and (b) show the fundamental frequencies $f_{\text{ext1}} = 105.9$ MHz and $f_{\text{ext2}} = 121.6$ MHz of cavity 1 and cavity 2, respectively, which correspond to the lengths of 283 cm and 247 cm, respectively. Once the fundamental cavity frequencies are determined, both fields are fed back into the laser. As in the case for a single FOF in Refs. [44, 46] where the period of oscillations of laser frequency is dominated by the delay time of the single cavity, in two FOFs, the period of frequency oscillations is determined by two time delays related to the feedback loops (the filters add a substantial frequency shift of $\sim 1/\Lambda_{1,2}$ to the period of the frequency oscillations [47]). The frequency corresponding to this period is given by the average of the fundamental frequencies of cavity 1 and cavity 2. Figure 3.3(a) displays the RIN spectrum of the laser when the two feedbacks are of approximately equal strengths. The dominant frequency, 114.8 MHz, corresponding to the peak in the spectrum (Fig. 3.3(a)) shows the average of the two fundamental cavity frequencies (105.9+121.6)/2 = 113.8 MHz.

This average frequency is dependent on the ratio of the feedback strengths from the two cavities. If the feedback from cavity 1 is larger than that from cavity 2, the average frequency (112.4 MHz) shifts towards the fundamental frequency of cav-

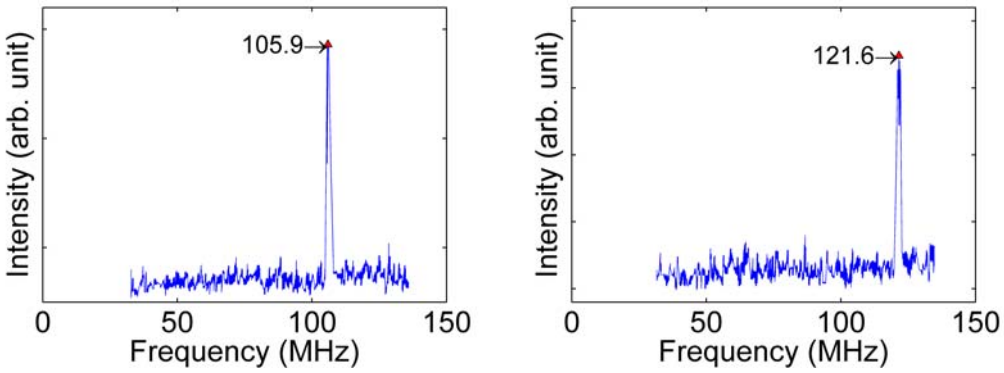

Figure 3.2. Experimentally measured RIN spectra when the feedback is provided by only (a) cavity 1, and (b) cavity 2.

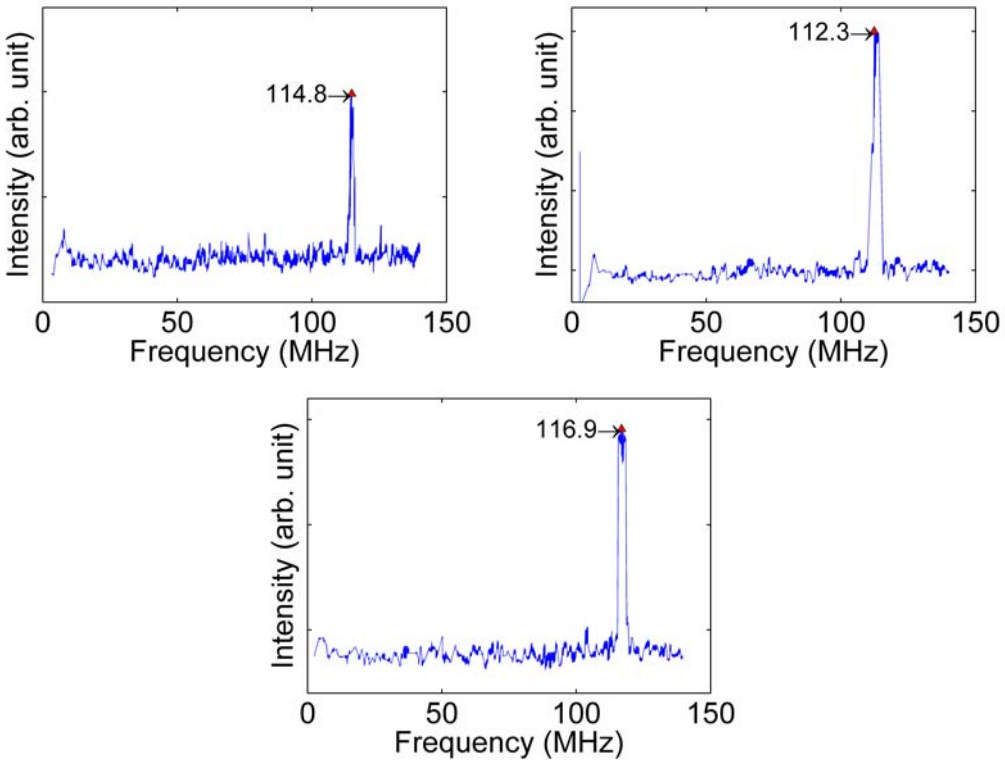

Figure 3.3. Experimentally measured RIN spectra depicting the change in frequency oscillations as the ratio of feedbacks from the cavities is varied. Spectra recorded (a) at approximately equal feedback strengths from the two cavities, (b) when the feedback strength from cavity 1 is larger than that from cavity 2, and (c) when the feedback strength from cavity 2 is larger than that from cavity 1.

ity 1, as shown in Fig. 3.3(b). Similarly, the average frequency, 116.9 MHz, shifts towards the fundamental frequency of cavity 2, when the feedback from cavity 2 is larger, as shown in Fig. 3.3(c). These experimental results are verified by numerical results, which we reported in Ref. [52], and a good agreement between the theory and experiment was found.

In Fig. 3.3(a), the frequency of 114.8 MHz has a small deviation from the average frequency of (105.9+121.6)/2 = 113.8 MHz. This discrepancy arises due to the fact that the number of external cavity modes of cavities 1 and 2 lying under the profiles of filters 1 and 2 are not the same. Thus two FOF fields from the two cavities are not equal, and hence the feedback amounts $\kappa_1 F_1$ and $\kappa_2 F_2$ are not the same. In particular, $\kappa_2 F_2 > \kappa_1 F_1$, and thus the average frequency shows a shift towards the higher frequency side of cavity 2. In this case, the difference between the two fundamental cavity frequencies is smaller than the difference between the higher harmonics, i.e., $|f_{\text{ext1}} - f_{\text{ext2}}| < |2f_{\text{ext1}} - f_{\text{ext2}}| < |f_{\text{ext1}} - 2f_{\text{ext2}}|$. Then the two fundamental cavity frequencies beat together inside the laser and determine the period of oscillations of the laser frequency, and the frequency corresponding to this period represents the average of the two fundamental cavity frequencies.

Now we change the cavity lengths so that the two fundamental cavity frequencies are $f_{\text{ext1}} = 75$ MHz and $f_{\text{ext2}} = 131$ MHz. In this case $|2f_{\text{ext1}} - f_{\text{ext2}}| < |f_{\text{ext1}} - f_{\text{ext2}}| < |f_{\text{ext1}} - 2f_{\text{ext2}}|$. Then the beating between the second harmonic of cavity 1 and the fundamental frequency of cavity 2 determines the period of oscillations of the frequency of the laser light. In Fig. 3.4, the frequency of 141.0 MHz corresponding to the peak represents the average of the second harmonic, 150 MHz, of cavity 1 and the fundamental frequency, 131 MHz, of cavity 2.

Again, if we change the cavity lengths so that the two fundamental cavity frequencies are $f_{\text{ext1}} = 70.2$ MHz and $f_{\text{ext2}} = 189.3$ MHz, respectively, the third harmonic of cavity 1 becomes much closer to the fundamental frequency of cavity 2. Then the frequency of the system is given by the average of the third harmonic of cavity 1 and the fundamental frequency of cavity 2, viz. the frequency of 201.7 MHz corresponding

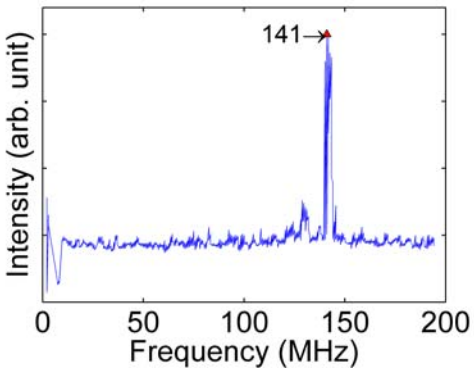

Figure 3.4. With the fundamental cavity frequencies $f_{\text{ext1}} = 75$ MHz and $f_{\text{ext2}} = 131.4$ MHz and at equal feedback strengths from the two cavities, a weighted average frequency between the second harmonic of cavity 1 and the fundamental frequency of cavity 2 is seen in the experimentally observed spectrum with feedback rates $\kappa_1 = \kappa_2 = 0.0045$, time delays $\tau_1 = 1250$, $\tau_2 = 680$, filter bandwidths $\Lambda_1 = \Lambda_2 = 0.012$, and detunings $\Delta_1 = \Delta_2 = -0.007$.

to the peak in Fig. 3.5 can be written as $\approx \frac{3f_{\text{ext1}}+f_{\text{ext2}}}{2} = 200.0$ MHz. In this case, $|3f_{\text{ext1}} - f_{\text{ext2}}| < |2f_{\text{ext1}} - f_{\text{ext2}}| < |f_{\text{ext1}} - 2f_{\text{ext2}}|$. We observe in the simulations that, in general, the laser selects the two frequencies whose difference is the smallest and the induced frequency of the dynamics is the weighted average of these two frequencies. This is confirmed in the experiments after changing the cavity lengths to make $2f_{\text{ext1}} \approx f_{\text{ext2}}$ and $3f_{\text{ext1}} \approx f_{\text{ext2}}$.

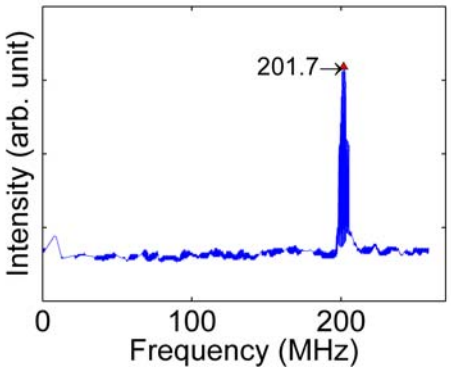

Figure 3.5. With the fundamental cavity frequencies $f_{\text{ext1}} = 70.2$ MHz and $f_{\text{ext2}} = 189.3$ MHz, and at equal feedback strengths from the two cavities, a weighted average frequency between the third harmonic of cavity 1 and the fundamental frequency of cavity 2 is seen in the experimentally observed spectrum with feedback rates $\kappa_1 = \kappa_2 = 0.0045$, time delays $\tau_1 = 1341$, $\tau_2 = 445$, filter bandwidths $\Lambda_1 = \Lambda_2 = 0.012$, and detunings $\Delta_1 = \Delta_2 = -0.007$.

In addition to the fundamental frequency, there are also higher harmonics that are induced in the single FOF. Figure 3.6 shows the RIN spectra when the laser is subjected to a single FOF. The fundamental frequency, 75.1 MHz, and the second harmonic are both present. Unique to two FOFs, the fundamental frequency is found to be suppressed as the second feedback field is switched on, and also, the amplitude of the second harmonic becomes larger than that of the fundamental frequency. This is shown both experimentally in Fig. 3.7 and numerically in Ref. [52]. The ratio of the amplitudes of the second harmonic to the fundamental frequency increases as the ratio of feedback rates $\kappa_2 : \kappa_1$ increases.

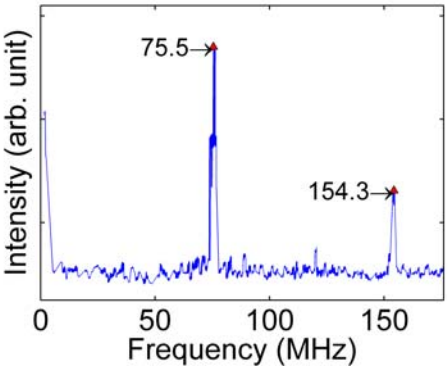

Figure 3.6. For the laser subject to a single FOF, (a) experimentally measured frequency spectrum, and (b) numerically simulated matching spectrum, with feedback rate $\kappa_1 = 0.01$, time delay $\tau_1 = 1248$, filter bandwidth $\Lambda_1 = 0.012$ and detuning $\Delta_1 = -0.013$.

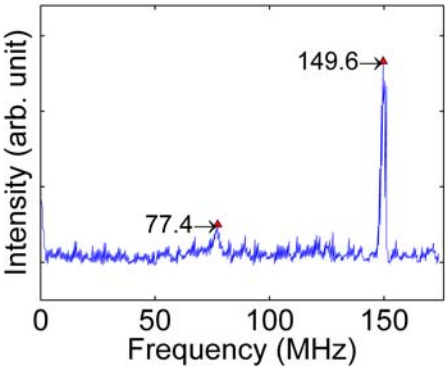

Figure 3.7. For the laser subject to two FOFs, experimentally measured spectrum at the feedback ratio $\kappa_2 : \kappa_1 = 1 : 4$

Single FOF studies have shown that in addition to frequency oscillations which are determined by the external round trip time, oscillations corresponding to twice the period are possible within certain regimes [46]. We have observed similar behaviors for a two FOF system. After changing the cavity length in the experiment so that the two fundamental cavity frequencies are 104 MHz and 119 MHz, we observe a weighted average frequency of 108 MHz, as described earlier. In addition, we observe a peak at 54 MHz, which corresponds to the period doubling behavior, shown in Fig. 3.8. Numerically, this period doubling behavior is obtained by simulating the spectrum of the frequency oscillations ($\dot{\phi}_{F_1}$) of the feedback intensity I_{F_1}. The peak corresponding to frequency f_1 is the period doubled frequency of the weighted average f_2.

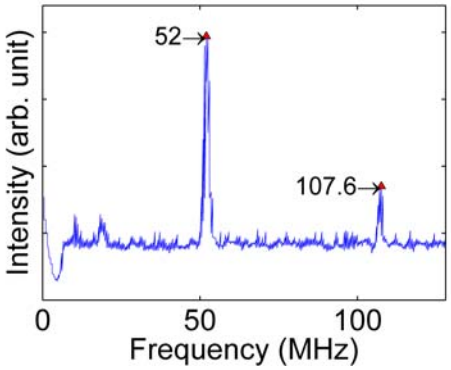

Figure 3.8. Frequency spectra showing period doubling of the weighted average frequency: experimentally measured with time delays $\tau_1 = 862$, $\tau_2 = 740$, filter bandwidths $\Lambda_1 = \Lambda_2 = 0.01$, detunings $\Delta_1 = \Delta_2 = -0.007$, and feedback rates $\kappa_1 = 0.016$, $\kappa_2 = 0.008$.

In contrast to the averaging between the fundamental and the higher harmonics, there occurs a weighted average of the period doubled frequency of one cavity and the fundamental of the other. Experimentally, this was observed for the cavity lengths corresponding to the fundamental frequencies of 180.0 MHz and 122.4 MHz. Figure 3.9 shows the weighted average of the period doubled frequency of 90 MHz and the fundamental of 122.4 MHz. This is numerically reproduced in Fig. 3.9. It is interesting to note that this behavior is consistent with the generalization that the laser chooses

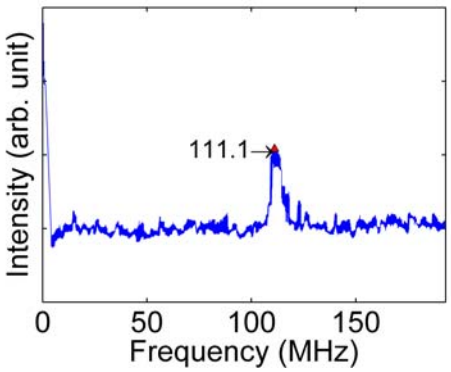

Figure 3.9. Frequency spectra showing a weighted average at 110.2 MHz between the fundamental of one cavity and the period doubled frequency of the other cavity: experimentally observed with feedback rates $\kappa_1 = 0.003$, $\kappa_2 = 0.0018$, time delays $\tau_1 = 734$, $\tau_2 = 222$, filter bandwidths $\Lambda_1 = 0.012$, $\Lambda_2 = 0.003$, and detunings $\Delta_1 = \Delta_2 = -0.007$.

the frequency which results in the smallest difference between the frequencies present, i.e., in this case $|\frac{1}{2}f_{\text{ext1}} - f_{\text{ext2}}| < |f_{\text{ext1}} - f_{\text{ext2}}| < |2f_{\text{ext2}} - f_{\text{ext1}}|$.

3.5.2 Bifurcation analysis

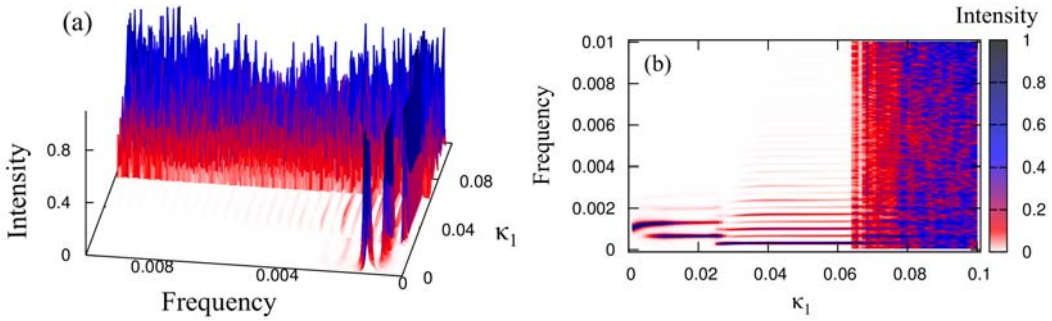

Figure 3.10. With time delays $\tau_1 = 1333$, $\tau_2 = 793$, feedback rate $\kappa_2 = 0.003$, filter bandwidths $\Lambda_1 = \Lambda_2 = 0.005$, detunings $\Delta_1 = \Delta_2 = -0.007$, and asymmetry parameter $\eta = 1$, the spectral bifurcation diagram of the two-FOF laser as the feedback rate κ_1 is varied: (a) the three-dimensional view, and (b) the density map of the combined laser intensity spectra.

In order to explore the dynamics at different values of the parameters κ_1 and κ_2, we use a bifurcation analysis. This study is performed by using the method of spectral bifurcation diagram [60]. In this method, the diagram is composed by combining the intensity spectra at different values of the parameter into a continuous intensity histogram. The intensity of the peaks in each spectra is normalized to its maximum value of 1. The parameters used in the simulation are $\tau_1 = 1333$, $\tau_2 = 793$ and $\kappa_2 = 0.003$. We vary the feedback rate κ_1 while the other parameters are kept fixed. At the low value of κ_1, the laser dynamics shows single period oscillations. A further increase in κ_1, e.g., to 0.005, causes a period doubling in the laser dynamics. This period doubling continues up to the value of $\kappa_1 = 0.025$, and after that a period quadrupling occurs. This quadrupling behavior changes into the quasi-periodic solution as κ_1 is further increased. A further increase in the κ_1, e.g., to ~ 0.07, leads

to the dynamics in the chaotic regime, as shown in Figs. 3.10(a) and 3.10(b). This analysis suggests that there is a cascade of period doubling bifurcations, resulting in a final chaotic state.

3.6 Conclusions

In a semiconductor laser subject to filtered optical feedback, we have shown that a second feedback plays an important role in controlling the frequency oscillations of the laser light. The period of oscillations of the frequency of the laser light is determined by the time delays of the two feedback loops. The frequency corresponding to this period represents the weighted average of cavity 1 and cavity 2. The average frequency is dependent on the relative feedback from both cavities and corresponds to the weight between them. A proper adjustment of the cavity lengths leads to the oscillations at the frequency which represents the average of the higher harmonics of one cavity and the fundamental frequency of the other cavity. In general, the laser selects the two frequencies whose difference is the smallest and averages between these two frequencies. We have also found that the amplitudes of fundamental and second harmonic of single FOF are modified due to the addition of a second FOF, and in particular, by varying the strength of the second feedback, the amplitude of the fundamental frequency is suppressed while the amplitude of the second harmonic becomes larger than that of the fundamental frequency. The ratio of the amplitudes of the second harmonic and the fundamental frequency increases as the feedback ratio $\kappa_2 : \kappa_1$ increases. A cascade of period doubling bifurcation is also found in the two-FOF laser. Indeed, we further explore this bifurcation in the next chapter by including the effects of quantum noise. The effects of noise were included in order to reconcile a quantitative difference between the deterministic simulations and the experimental bifurcation route. In addition, we examine the effects of noise for different bandwidth and feedback strength regimes.

As mentioned in the Introduction, semiconductor lasers with feedback have served as model systems for chaotic cryptography, random number generation etc., and thus the present study, which provides additional control parameters could be used to investigate some of these applications. The technique of single filtered optical feedback reported in [34,43,45,47] has been used to control and manipulate semiconductor laser dynamics. Our present work with two filtered optical feedbacks has shown to lead to a rich control over the laser dynamics. Thus the results presented in this paper can be very useful for the development of an efficient technique to manipulate the dynamical response of a semiconductor laser from the view point of engineering.

4. Effects of Quantum Noise on the Dynamics

Main results of this chapter have been published in Ref. [61]

This chapter describes the numerical investigation on the influence of quantum noise on the dynamics that arise in a semiconductor laser subject to two FOF. This is a continuation of our experimental work described in the previous chapter, wherein a period-doubling route to chaos was numerically observed. This chapter reconciles the discrepancy between the deterministic simulations of a period-doubling route and experimental results by including the effects of noise in the feedback model. We demonstrate that in the presence of quantum noise the feedback strength required to induce chaotic dynamics is greater than the deterministic value. In addition, we discuss the effects of noise on dynamics for different filter bandwidths. Three bandwidth regimes are explored, viz. a narrow, intermediate, and wide bandwidth. In our investigation we change one bandwidth while the second remains constant. Finally, we discuss our results to give an overall picture of the role of noise on the dynamics.

4.1 Introduction

Recently, there has been an interest in the dynamics of a SCL subject to two simultaneous FOFs [59, 62, 63]. The vast number of parameters available allows researchers to explore many different avenues. Krauskopf and co-workers have reported an exhaustive study of the bifurcations that arise in such systems [64, 65]. Not only has a theoretical interest in two FOF gained traction, but this system is providing an excellent test-bed for applied research. An interesting application recently reported is the ability to study state-dependent switching in a photonic system consisting of two FOF [63]. Martinez-Llinas (fix name) and co-workers observed that the system

behaved as if it were subject to only one of the two external cavities depending on the state of the system [63]. The model in Ref. [63] is identical to deterministic rate equations we use in the previous chapter (see Ref. [52]).

We discussed in the previous chapter our experimental study on the frequency dynamics in the light from the laser when subject to two FOFs [52]. Among the more interesting observations was the generation of new frequencies in the system, and the results were explained via a theoretical model that consisted of the usual Lang-Kobayashi rate equations augmented to include two FOFs. The agreement between experiments and theory was excellent.

One of the observations that emerged from our work was that the frequency of laser light in a SCL subject to two FOFs follows a period-doubling route to chaos. However, the feedback strength necessary for coherence collapse that was predicted by the theoretical model was higher than what was observed experimentally. This mismatch between theory and experiment inspired us to examine the role of unavoidable quantum noise in the laser and its influence on the dynamics of the laser. To this end, we have augmented the theoretical model with Langevin noise terms to account for the spontaneous emission noise as well as inversion noise. To give one a picture of the system studied, we show a schematic of the experimental design [Fig.4.1] highlighting the key parameters accessible to experiment, which are detailed in the following section.

4.2 Model

A semiconductor laser with FOF from a single cavity can be modeled with a set of rate equations describing the time evolution of the slowly varying complex electric fields, $E(t)$ and $F(t)$, of the laser and feedback field, respectively, and the carrier inversion $N(t)$ [43]. Our setup [Fig. 4.1], which includes two cavities, each with a

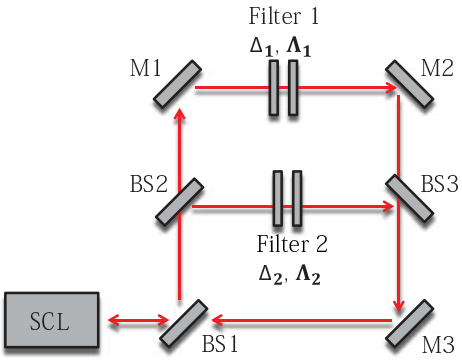

Figure 4.1. The schematic shows a semiconductor laser (SCL) subject to optical feedback from two external cavities. The outer cavity (1) is formed by the SCL and the mirrors (M1, M2, and M3). The inner cavity (2) is formed by the SCL, beam splitters (BS2 and BS3), and mirror (M3). Each cavity contains a Fabry-Perot resonator acting as a spectral filter, which can be modified by changing the reflectivity or spacing of the filter mirrors. This in turn changes the bandwidth, Λ. The detuning, Δ, is altered by adjusting the pump current. The delay-times, τ_1 and τ_2, are increased or decreased by lengthening or shortening the cavities.

spectral filter, must therefore include two filtered feedback fields, $F_1(t)$ and $F_2(t)$, resulting in the following description,

$$\frac{dE}{dt} = \frac{1}{2}(1+i\alpha)\xi N(t)E(t) + \kappa_1 F_1(t,\tau_1) + \kappa_2 F_2(t,\tau_2) + L_E(t), \tag{4.1a}$$

$$\frac{dN}{dt} = J - J_{thr} - \frac{N(t)}{T_1} - [\Gamma_0 + \xi N(t)]|E(t)|^2 + L_N(t), \tag{4.1b}$$

$$\frac{dF_1}{dt} = \Lambda_1 E(t-\tau_1)\mathrm{e}^{-i\omega_0\tau_1} + (i\Delta_1 - \Lambda_1)F_1(t). \tag{4.1c}$$

$$\frac{dF_2}{dt} = \Lambda_2 E(t-\tau_2)\mathrm{e}^{-i\omega_0\tau_2} + (i\Delta_2 - \Lambda_2)F_2(t), \tag{4.1d}$$

where ξNE in the first term of Eq. (4.1a) accounts for the growth (or decay) when the carrier inversion $N(t)$ is above (or below) threshold, and ξ is the differential gain coefficient. α is the linewidth enhancement factor which quantifies the phase-amplitude coupling. The second (third) term in Eq. (4.1a) accounts for the feedback field $F_1(t,\tau_1)$ ($F_2(t,\tau_2)$), where κ_1 (κ_2) is the feedback rate and τ_1 (τ_2) is the time delay due to the propagation of the feedback field in cavity 1 (2).

The rate equation for the carrier inversion [Eq. (4.1b)] depends on the difference between the pump current J and the threshold current J_{thr}. The second term [Eq. (4.1b)] accounts for the spontaneous decay, hence T_1 is the carrier decay rate, and the third term includes the stimulated emission, where Γ_0 is the photon decay rate.

Eqs. (4.1c) and (4.1d) are derived by assuming that the response function, $r(\omega)$, of the filter is Lorentzian [43], i.e.

$$r(\omega) = \frac{\Lambda}{\Lambda + i(\omega - \Delta)}, \tag{4.2}$$

where ω is the instantaneous optical frequency, Λ is the half width at half maximum (HWHM) of the filter and Δ is the detuning of the solitary laser frequency from the center frequency of the filter. The explicit dependence on the time-delayed fields $E(t - \tau_{1,2})$ is seen in Eqs.(4.1c) and (4.1d). The feedback phase accumulated due to the propagation of the field through cavity 1 (2) is given by $\omega_0\tau_1$ ($\omega_0\tau_2$), which we assume equal for the two cavities and fix at $\omega_0\tau_1 = \omega_0\tau_2 \equiv \theta$. The spontaneous-recombination noise terms are described by $L_E(t)$ and $L_N(t)$. Both noise sources are assumed to be Gaussian with zero mean. Their autocorrelation functions are given by,

$$\langle Re(L_E(t))Im(L_E(t'))\rangle = 0, \tag{4.3a}$$

$$\langle Re(L_E(t))Re(L_E(t'))\rangle = \langle Im(L_E(t))Im(L_E(t'))\rangle = R_{sp}\delta(t - t'), \tag{4.3b}$$

$$\langle L_N(t)L_N(t')\rangle = D\delta(t - t'). \tag{4.3c}$$

The rate of spontaneous emission is written as $R_{sp} = \beta_{sp}CN^2$, where β_{sp} is the fraction of spontaneous emission coupled into the dominant mode and C is a radiative recombination rate [5]. The shot noise diffusion rate is given by D. The noise sources L_E and L_N are derived quantum mechanically in order to arrive at their explicit form and statistical properties [50]. Although the noise sources are correlated in a SCL [50], we found that correlating sources resulted in no significant difference when compared to uncorrelated noise [51]. Therefore, the proceeding analysis is done with uncorrelated noise.

Eqs. (4.1) are integrated using a modified fourth order Runge-Kutta method. The time step was varied from 0.1 ps to 10 ps in order to ensure consistent dynamical behavior independent of the integration step size. The modified Runge-Kutta method accounts for the Langevin noise source and avoids an infinite variance of the stochastic terms following the stochastic Runge-Kutta algorithm outlined in Ref. [66]. At each integration step, the noise terms are pulled from a matrix of normally distributed random numbers generated via the *randn()* function in MATLAB. In order to account for the time delayed fields, a history function is built by initially integrating Eqs. (4.1) without feedback ($\kappa_{1,2} = 0$). The transient behavior is discarded and the history function with a minimum integration time of $4\tau_{1,2}$ is saved. The remaining parameters and noise strengths for a typical edge emitting SCL are highlighted in Table 5.1.

We point out that this system contains a rich variety of parameters that are accessible in an experiment. Adjusting the pump current J controls the optical frequency, which in turn changes the detuning $\Delta_{1,2}$. Changing the filter mirror spacing or reflectivity modifies the bandwidth $\Lambda_{1,2}$, and the time delays $\tau_{1,2}$ are directly proportional to the external cavity lengths $L_{1,2}$. The feedback rates $\kappa_{1,2}$ are controlled via a neutral density filter inserted in each cavity.

4.3 Results: a period doubling route to chaos

This section describes the results of our work, but before doing so it is important to point out that the 2FOF system has a large set of parameters, each of which can influence the resulting dynamics. We have, therefore, focused on a limited set which highlights the role of quantum noise. For example, we have chosen typical noise strengths and have not varied the strength of the noise. Furthermore, we have fixed the bandwidth of one of the filters to 1GHz, the so-called intermediate bandwidth which lies between the external cavity mode spacing frequency and the laser relaxation oscillation (RO) frequency, and varied the bandwidth of the second filter to study the effects of filter bandwidth.

Table 4.1.
The parameter values for a typical SCL which are used in the simulations (unless otherwise specified).

Quantity	Symbol	Value
Linewidth enhancement factor	α	5
Feedback rate field 1	κ_1	Varies
Feedback rate field 2	κ_2	0.8 GHz
Bandwidth of filter 1	Λ_1	Varies
Detuning of filter 1	Δ_1	Varies
Bandwidth of filter 2	Λ_2	1.0 GHz
Detuning of filter 2	Δ_2	-1.5 GHz
Delay-time field 1	τ_1	14.28 ns
Delay-time field 2	τ_2	7.93 ns
Phase accumulation	θ	1.111
Differential gain coefficient	ξ	5×10^3 s^{-1}
Photon decay rate	Γ_0	10^{11} s^{-1}
Carrier decay rate	T_1	1 ns
Threshold pump rate	J_{thr}	1×10^{17} s^{-1}
Pump rate	J	$1.5J_{thr}$
Spontaneous emission rate	R_{sp}	5×10^{12} s^{-1}
Shot noise diffusion rate	D	1.45×10^{16} s^{-1}

We begin by describing the results of our calculations, shown in Fig. 4.2, which exhibits a period doubling route to chaos of the frequency $\omega(t)$ of the laser wavelength (instantaneous frequency) oscillations. The period doubling route is produced via the bifurcation parameter κ_1, which is the feedback rate of field 1. The color scheme corresponds to the amplitude of the oscillations. All other parameters are fixed as specified in Table 5.1 except the filter bandwidth and detuning, where $\Lambda_1 = 1$ GHz

and $\Delta_1 = -0.5$ GHz. Initially the feedback is solely from cavity 2 ($\kappa_2 = 0.8$ GHz and $\kappa_1 = 0$ GHz). We calculate the time series for $E(t)$, $F_{1,2}(t)$, and $N(t)$. Using the complex electric field $E(t)$ we extract the phase $\phi(t)$, where $\phi(t) = arg(E(t))$. $arg(z)$ is the typically defined complex argument of z. The frequency $\omega(t)$ of the slowly varying complex electric field $E(t)$ is found by calculating the time derivative of the phase [$\omega(t) = \dot{\phi}(t)$]. Finally, the numerical spectra are determined for $E(t)$ and $\omega(t)$ after discarding the transient behavior. The feedback rate κ_1 is increased by $\Delta\kappa_1 \approx 0.32$ GHz and this process is repeated over 32 iterations in order to arrive at a final feedback rate of $\kappa_1 = 10$ GHz. In the presence of noise, this procedure is averaged over 1000 instances. These spectra are stitched together resulting in a period doubling route to chaos shown in Fig. 4.2. Examining the deterministic period doubling map [Fig. 4.2a], the first frequency (labeled f_I) to emerge is 105 MHz corresponding to the fundamental frequency from cavity 2 ($f_2 \approx \frac{1}{\tau_2 + 1/\Lambda_2} \approx 107$ MHz). Note that the fundamental frequency, which we label as f_{fun}, for FOF is dependent on both the delay time τ and the bandwidth Λ. κ_1 is increased and a frequency (f_{II}) of 130 MHz is produced which corresponds to an average between the fundamental frequency of cavity 2 and the second harmonic of cavity 1 ($\frac{f_2 + 2f_1}{2} \approx 125$ MHz). A further increase in κ_1 results in a quasi period-doubling route to chaos. Examining the deterministic case in Fig. 4.2a, it is clear that the onset of chaos begins at $\kappa_1 \approx 4.5$ GHz. When noise is present, shown in Fig. 4.2b, the period doubling route for smaller frequencies is drastically altered. The onset of chaos is delayed and a spread in the spectrum does not emerge until $\kappa_1 \approx 7$ GHz. Not only is the chaotic regime shifted to a larger feedback rate, but the frequency content is altered. The stochastic spectra, which are extended to 5 GHz and shown in Fig. 4.2c, also depict a change near $\kappa_1 \approx 4.5$ GHz. The deterministic spectra (not shown) are very similar when depicted on the same scale. One gains an insight into the mechanism for this delay by examining the dynamics at different parameters in more detail.

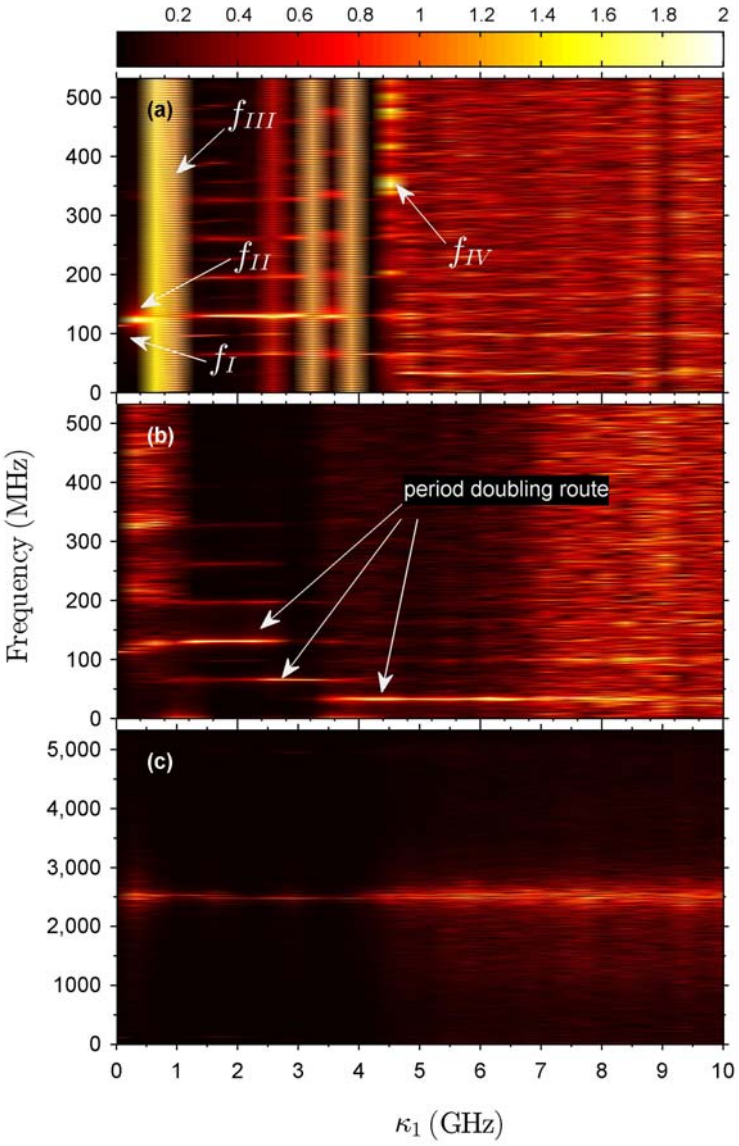

Figure 4.2. Deterministic (a) and stochastic [(b),(c)] density plots of the period doubling route to chaos when the feedback strength κ_1 from cavity 1 is increased. The bandwidth and detuning are fixed at $\Lambda_1 = 1$ GHz and $\Delta = -0.5$ GHz, otherwise all other parameters are recorded in Table 5.1. f_{I-IV} are the frequencies discussed in this text which differ significantly in the stochastic period doubling route. Note that (c) contains the stochastic spectra extended out to 5 GHz.

4.3.1 Influence of noise

Previous studies of a SCL subject to FOF demonstrated that noise influences the dynamics substantially [51, 67]. They showed that multiple attractors exist for the deterministic dynamics, and in the presence of noise some of the attractors no longer survive [51]. The argument followed that noise helps determine whether a particular attractor is stable, analogous to that of a perturbation acting on a system at a maximum of a potential distribution. Other studies have shown that noise induces jumps between stable attractors if the ratio of the noise strength to potential barrier is large enough [67]. A good understanding of this behavior is gained via an examination of the time-series in conjunction with the phase-portraits and rf spectra. The previous studies investigated particular instances of a parameter space, while we focus on the period-doubling route to chaos as the feedback strength is increased. Using these tools with the addition of first return maps, the period doubling route is traced along increasing feedback strength κ_1. The return map is generated by determining the maximum values (ω_{max}) for each oscillation in the time series $\omega(t)$. Thus a series of maximum values is generated, and $\omega_{(max)\,n+1}$ is compared to the previous value at $\omega_{(max)\,n}$.

Fig. 4.3 depicts four deterministic plots and four stochastic plots. When the feedback strength is $\kappa_1 = 0$ GHz, the three corresponding plots are the instantaneous frequency $\omega(t)$ time series (a1 and b1), the phase plane of the frequency ω_n and phase difference $\eta = \phi(t) - \phi(t-\tau)$ (a2 and b2), and the rf spectrum of $\omega(t)$ (a3 and b3). We note, when comparing the deterministic (a3) and stochastic (b3) rf spectra, that the perturbation of noise does not affect the dominant frequencies in time-delay regime, even though the time-series are clearly different. This difference is noted in the large rf spectra (a4 and b4), where in the presence of noise (b4) the ROs are undamped. However, as we increase the feedback strength κ_1, noise plays a significant role in determining the dominant frequencies.

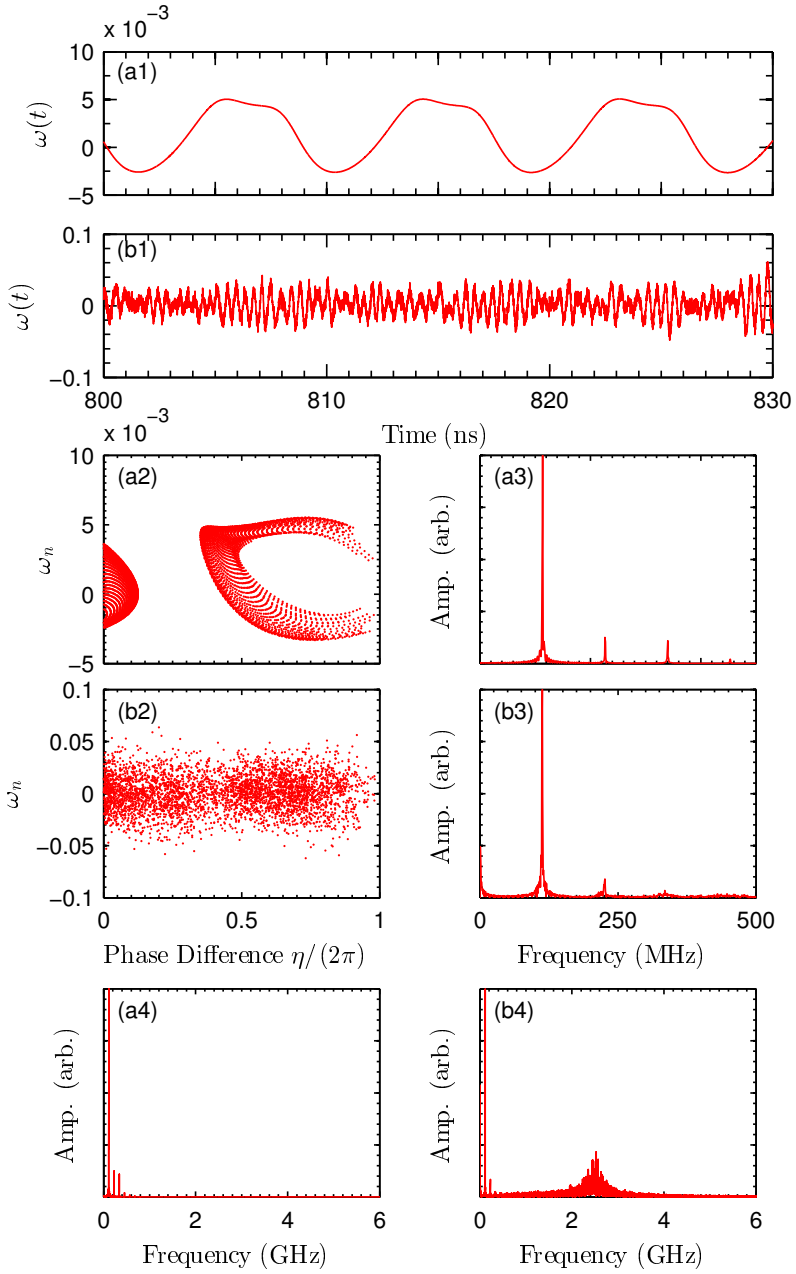

Figure 4.3. Deterministic (a) and stochastic (b) plots of the frequency $\omega(t)$ time-series (1), the phase-plane of ω_n and η (2), and the rf spectrum (3) showing a fundamental frequency of $f_{fun} \approx 123$ GHz. The plots are calculated when the feedback is injected solely from cavity 2 ($\kappa_1 = 0$ GHz). The rf spectra (a4) and (b4) are extended out to 6 GHz in order to depict the undamping of the ROs seen in the time-series (b1).

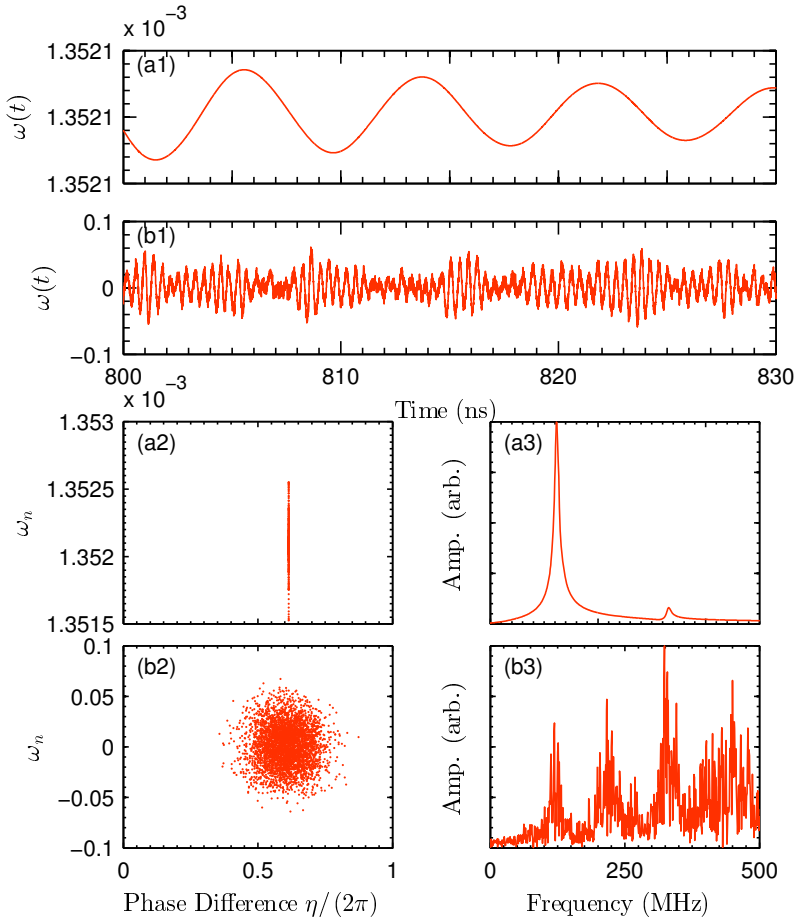

Figure 4.4. Deterministic (a) and stochastic (b) plots of the frequency $\omega(t)$ time-series (1), the phase-plane of ω_n and η (2), and the RIN spectrum (3) when the feedback strength is κ_1 =0.32 GHz. The deterministic time-series captures a transient behavior toward a steady-state behavior.

Once the feedback from the first cavity is allowed ($\kappa_1 = 0.32$ GHz), as shown in Fig. 4.4, the deterministic and stochastic rf spectra [(a3) and (b3)] show clear differences. The differences can be understood by examining the deterministic and stochastic time series [(a1) and (b1)] and phase portraits [(a2) and (b2)]. From the time series (a1), it is clear that the frequency $\omega(t)$ is always positive and $\omega(t)$ evolves toward a steady-state. The movement toward a steady state (fixed point) is depicted in the deterministic phase portrait (a2). The dominant frequency in the deterministic spectrum (a3) is ~ 125 MHz. In the presence of noise (b3), the peak at ~ 125 MHz is reduced and the peak at ~ 337 MHz is enhanced. In addition, the frequency, shown in the stochastic time series (b1), oscillates around $\omega = 0$. We note that this shift in the frequency toward $\omega = 0$ is a general feature when noise is included in the simulations. For this feedback strength ($\kappa = 0.32$ GHz), the shift occurs because the fixed point no longer survives in the presence of noise. The absence of the fixed point is clearly depicted when one compares the deterministic and stochastic return maps, shown in Fig. 4.5. Examining the return map (Fig. 4.5), the deterministic maxima (blue circles) show little variance and are centered at the fixed point, while the stochastic maxima (red triangle) spread and are no longer centered at the same location. Instead, noise drives the system toward higher frequencies coinciding with higher harmonics shown in the rf spectrum of Fig. 4.4(b3).

At a feedback strength of $\kappa_1 = 0.97$ GHz, the time-series in Fig. 4.6 shows periodic oscillations with a period of $1/f_{RO} = 400$ ps, where f_{RO} is the frequency of the ROs. This behavior corresponds to the undamping of the ROs, which then become the dominant feature. This undamping of the ROs is a well studied phenomenon of a SCL subject to optical feedback, where the ROs are an exchange of energy between the photons and the inversion carriers when the SCL is externally perturbed [8, 50]. The frequency of these oscillations occur near $f_{RO} \approx 2.5$ GHz and varies depending on the SCL design and parameters. The phase portrait [Fig. 4.6(a2)] shows a periodic attractor, which does not survive in the presence of noise [Fig. 4.6(b2)].

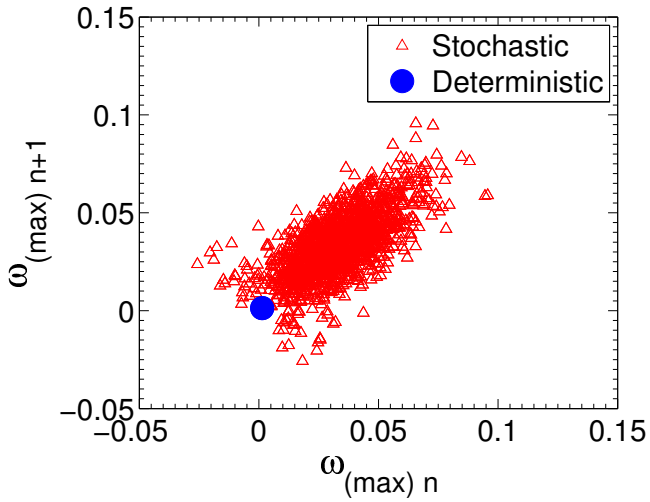

Figure 4.5. First return maps for feedback strength of κ_1 =0.32 GHz showing both the stochastic (red triangle) and deterministic (blue circle) locations of ω_{max}.

The extinction of this attractor allows the time-delay oscillations to influence the global behavior seen in the stochastic rf spectrum [Fig. 4.6(b3)].

Signatures of the ROs in the dynamics occur at three instances along the bifurcation map of Fig. 4.2(a) at $\kappa_1 = 0.97$ GHz (f_{III} on the map), $\kappa_1 = 3.1$ GHz, and $\kappa_1 = 3.5$ GHz. Each instance displays the same behavior characterized by frequency oscillations with a period of $1/f_{RO} = 400$ ps and the existence of a limit cycle in the phase-portrait. However, in each case, this attractor no longer survives in the presence of noise. Noise drives the system toward periodic oscillations which are dictated by the delay time and filter bandwidth.

Turning our attention to the period doubling maps [Fig. 4.2], we note that the transition into chaotic deterministic dynamics begins at a feedback strength of $\kappa_1 \approx 4.5$ GHz (f_{IV} on the map), and in presence of noise the onset of a chaotic transition is clearly delayed ($\kappa_1 \approx 7.0$ GHz). Fig. 4.7 displays this critical transition at a feedback $\kappa_1 = 4.52$ GHz for the deterministic onset of chaos. The frequency $\omega(t)$ not only oscillates with a period of $1/f_{RO}$ but exhibits an envelope of slower oscillations which are shown in the time series (a1) and spectrum (a2) of Fig. 4.7. The return map in Fig. 4.8(a) suggests stable periodic oscillations demonstrated by the small variance in the deterministic maximum values (blue circle) of the frequency ω_{max}. Comparing this to the stochastic dynamics, the corresponding behaviors are very different. Shown in Fig. 4.7(b2), the attractor no longer survives and the spectrum [Fig. 4.7(b3)] greatly differs. The spectrum contains a period doubled frequency located at $f_{dom}/2 = 62$ MHz. Here we define f_{dom} as the dominant frequency which corresponds to the weighted average between the two fundamental frequencies of each cavity. Once again, the dominant frequency in the presence of noise is dictated by the FOF time scales (τ and Λ).

The return maps in Fig. 4.8 for feedback strengths $\kappa_1 = 4.84$ GHz [Fig. 4.8(b)] and $\kappa_1 = 5.16$ GHz [Fig. 4.8(c)] provide an excellent representation of the difference between the deterministic and stochastic dynamical states. Comparing all three return maps [Fig. 4.8a,b, and c], the stochastic maxima (red triangles) reveal a departure

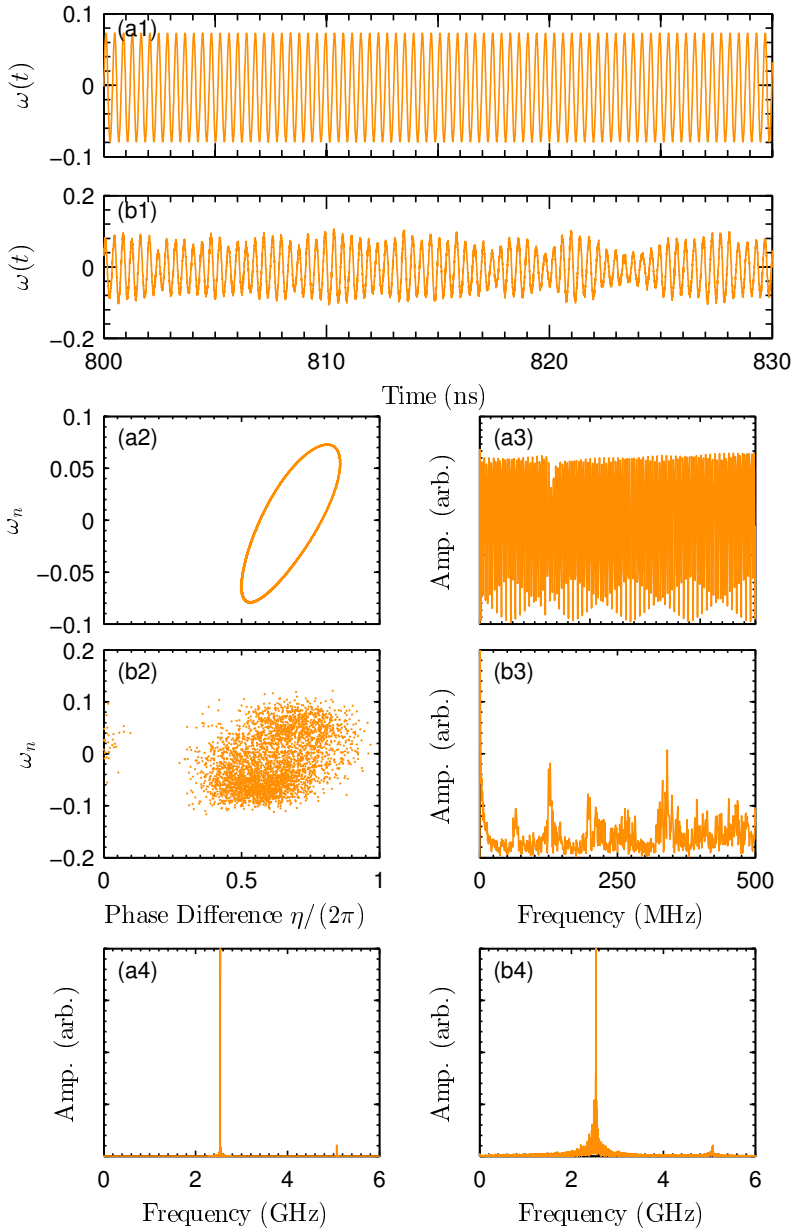

Figure 4.6. Deterministic (a) and stochastic (b) plots of the frequency $\omega(t)$ time-series (1), the phase-plane of ω_n and η (2), and the rf spectrum (3) when the feedback strength is κ_1 =0.97 GHz. The deterministic time-series and phase-portrait show periodic behavior with a frequency of $f_{RO} \approx 2.5$ GHz, which is shown in the extended spectra (a4) and (b4).

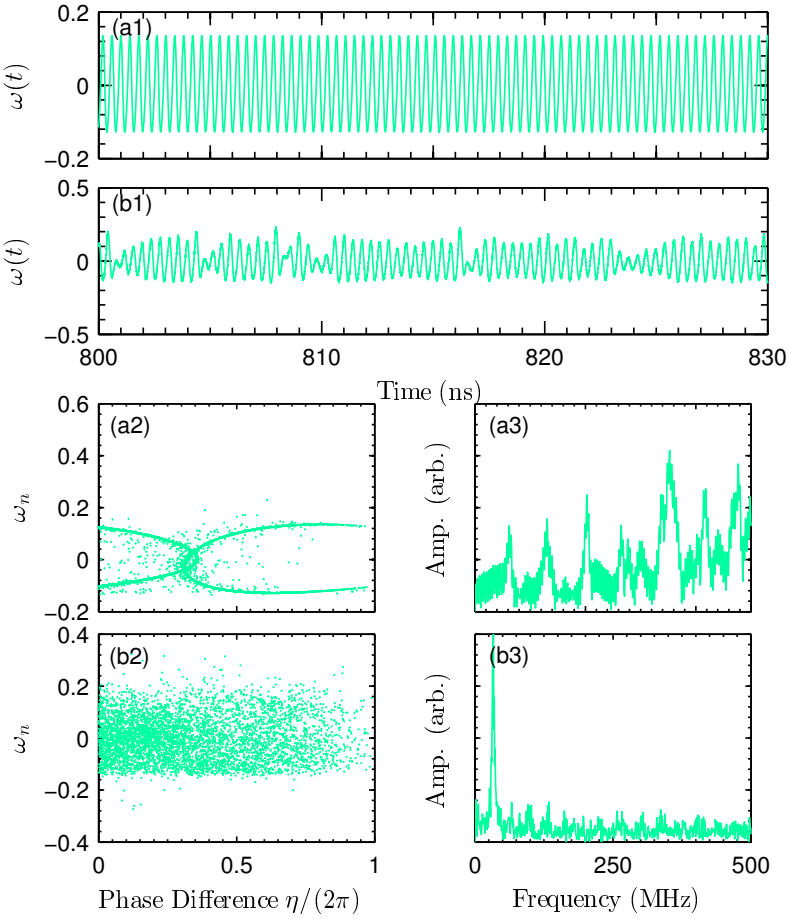

Figure 4.7. Deterministic (a) and stochastic (b) plots of the frequency $\omega(t)$ time-series (a1 and b1), the phase-plane of ω_n and η (a2 and b2), and the rf spectrum (a3 and b3) when the feedback strength is κ_1 =4.52 GHz.

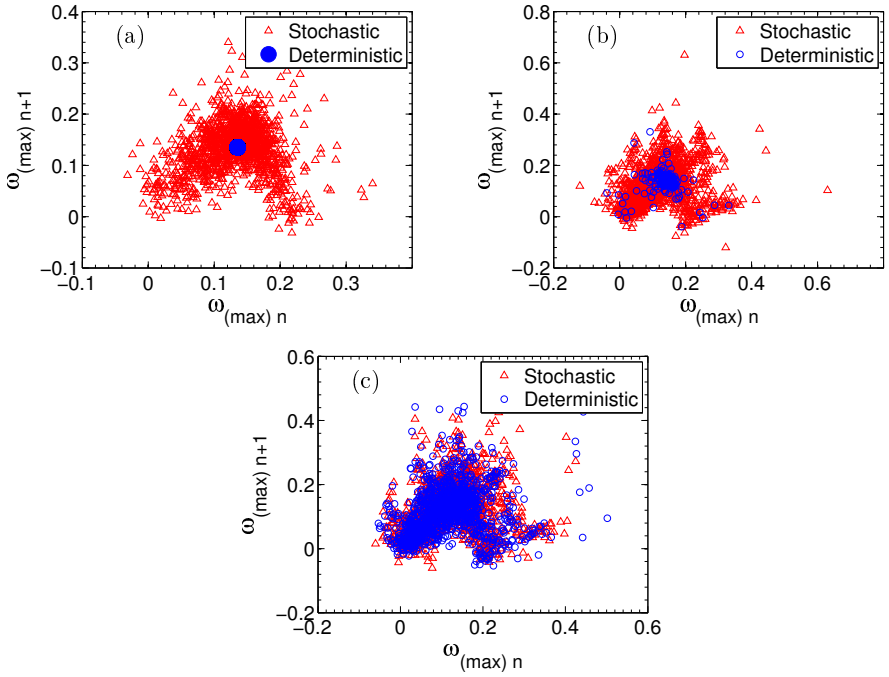

Figure 4.8. First return maps for feedback strength of (a) κ_1 =4.52 GHz, (b) κ_1 =4.84 GHz, and (c) κ_1 =5.16 GHz showing both the stochastic (red triangle) and deterministic (blue circle) values.

from the linear shape at smaller feedback strengths (see Fig. 4.5). The deterministic maxima (blue circles) ω_{max}, however, require a larger feedback strength (κ_1 =5.16 GHz) in order to replicate stochastic maps. It is not until κ_1 =5.16 GHz [Fig. 4.8(c)] that the two maps become similar.

However, the similarity in the return maps [Fig. 4.8(c)] does not guarantee that the dynamical states will be identical. The difference between the stochastic and deterministic dynamics is manifested in the period doubling routes shown in Fig. 4.2, where two key differences standout. First, the lack of stable RO frequencies in Fig. 4.2(b) (stochastic), which are present in Fig. 4.2(a) (deterministic). An example of the RO frequency in Fig. 4.2(a) is displayed by the marker f_{III}. Second, the onset of chaos is delayed in Fig. 4.2(b) until a feedback strength of $\kappa_1 \approx 7$ GHz is reached. To explain these differences, it appears that multiple mechanisms play a role. Not only does noise limit the number of stable attractors, but noise drives the periodic oscillations toward the dynamics influenced by the time-delay and filter bandwidth.

4.4 Effects of the filter bandwidth on the dynamics

We next turn our attention to the effects of the two filter bandwidths on the dynamics. In a single FOF system, it is possible to identify three regimes depending on the magnitude of the bandwidth Λ relative to the RO frequency f_{RO} and relative to the external cavity mode (ECM) spacing. The effects of the filter width on the dynamics for each case have been outlined by Fischer [44], while other theoretical work has characterized the mode structures for the different bandwidth regimes [47]. Our previous bifurcation analysis was done for bandwidths of equal magnitudes, $\Lambda_1 = \Lambda_2 = 1$ GHz, which fall in an intermediate range. The intermediate range is where Λ is large enough to include a number of ECMs yet smaller than the frequency of the ROs. A narrow filter ($\Lambda \to 0$) was shown to resemble optical injection [68], while a wide filter ($\Lambda \to \infty$) was shown to resemble conventional optical feedback (COF), hence the latter case reduces to the standard Lang-Kobayashi rate equations [46].

In general, the most interesting dynamics occur in the intermediate regime, because in this regime the parameters of the filter (Λ and Δ) play an important role in determining both the stability and control of the dynamics [44].

The use of two filters is advantageous not only because of the additional parameters introduced (τ_2, Λ_2, Δ_2, *etc.*) but also because of the interplay between the two fields which results in novel dynamics and the possibility of robust control over these dynamics [52]. As stated earlier, we fix one filter Λ_1 in the intermediate regime while the other filter Λ_2 is varied. In particular, we focus on two cases. The first is a narrow filter $\Lambda_2 < \delta_{ECM}$, where δ_{ECM} is the frequency of the external cavity mode spacing. The second is a wide filter, $\Lambda_2 > f_{RO}$. We achieve this by varying the bandwidth of one filter over a large range from $\Lambda_2 = 0 \rightarrow 20$ GHz, while the second filter is fixed at $\Lambda_2 = 1$ GHz. We focus on these two cases in order to isolate the effects of both noise and the bandwidth. A study could be done of the narrow-narrow, wide-wide, or narrow-wide cases, but these would no longer contain any signatures of the spectrally filtered feedback. Rather, they would resemble injection and COF.

4.4.1 Feedback from an intermediate and narrow filter

In practice, one is not able to reduce the bandwidth indefinitely, therefore we restrict ourselves to the narrow filter where $0 < \Lambda < \delta_{ECM}$. Experimentally, the bandwidth of the filter can be modified by changing the mirror reflectivity of the filter or the mirror spacing. We study this system by keeping $\Lambda_2 = 1$ GHz while Λ_1 and Δ_1 are varied from 10 MHz to 50 MHz and -10 MHz to -50 MHz, respectively, where 50 MHz is slightly larger than the SCL linewidth. Along each iteration of the bandwidth, the detuning is varied such that the laser frequency lies at the same position of the filter profile. Similar to the period doubling map, the spectra are stitched together for different Λ_1 and Fig. 4.9 shows the resultant density plots of the intensities (1) $I_L(t)$, (2) $I_{F_1}(t)$, and (3) $I_{F_2}(t)$, where $I_L(t) = |E(t)|^2$, $I_{F_1}(t) = |F_1(t)|^2$, and $I_{F_2}(t) = |F_2(t)|^2$.

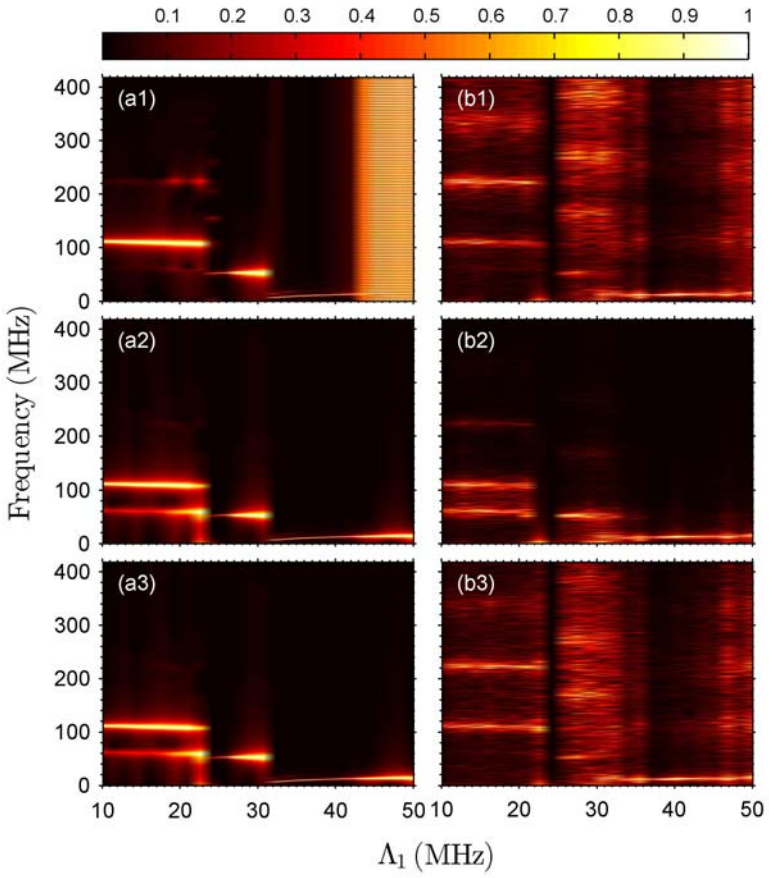

Figure 4.9. Deterministic (a) and stochastic (b) density plots of the amplitude of the spectrum as a function of changing bandwidth, Λ_1. The density plots correspond to the spectra for (1) $I_L(t)$, (2) $I_{F_1}(t)$, (3) and $I_{F_2}(t)$. Λ_2 is fixed at 1 GHz and the two feedback rates are kept constant at $\kappa_1 = 3$ GHZ and $\kappa_2 = 0.8$ GHz.

Initially, for the deterministic case, when Λ_1 is small (0 MHz $< \Lambda_1 <$ 20 MHz), the frequency of oscillations is $f_{dom} \approx 110$ MHz shown in Figure 4.9(a). This frequency of 110 MHz corresponds to the fundamental frequency of cavity 2. Using the parameters in Table 5.1, we find that $f_2 \approx 1/(\tau_2 + 1/\Lambda_2) \approx 112$ MHz. When Λ_1 is increased, a frequency of 50 MHz emerges, which is a consequence of the spectrally filtered feedback from cavity 1. The frequency of 50 MHz is an average between f_1 and f_2, where $f_1 \approx 1/(\tau_1 + 1/\Lambda_1) \approx 15$ MHz. The average, weighted toward f_1, is explained by the larger feedback rate from cavity 1 ($\kappa_1 > \kappa_2$). The dependence of the weighted average on the ratio of the feedback rates was reported in Ref. [52]. Continuing to increase Λ_1 results in a frequency of approximately 15 MHz, which is dominated by f_1. Upon further increase of Λ_1 the ROs become dominant which is evident in the time series plot in Fig. 4.11(a1). Note that these ROs are not present in Figs. 4.9(a2) and 4.9(a3) because, Λ_1 and Λ_2 act as low pass filters. The same density plots are then produced in the presence of noise shown in Fig. 4.9b. For all three plots in Fig. 4.9b, there is an absence of the broad 50 MHz frequency at a bandwidth of $\Lambda_1 = 32$ MHz.

The deterministic time series for $\Lambda_1 = 32$ MHz in Fig. 4.10(a1) shows the evolution of $I_L(t)$ toward a steady-state value and the phase portrait (a2) shows this fixed point attractor. Comparing this to the stochastic time series for $\Lambda_1 = 32$ MHz in Fig. 4.10(b1), it becomes evident that noise drives the system out of the fixed point, which was explained in our analysis above describing the period-doubling route to chaos. Comparing Fig. 4.11(a1) and Fig. 4.11(b1), it is clear that the relaxation oscillations are no longer the dominant frequency for the deterministic case at a larger bandwidth of $\Lambda_1 = 50$ MHz, rather the dominant frequency contains signatures of the FOF time scale in the rf spectrum shown in Fig.4.11(b3).

Although $\Lambda_1 < \delta_{ECM}$, we point out that the feedback from cavity 1 only resembles optical injection when the bandwidth is $\Lambda_1 <$ 25 MHz. This is observed by noting that the dynamics in the presence of cavity 1 alone, when $\kappa_2 = 0$ GHz (not shown), evolve to a steady-state fixed point for any bandwidth of Λ_1 up to 25 MHz. Beyond

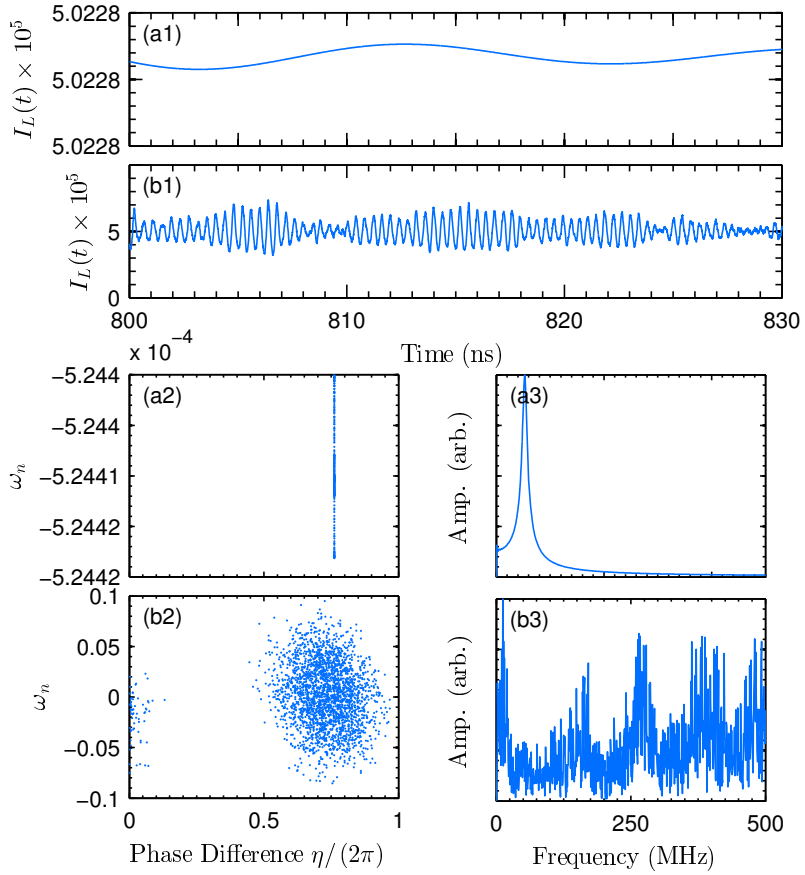

Figure 4.10. (1) Intensity time series $I_L(t)$, (2) phase portraits (η, P), and (3) rf spectrum in the absence of noise (a) and in the presence of noise (b) for a bandwidth of $\Lambda_1 \approx 32$ MHz and detuning $\Delta_1 = -32$ MHz.

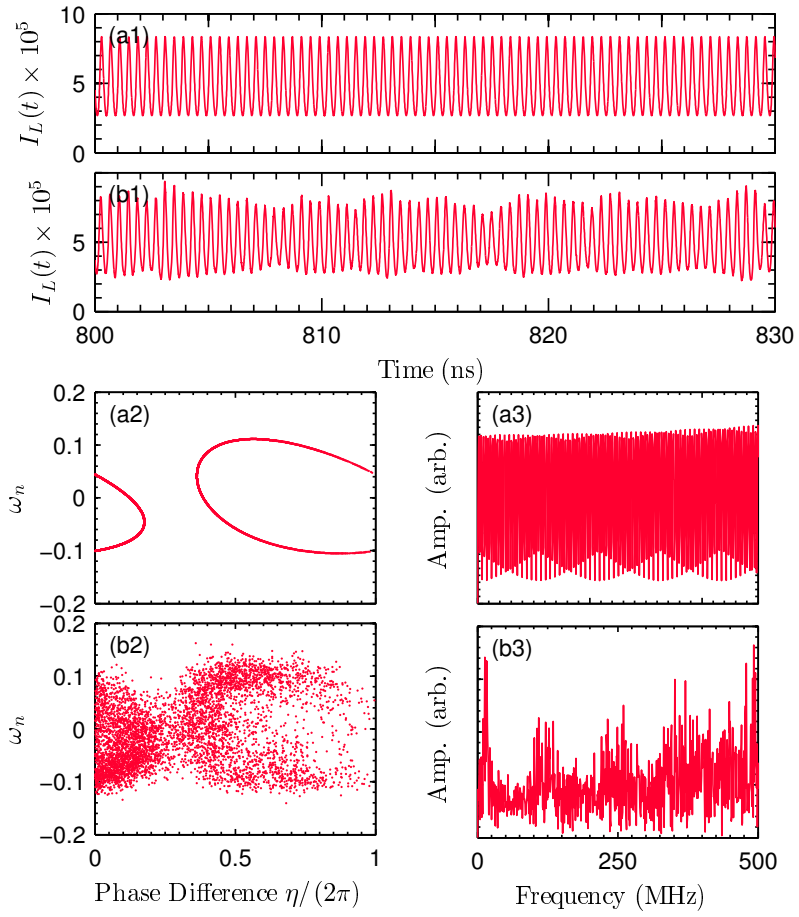

Figure 4.11. (1) Intensity time series $I_L(t)$, (2) phase portraits (ω_n, η), and (3) rf spectrum in the absence of noise (a) and in the presence of noise (b) for a bandwidth of $\Lambda_1 = 50$ MHz and detuning $\Delta_1 = -50$ MHz.

a bandwidth of $\Lambda_1 = 25$ MHz the dynamics become periodic and the period of these dynamics depend on the filter bandwidth, thus no longer considered optical injection. In summary, both the narrow-intermediate and intermediate-intermediate cases show that particular attractors no longer survive and, in turn, drive the system toward periodic oscillations determined by the a FOF time scales (τ and Λ). This relationship, however, is for two particular feedback rates κ_1 and κ_2. A complete picture becomes highly complex due to the amount of parameters $\Lambda_{1,2}, \tau_{1,2}, \Delta_{1,2}, \kappa_{1,2}$ which influence the dynamical behavior of this system.

4.4.2 Feedback from an intermediate and wide filter

We next investigate the effects of a competition between an intermediate filter and wide filter. The dynamics of both cases have been intensely studied for the single FOF case which showed that the stability and dynamics vary depending on the filter width [44]. Knowing that the wide filter resembles COF, we expect to see only two time signatures (τ and $1/f_{RO}$), instead of the influence of the bandwidth Λ found in FOF dynamics.

To study this system, we fix both bandwidths at $\Lambda_1 = 20$ GHz and $\Lambda_2 = 1$ GHz and detunings $\Delta_1 = -5$ GHz and $\Delta_2 = -1.5$ GHz. κ_1 is varied while $\kappa_2 = 0.8$ GHz is fixed. κ_1 is varied, rather than Λ_1, because the period of elicited oscillations for this two FOF system remain unaltered when Λ_1 is increased. Fig. 4.12 contains the spectra of the intensity of the laser $I_L(t)$ and the intensity of the light through filter 2, $I_{F_2}(t)$, when the feedback rate κ_1 is varied. These two intensities were chosen because the light through filter 1, I_{F_1}, directly mimics $I_L(t)$ due to the wide filter and the presence of the ROs, which are not as dominant in the dynamics of feedback from filter 2.

Initially, the feedback is solely from cavity 2 ($\kappa_1 = 0$ GHz). Therefore, the dynamics which arise are a consequence of the spectrally filtered (intermediate) feedback from cavity 2, which are shown in Fig. 4.13 for feedback rates of $\kappa_2 = 0.8$ GHz and

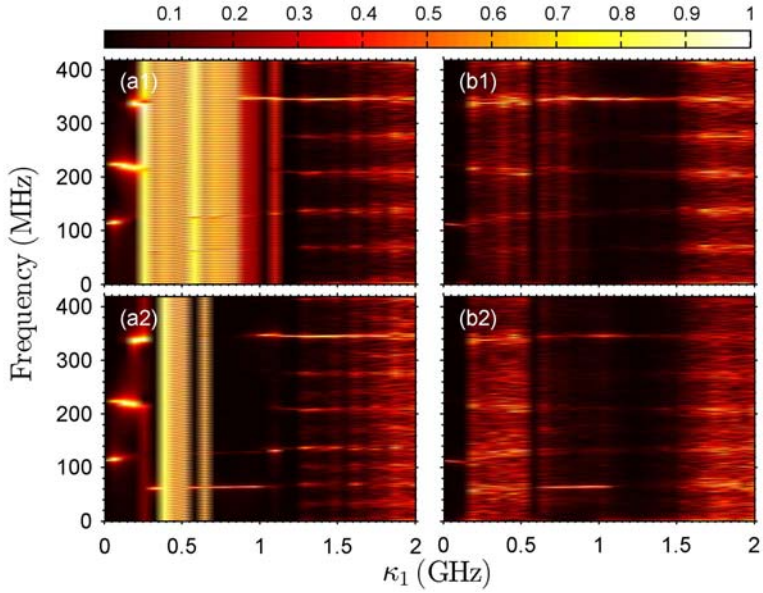

Figure 4.12. Deterministic (a) and stochastic (b) density plots of the amplitude of the spectrum as a function of the increasing feedback rate, κ_1. The spectra are calculated with the with the parameters mentioned in Table 5.1 except the following: $\Lambda_1 = 20$ GHz and $\Delta_1 = -5$ GHz. (1) Spectra of the intensity of light from laser, $I_L(t)$ and (2) spectra from the light through filter 2, $I_{F_2}(t)$.

$\kappa_1 = 0$ GHz. It is clear that the rf spectra of the deterministic (a3) and stochastic (b3) dynamics are very similar at this feedback strengths. The dominant frequency $f_2 \approx 112$ MHz corresponds to the fundamental frequency of cavity 2. The higher harmonics are also present with decreasing amplitudes. The feedback rate κ_1 is increased which enhances the second and third harmonic shown in both Fig. 4.12(a1) and (a2). As the feedback rate increases, $\kappa_1 \approx 0.32$ GHz, a frequency at $f \approx 66$ MHz emerges. We note that this corresponds to the fundamental frequency from cavity 1 which is $f_1 \approx 1/\tau_1$, which has no signatures of the bandwidth ($\Lambda_1 = 20$ GHz). A continued increase in κ_1 results in the enhancement of the successive higher harmonics, the second and third harmonic emerge, $2f_1$ and $3f_1$ respectively. The ROs appear in the laser intensity, which is shown Fig.4.12(a1), while they are attenuated through filter 2 shown in Fig. 4.12(a2).

The dynamics become more complicated and eventually evolve into the chaotic regime as the feedback rate κ_1 is increased. This is seen in all three subplots in Fig. 4.13(c1) and Fig 4.13(d1) at feedback rate of $\kappa_1 = 1.7$ GHz. The complicated time series, the jumping between attractors in the phase portrait and the spread in the rf spectrum all indicate the emergence of a chaotic regime. This behavior is well known for COF systems as the feedback rate is increased eventually inducing coherence collapse.

Comparing the deterministic [Fig. 4.12(a)] and stochastic [Fig. 4.12(b)] spectra (density plots) for an increasing feedback strength (κ_1), it is evident that noise plays a significant role in determining which frequencies emerge. This is understood by noting that the filter widths are larger, thus effectively reducing the spectral filtering of the feedback fields. Initially, the frequency spectra are very similar when $\kappa_1 = 0$ GHz shown in Fig.4.13(a3) and Fig. 4.13(b3). As κ_1 is increased, two regions of dissimilarity emerge. The first is a lack of the second and third harmonic found in Fig. 4.12(b). Upon further investigation we found that these harmonics emerge as the system evolves toward a steady state intensity. When the feedback rate is 0.1 GHz

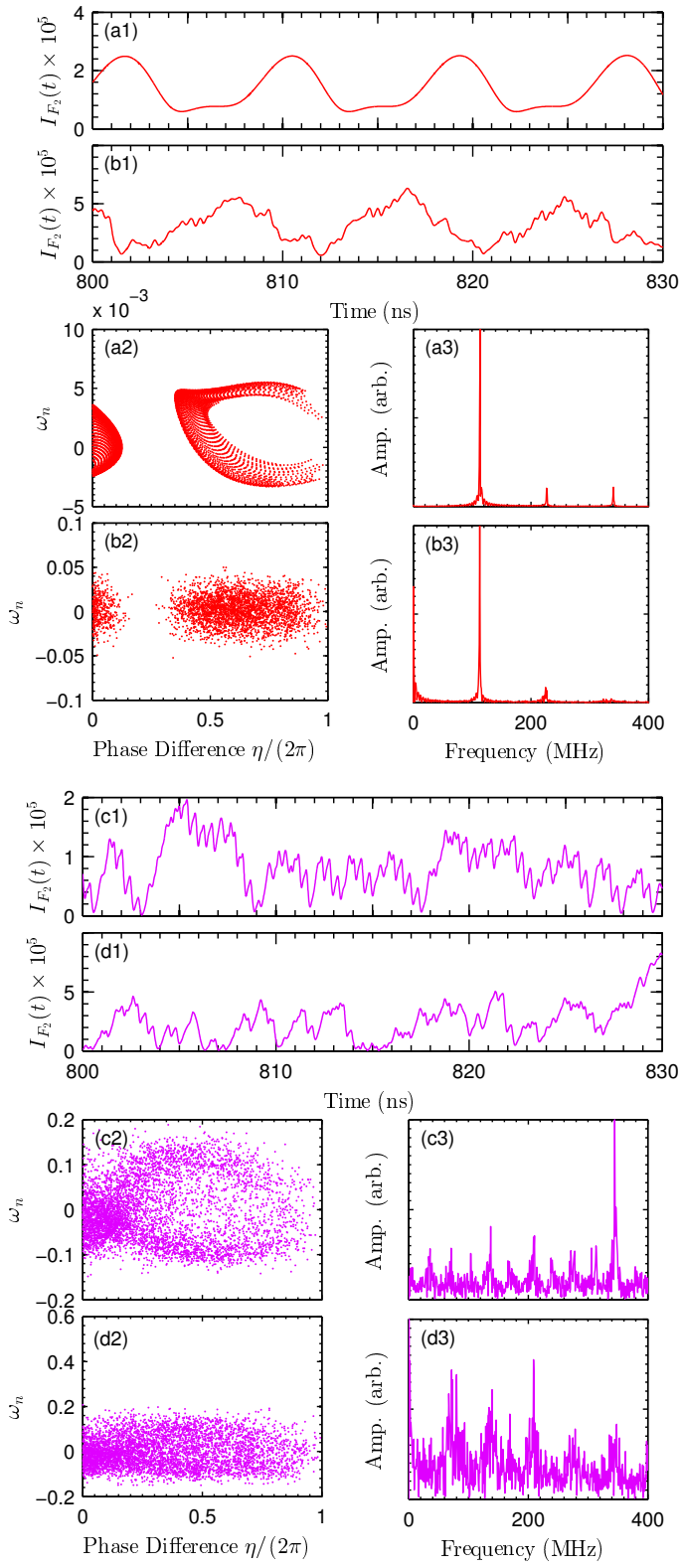

Figure 4.13. Three subplots are produced using the intensity of light through filter 2, $I_{F_2}(t)$. The times series (1), phase portrait $\omega_n, \eta(t)$ (2), and rf spectrum (3) are calculated for the feedback rates [(a) and (b)] $\kappa_1 = 0$ GHz and [(c) and (d)] $\kappa_1 = 1.7$ GHz.

$< \kappa_1 < 0.3$ GHz, noise drives the system out of these fixed point solutions, which is in good agreement with the previous analysis.

However, it is interesting to note that noise does not appear to delay the onset of chaos in larger feedback regimes ($\kappa_1 > 1.5$ GHz) shown in Fig. 4.12(b). A stark difference between the former bandwidth regimes and the wide-intermediate regime is that there is no averaging between the fundamental frequencies of the cavities, i.e. the dynamics are dictated by cavity 2 (intermediate filter) or cavity 1 (wide filter). In the presence of noise, two chaotic regimes emerge, when 0.3 GHz $< \kappa_1 <$ 0.55 GHz and $\kappa_1 > 1.7$ GHz [Fig. 4.12(b)]. For small feedback strengths (0.3 GHz $< \kappa_1 <$ 0.55 GHz) when the RO dynamics emerge [Fig. 4.12(a)], instead of driving the system toward periodic oscillations, the dynamics become chaotic [Fig. 4.12(b)]. In summary, the presence of a large bandwidth does not filter the frequency content and thus permits chaotic dynamics when the deterministic periodic (ROs) attractors no longer survive in the presence of noise even for a smaller feedback rate (0.3 GHz $< \kappa_1 <$ 0.55 GHz).

4.5 Discussion and conclusion

In this paper, we have reported on a theoretical and computational investigation of the effects of quantum noise on the complex dynamics that arise in the instantaneous optical frequency of a SCL that is subject to two filtered optical feedbacks. A majority of the results deal with the situation where the bandwidths of both filters through which the feedbacks are filtered are in the intermediate regime and wherein the feedback strength from one cavity is kept fixed while the feedback strength from the second cavity is varied. For these parameters, the most important observation is that the feedback strength needed from the second cavity to produce coherence collapse is significantly increased in the presence of noise. Our calculations indicate that this is a general feature of two FOFs in the presence of noise, even though we have displayed the results for one set of parameters. The physical origin of this increased feedback needed to produce coherence collapse lies in the fact that some of the

attractors in the deterministic model do not survive in the presence of noise. An important consequence of this is that the effects of the time-delay and filter bandwidth are enhanced in the presence of quantum noise.

Most of the results that we report show the dynamics up to frequencies of a few hundred MHz since these can be easily measured with standard detection components with rise times of a few nanoseconds. In some representative cases we also show the observed behaviors extended out to a few GHz, and the dominant theme to emerge from these data is that as the feedback strength from the second cavity is increased, the relaxation oscillations become the more dominant feature. In general, the results indicate that the effect of noise is to destroy the periodic attractor related to the relaxation oscillations and to enhance the effects of time-delay and filter bandwidth.

Typically, the effects of quantum noise will be most prominent when both filters have bandwidths in the intermediate regime. For narrow filters, any relaxation oscillations that are undamped will be suppressed by the narrow filters and hence the dynamics will be dominated by the time-delay of the feedbacks. For wide filters, signatures of the time-delayed feedback will be suppressed by the relaxation oscillations. It is only the intermediate regime in which noise can push the dynamics either towards making the time-delay dynamics the dominant ones or the relaxation oscillations the dominant ones, depending on feedback strengths.

This chapter also reports the laser frequency dynamics when one of the filters has an intermediate bandwidth and the other is either much narrower or much wider. In the former case, the effect of quantum noise is to once again drive the system away from the deterministic fixed point. In addition, the relaxation oscillations are suppressed and the time scale associated with the time-delayed feedback and the filter bandwidth contribute to the dominant frequencies. In the case of one intermediate filter and one wide filter, the spectral filtering of the feedback is reduced and as a consequence one finds that the laser frequency goes into the coherence collapse regime at about the same feedback levels in the presence of quantum noise as it does in the deterministic case. Therefore, it is clear that the requirement for a higher feedback

strength to induce coherence collapse in the presence of quantum noise arises only when the filter bandwidths are in the intermediate regime, even though noise does play a role in determining which deterministic attractors persist.

In summary, our work confirms that it is important to include the role of quantum noise to accurately describe the frequency dynamics of a SCL subject to two FOFs. The complexity and richness of this multi-parameter system raises some interesting and important questions, such as the physical mechanisms that cause laser frequency dynamics to be dominated by the time-delay and filter bandwidth in the two intermediate filter case, the reasons for the return maps to deviate from a linear shape in the presence of noise, the effects of correlated amplitude and inversion noise, and the influence of different noise strengths and of other combinations of filter widths. We hope to explore these, and other, questions in future studies.

5. Parity-Time Symmetry Breaking in Delay Coupled SCLs

The two previous chapters discussed our investigations on the dynamics that arise in a SCL due to two filtered optical feedbacks. In this chapter, we shift our focus to a system comprising two optically coupled SCLs. Although the theoretical model remains very similar, we now examine the optically induced dynamics of the SCLs in a new context, parity (P) and time-reversal (T) symmetry breaking. Therefore, it is important to understand the background of PT-symmetry and the connection to optically coupled SCLs.

5.1 Introduction

Carl Bender and Stefan Boettcher demonstrated that non-Hermitian Hamiltonians, invariant under the combined operations of P and T, may have a set of entirely real eigenvalues [69]. In particular, the eigenvalues can undergo a transition from purely real to complex upon changing a parameter that controls the non-Hermiticity of the Hamiltonian. These surprising results sparked a theoretical interest in PT-symmetric systems. The implications of a non-Hermitian Hamiltonian on our understanding of quantum theory continue to be debated and studied in mathematical physics [70–74]. However, considerable interest in PT-symmetric systems has gained traction since the proposal and subsequent experimental realizations of PT-transitions in optical materials. In particular, a flurry of experimental studies are showing that the field of optics offers a rich test-bed to explore the notions of PT-transitions [75–81]. By advantage of the ability to steer the system into a region of interest, i.e. in a region where the symmetry is broken or unbroken, these investigations are paving the way toward applications in laser physics [82–84] and synthetic optical isolators [85] (see references therein). Let us now take a closer look at what is meant by PT-transition.

The studies assume the conventional definitions of P and T that respectively have the effect of changing a right-handed system to a left-handed system ($x \to -x, y \to -y, z \to -z$) and reversing time, or motion ($t \to -t$) [86]. We remark that the effect of T is of particular interest to us, since the system we investigate has an intrinsic time-delay associated with the optically coupled fields. A time-delay is present because of the finite distance L between the two SCLs, i.e. the light 'seen' by SCL1 was emitted by SCL2 at an earlier time τ ($\tau = L/c$). Indeed, we shall see that the notion of reversing time produces surprising effects on the PT-transition. However, to anticipate these effects, we now return to the introduction of a PT-transition.

When a Hamiltonian is invariant under a combination of P and T, the Hamiltonian commutes with the PT operator, i.e. $[H, PT] = 0$, and is said to be PT-symmetric. PT-symmetry breaking occurs when the eigenvalues transition from purely real (termed below threshold) to complex (termed above threshold). The transition marks the symmetry breaking of the eigensolutions. More precisely, the eigensolutions below threshold commute with the PT operator, while the eigensolutions above threshold no longer commute.

To gain an intuition for the features of PT-symmetry breaking, it is illustrative to examine a two-state system, where the 'Hamiltonian' can be represented by a 2x2 matrix. Besides being a paradigm for experimental studies in PT-symmetry, we will show in subsequent sections that a 2x2 PT-model can accurately describe our experimental system of two optically coupled SCLs. A general 'Hamiltonian' for this system can be expressed by

$$H = \begin{pmatrix} a & b \\ c & d \end{pmatrix}, \tag{5.1}$$

where a, b, c, and d can be complex. In a two-state system, the form of P and T can be expressed by P $= \left(\begin{smallmatrix} 0 & 1 \\ 1 & 0 \end{smallmatrix}\right)$ and T $\implies i \to -i$. Using these definitions, one can show that for H to remain invariant under the combined operations of P and T ($[\mathcal{PT}, H] = 0$), the following restrictions must be met,

$$a = d^* \text{ and } b = c^*. \tag{5.2}$$

The meaning of terms (a, b, c, and, d) become clear as we examine the Schrödinger equation of two state system written in matrix form,

$$-i\hbar \begin{pmatrix} \dot{\psi}_1(t) \\ \dot{\psi}_2(t) \end{pmatrix} = \begin{pmatrix} a & b \\ c & d \end{pmatrix} \begin{pmatrix} \psi_1(t) \\ \psi_2(t) \end{pmatrix}. \tag{5.3}$$

We see that b and c couple the two states, $\psi_1(t)$ and $\psi_2(t)$. The role of a and d are a little more complex. Let us suppose the states are uncoupled ($b = c = 0$). We can then write the form of the solution to Eqn. (5.5) as e^{-idt}, where we can replace with d with a. Thus, the imaginary part of d ($Im(d)$) determines the exponential growth or decay, and the real part of d ($Re(d)$) is the intrinsic resonant frequency of each state. If we examine the simplest case, which is also the prototype for PT-symmetric systems, then H is expressed by

$$H = \begin{pmatrix} -i\gamma & \kappa \\ \kappa & i\gamma \end{pmatrix}, \tag{5.4}$$

where the real parameters κ and γ represent the coupling strength between the two states and the intrinsic gain/loss strength of each state, respectively. We have renamed the parameters in order to touch base with the conventional notation used in PT optical systems. Up to this point we have not specified the system that H describes. It is beneficial to examine a prototypical example in optics, not only for illustrative purposes and to gain insight into the PT-characteristics, but also to contrast our PT-model describing time-delayed optically coupled SCLs. In this way, the distinctive and novel features of coupled SCLs clearly emerge.

We turn now to the prototype comprising two optically coupled waveguides that have been engineered to facilitate a balanced gain and loss in each channel. Light propagating in each channel is evanescently coupled to the neighboring waveguide. Hence the coupling term κ is tuned via the spacing between each waveguide. Each channel has an intrinsic loss, however one arm is optically pumped to provide a variable gain. An impressive feature of this system is that the optical field dynamics are described by Eqn. (5.5), a 2x2 'Hamiltonian',

$$-i\hbar \begin{pmatrix} \dot{\psi}_1(t) \\ \dot{\psi}_2(t) \end{pmatrix} = \begin{pmatrix} -i\gamma & \kappa \\ \kappa & i\gamma \end{pmatrix} \begin{pmatrix} \psi_1(t) \\ \psi_2(t) \end{pmatrix}, \tag{5.5}$$

where ψ_1 and ψ_2 represent the electric field envelopes in each channel. Knowing the rate equations that govern the field dynamics, let us take a closer look at the implications of PT-symmetry breaking and how one can experimentally observe the transition.

It is straightforward to show that the eigenvalues of Eqn. (5.5) are $\lambda_{1,2} = \pm\sqrt{\kappa^2 - \gamma^2}$. By examining the eigenvalues along with the form of the solution ($e^{-i\lambda t}$), one can anticipate the behavior indicated by a PT-transition. Below threshold ($\kappa > \gamma$), the amplitudes undergo oscillations and above threshold ($\kappa < \gamma$) the amplitudes exponentially grow or decay. This is the behavior Ref. [75] observed using balanced dual gain/loss waveguides. In the next section, we will discuss the similarities and differences between a conventional PT-system (coupled waveguides) and optically coupled SCLs - comparing both the model and experimental observations.

To understand how these distinctions emerge, we introduce the full model comprising four coupled nonlinear rate equations that describe the electric field and carrier number inversion of each SCL. We show the remarkable feature that the rate equations reduce to a time-delayed 2x2 PT-model. The time-delayed PT-model is analyzed in detail by examining the evolution of the eigenvalues as the PT parameters are varied. We take a closer look at some key differences between the conventional PT-model of coupled waveguides and the PT-model of optically coupled SCLs. The first and most surprising is the effect of the time-delay on the PT-transition. We discuss the counterintuitive notion of time reversal on delayed fields, and show that the frequency detuning between the SCLs replaces the role of gain/loss in PT-optics.

After the analysis of the PT-model, we show the excellent agreement with the simulations produced by the full rate equations. The experimental procedure is outlined, and we analyze the experimental observations by comparing them with the 2x2 PT-model and the simulations. The time-delay is varied in order to demonstrate the

unique features that arise it. Finally, we discuss the connection between the phase breaking/locking condition, typical of coupled oscillators, and the PT-transition that occurs in coupled SCLs.

5.2 Rate Equations

The numerical simulations are done with the full rate equation model and time averaged over 1ns to mimic the detector response time in experiments. The model we employ assumes the SCLs are identical, except for their free running emission frequencies (at threshold), and operate at nearly identical optical frequencies ($\omega_1 \approx \omega_2$) [87]. The slowly varying electric fields are defined in a symmetric reference frame $\theta = (\omega_1 + \omega_2)/2$. The rate equations describing the normalized complex electric fields $E_{1,2}$ and the normalized excess carrier densities $N_{1,2}$ may be written as follows:

$$\frac{dE_1}{dt} = (1 + i\alpha)N_1(t)E_1(t) + i\Delta\omega E_1(t) + \kappa e^{-i\theta\tau}E_2(t-\tau), \tag{5.6a}$$

$$\frac{dE_2}{dt} = (1 + i\alpha)N_2(t)E_2(t) - i\Delta\omega E_2(t) + \kappa e^{-i\theta\tau}E_1(t-\tau), \tag{5.6b}$$

$$T\frac{dN_1}{dt} = J_1 - N_1(t) - (1 + 2N_1(t))|E_1(t)|^2, \tag{5.6c}$$

$$T\frac{dN_2}{dt} = J_2 - N_2(t) - (1 + 2N_2(t))|E_2(t)|^2, \tag{5.6d}$$

where α is the linewidth enhancement factor, τ is the time delay in the coupling, $J_{1,2} \propto I_{1,2}/I_{thr}$ is the pumping current above threshold, and $T = \tau_s/\tau_p$ is the ratio of the carrier lifetime τ_s to photon lifetime τ_p. The two PT parameters, κ and $\Delta\omega = (\omega_1 - \omega_2)/2$, are the coupling strength coefficient and frequency detuning, respectively. These are examined in more detail when we outline the experimental procedure. In this way, it will become clear how we experimentally determine their numerical values for the PT-model and simulations. The remaining normalized variables are described in Chapter 2.

The derivation of Eqns. (5.6) follows a similar approach to the rate equations describing optical feedback that were outlined in Chapter 2. In Eqn.(5.6a) and (5.6b), the optical feedback term is modified to account for the mutual coupling between two

SCLs. The second term (in Eqn.(5.6a) and (5.6b)) induces a phase shift that depends linearly on the frequency detuning, $\Delta\omega$. There is linear dependence because the higher-order coupling terms have been neglected. These approximations were shown to be accurate for weak coupling strengths, typically less than 5% of optical power coupled between SCLs [87]. The experimental conditions we employ fall within this range. Eqns. (5.6) are known to accurately mimic a broad range of dynamical behavior of coupled SCLs [88–91].

The parameter values used in the simulations are defined in Table 5.1. The stated values correspond to those typical of the SCL used in our experiment [92]. We refer to Eqns. (5.6) as the full-model in order to distinguish them from the simplified PT-model introduced in the next section.

Table 5.1.
The parameter values for a typical SCL that are used in the simulations (unless otherwise specified).

Quantity	Symbol	Value
Linewidth enhancement factor	α	5
Coupling strength	κ	0 - 0.2
Delay-time	τ	0 - 500
Ratio of carrier to photon lifetime	T	100
Pump rate	J	0.01 - 0.10

We integrate Eqns. (5.6) using a modified fourth order Runge-Kutta method with a step size that varies from 0.1ps to 10ps. The delay is accounted for by storing the history at each step over a 4τ interval in order to calculate an interpolated history function.

We emphasize that the gain and loss ($\pm i\gamma$) in conventional PT systems is now replaced by the $\pm i\Delta\omega$ term. The detuning term ($\pm\Delta\omega$) accounts for frequency pulling that is typical of coupled laser oscillators operating at different frequencies [93]. This

can be understood by examining Eqns. (5.6a) and (5.6b), wherein a phase shift in the fields $E_{1,2}$ is induced by the second term $\pm i\Delta\omega E_{1,2}(t)$ in Eqns. (5.6a) and (5.6b). We examine this in more detail in the following section.

5.3 Theoretical Results

To motivate the 2x2 PT-model, we begin with the simplest case. We arrive at this case by using appropriate approximations of the relevant parameters, τ, $N_{1,2}$, and $\theta\tau$. The restrictions on these parameters are gradually removed as we bring the PT-model closer to the experimental and simulated parameter values. To show the excellent agreement between the 2x2 model and simulations, we compare the predicted dynamics for three cases:

5.3.1 $\tau = 0$

We first consider the case of zero delay ($\tau = 0$). Let us suppose that the SCLs are uncoupled ($\kappa = 0$). The first term in Eqn. (5.6a) and (5.6b) accounts for the total growth or decay of the fields $E_{1,2}$ depending on the sign ($\pm$) of $N_{1,2}$. When the SCLs are operating in a steady-state, we expect the inversion above transparency to be zero, $N_{1,2} = 0$. We make the approximation for small κ that $N_{1,2} \approx 0$. The validity of this approximation is discussed in Section 5.8. Using these approximations, we write the time evolution of the electric fields in matrix notation as follows,

$$\begin{pmatrix} \dot{E}_1(t) \\ \dot{E}_2(t) \end{pmatrix} = \begin{pmatrix} i\Delta\omega & \kappa \\ \kappa & -i\Delta\omega \end{pmatrix} \begin{pmatrix} E_1(t) \\ E_2(t) \end{pmatrix}. \tag{5.7}$$

Contrasting this with Eqn. (5.5), we find two important differences.

First, the SCL model (Eqn. (5.7)) is missing an i from the LHS of the coupled waveguide model (Eqn. (5.5)). The absence of i corresponds to a 90° rotation in the complex plane, also called a Wick-rotation [94]. The absence of i also changes how each term in the 'Hamiltonian' in Eqn. (5.7) affects the dynamics. For example, the

diagonal terms no longer contribute to a growth or decay. Rather, $\pm i\Delta\omega$ determines the frequency of oscillations when there is no coupling ($\kappa = 0$).

Second, the coupling term, κ, no longer determines the frequency of exchange between channels (or SCLs). To understand this, let us suppose the diagonal elements are zero ($\Delta\omega = 0$). In the coupled waveguide experiment, κ is the frequency at which the channels exchange intensities (or energy), and the intensities are π out of phase. Contrast this with the optically coupled SCLs, we find that κ contributes to a growth in the intensities of the SCLs. Physically this can be understood in the following way: a fraction of the emitted light from each SCL is injected into the neighboring SCL, and the additional photons in the laser cavity contribute to the growth of the cavity field. Given these differences we ask the question of whether coupled SCLs still retain signatures of a PT-transition.

One can determine the eigenvalues by solving the following determinant,

$$\det\left[\begin{pmatrix} i\Delta\omega & \kappa \\ \kappa & -i\Delta\omega \end{pmatrix} - \mathbb{1}\lambda\right] = 0, \tag{5.8}$$

which yields the result $\lambda_{1,2} = \pm\sqrt{\kappa^2 - \Delta\omega^2}$. PT-symmetry breaking is indicated by a transition of the eigenvalues from purely real to complex. To observe this transition, we record the eigenvalues as we sweep $\Delta\omega$, while keeping κ fixed. The evolution of the eigenvalues is depicted in Fig. 5.1(a), where the coupling strength is a constant value of $\kappa = 0.1$ and the frequency mismatch is scanned from $\Delta\omega = -0.2 \rightarrow 0.2$. Thus we expect a PT-transition when $\kappa = |\Delta\omega|$. The effect of this transition on the lasers intensities is seen by noting the form ($\mathrm{e}^{\lambda t}$) of the solution to Eqn. (5.5). When $|\Delta\omega| > \kappa$, the eigenvalues are purely imaginary which indicates that the intensity of the laser undergoes oscillations. Below threshold, $|\Delta\omega| < \kappa$, the eigenvalues are real, and a growth or decay is expected. This behavior is similar to transitions reported, and outlined in the Introduction, in PT-symmetric waveguides [75].

To demonstrate that the PT-model provides an accurate description of the global behavior of the coupled SCLs, we compare the eigenvalue picture to the simulations provided by the full rate equation model (Eqns.(5.6)). We now allow the carrier

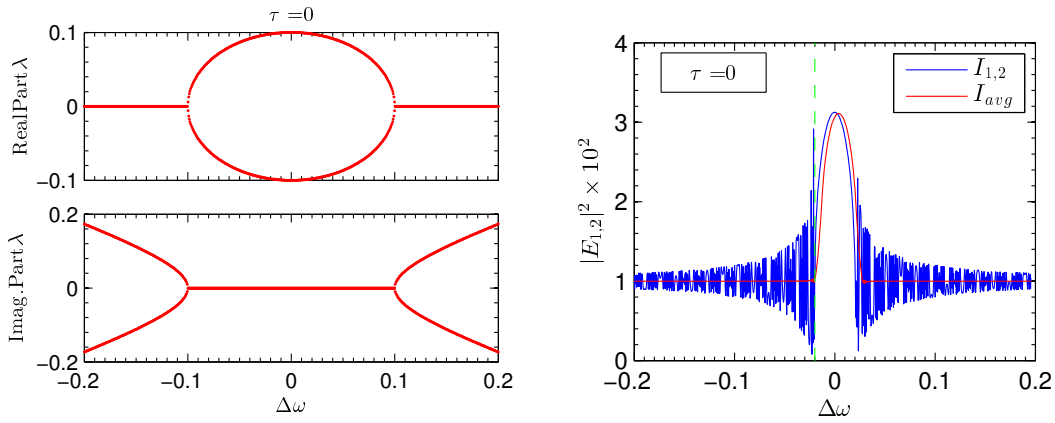

(a) (b)

Figure 5.1. (a) Trajectories of the eigenvalues when $\kappa = 0.1$ for zero delay ($\tau = 0$). (b) Simulations of the SCL intensities (I_1 and I_2) when $\kappa = 0.02$ and $P_1 = P_2 = 0.01$ for zero delay ($\tau = 0$). The solid blue line represents the instantaneous intensities of SCL1 and SCL2 (same). The solid red line is a rolling time average over 10 ns of the instantaneous intensities.

inversion ($N_{1,2}(t)$) to temporally change. When the system is below PT-threshold ($\kappa > |\Delta\omega|$), we no longer expect the approximation, $N_{1,2} \approx 0$, to be accurate. The eigenvalues below PT-threshold ($\kappa > |\Delta\omega|$) suggest an intensity growth (or decay). This addition (or depletion) of photons from the steady-state will have an effect on the carrier inversion ($N_{1,2}$). To accurately describe the coupling between the inversion and field below threshold, we rely on the rate Eqns. 4.1, which are integrated using a similar method to that provided in Chapter 2. The same procedure (scanning $\Delta\omega$) is followed which produced the eigenvalue plot shown in Fig. 5.1(a).

It is important to point out the difference between the two lines in Fig. 5.1(b). The red line represents a rolling time-average of the two intensities ($I_{1,2}(t)$), which in this case are identical due to the symmetry of the system. We emphasize that the remaining profiles are time-averaged as well. This is done in order to connect the simulations to the experimental procedure, wherein the bandwidth of the photo-diodes (10 MHz) and the sampling rate of the oscilloscope produce the effect of

a time-average. In addition, this allows us to examine the global behavior of the intensity evolution.

When examining Fig. 5.1(b) it is clear that the simulations agree well with PT-model depicted by the evolution of the eigenvalues in Fig. 5.1(a). At large negative detunings ($-\Delta\omega$), the intensities undergo oscillations with a frequency that is dependent on $\sqrt{\kappa^2 - \Delta\omega^2}$. When $\kappa > |\Delta\omega|$, the oscillations cease, and the amplitudes grow. The full-rate equations show that the inversion compensates and the intensity decreases until the point $\kappa < \Delta\omega$, where oscillations once more begin. The frequency of these oscillations are captured in Fig. 5.2, which is a spectrogram of intensity profile. To accentuate the transition, the coupling strength was set to $\kappa = 0.1$ and the detuning $\Delta\omega$ was scanned. A rolling fft was calculated from similar instantaneous (blue) intensity oscillations shown in Fig. 5.1(b). The amplitude of the spectra correspond to the color scheme in Fig. 5.2. The frequency of the oscillations follows a

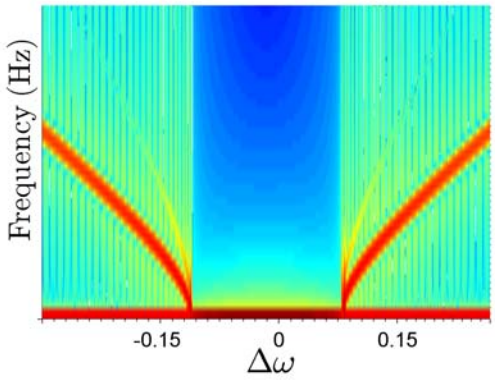

Figure 5.2. Spectrogram of instantaneous intensity oscillations taken from the $\tau = 0$ case in which $\kappa = 0.1$.

trajectory which agrees with the expected form of $\sqrt{\kappa^2 - \Delta\omega^2}$.

5.3.2 $\tau = 100$ and $\theta\tau = 2\pi m$

Next, we include the effects of a non-zero delay ($\tau > 0$). The delay is set to $\tau = 100$. Now that the delay is nonzero, we can no longer ignore the phase accumulation, $e^{-i\theta\tau}$, found in the third term of Eqns. (5.6a) and (5.6b). The SCLs are arranged so that the phase accumulation is $e^{-i\theta\tau} = 1$. This is achieved by changing the cavity length and average frequency of the two SCLs to ensure that $\theta\tau = 2\pi m$.

In the presence of a delay field $E_{1,2}(t-\tau)$, Eqns. (5.6a) and (5.6b) take the form of delay differential equations (DDEs). Methods for solving delay differential equations are similar to those proposed for ODEs in which one seeks exponential solutions of the form $e^{\lambda t}$ [95]. Using this form, we express the delayed terms in Eqn. (5.6) as $E_{1,2}(t-\tau) \propto E(t)e^{-\lambda\tau}$. Examining Eqns. (5.6a) and (5.6b), the coupling term now becomes $\kappa e^{-i\theta\tau}e^{-\lambda\tau}E(t) = \kappa e^{-\lambda\tau}E(t)$. Thus, an eigenvalue-like problem can be expressed as

$$\det\left[\begin{pmatrix} i\Delta\omega & \kappa \mathrm{e}^{-\lambda\tau} \\ \kappa \mathrm{e}^{-\lambda\tau} & -i\Delta\omega \end{pmatrix} - \mathbb{1}\lambda\right] = 0. \tag{5.9}$$

As expected, the effects of the delay appear in the off-diagonal term, or coupling strength. Furthermore, it is clear that *if* the eigenvalues are complex then the "operator" might no longer be PT-symmetric. Hence, we take a closer look at whether the system still retains PT-characteristics with a finite delay. The movement of eigenvalues, shown in Fig. (5.3(a)), is comparatively more complex.

The eigenvalues still retain the PT-characteristics, namely there is a distinct transition near $\kappa = |\Delta\omega|$, where the imaginary component of the eigenvalue (λ_I) becomes zero and the real part (λ_R) continues to grow until $\Delta\omega = 0$. The interesting behavior occurs above threshold when $|\Delta\omega| > \kappa$. λ_R oscillates from positive to negative, while λ_I follows a similar trajectory compared to the zero delay case (Fig. 5.1(a)) except for a series of discrete steps. A similar staircase pattern has been experimentally observed by measuring the frequency deviation between two coupled SCLs [96]. In addition, Wuenshe et. al. reported that the intensities of the two lasers change continuously in their phase difference from zero to π which may give rise to the discontinuities [96].

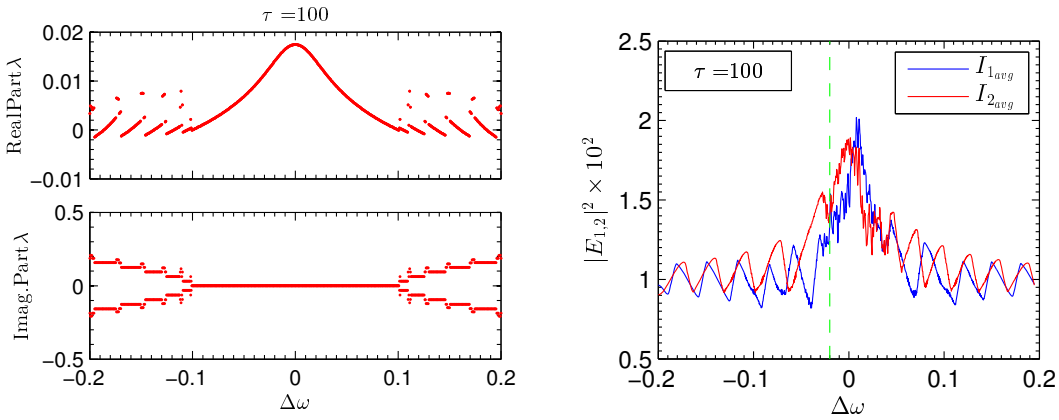

(a) (b)

Figure 5.3. (a) Trajectories of the eigenvalues when $\kappa = 0.1$ for finite delay of $\tau = 0$ and constant phase $\theta\tau = 2\pi n$. (b) Simulations of the SCL intensities (I_1 and I_2) for $\kappa = 0.02$, $P_1 = P_2 = 0.01$, and $\tau = 100$ with constant (πn) phase.

Remarkably, the λ_R oscillations are captured by the simulated time-averaged intensities ($I_{1,2_{avg}}$) shown in Fig. 5.3(b). Where the average intensities were constant for the zero delay case (Fig. 5.1(b)), oscillations are present in both intensities (SCL1 and SCL2) shown in Fig.5.3(b). The dashed green line, found in Fig. 5.3(b), marks the PT-transtion ($-\Delta\omega = \kappa = 0.02$) for the simulated parameters. Oscillations are induced above threshold $|\Delta\omega| > \kappa$. This behavior was suggested by the evolution of λ_R in the presence of a delay, shown in Fig 5.3(a), where λ_R undergoes transitions from positive to negative values.

By approaching this problem in the context of PT-symmetry breaking, we discover these unexpected oscillations of λ_R which to our knowledge have never been reported. However, in the PT-context two types of oscillatory dynamics arise. First, that non-zero λ_I values give rise to periodic oscillations whose frequency change with $\Delta\omega$. When $\Delta\omega$ and κ are constant, these oscillations can be observed in the intensity time-series. In comparison, the oscillations in λ_R, which we refer to as global oscillations, are observed when $\Delta\omega$ is *scanned* and the intensity profiles are recorded. Thus,

one could observe these global oscillations by scanning $\Delta\omega$ and time-averaging the intensity to filter out the faster oscillations caused by λ_I.

5.3.3 $\tau = 100$ and $\theta\tau$ varies

Finally, the effects of the phase accumulation are accounted for by allowing θ to vary. This case is the last step toward developing a time-delayed PT-model that mimics the experimental procedure. Indeed, we shall see that our experimental procedure for changing $\Delta\omega$, scanning the temperature to one laser, produces a change in θ. Recalling that $\theta = (\omega_1 + \omega_2)/2$, we achieve a θ variance by scanning one frequency (e.g. ω_1) and locking the other (e.g. ω_2). To induce a PT-transition, we repeat the same procedure as the previous two cases in which the coupling strength is set at $\kappa = 0.1$ and $\Delta\omega$ is scanned. The differences in the Hamiltonian between this case and the former two cases are the off-diagonal elements, shown in Eqn. (5.10), that contain an additional term, $e^{-i\theta\tau}$.

$$\det\left[\begin{pmatrix} i\Delta\omega & \kappa \mathrm{e}^{-\lambda\tau}\mathrm{e}^{-i\theta\tau} \\ \kappa \mathrm{e}^{-\lambda\tau}\mathrm{e}^{-i\theta\tau} & -i\Delta\omega \end{pmatrix} - \mathbb{1}\lambda\right] = 0. \tag{5.10}$$

It is worth noting that this term adds additional control over non-Hermicity of the 'Hamiltonian', i.e. by carefully manipulating either θ or τ one can vary $e^{-i\theta\tau}$ from real to purely imaginary. For the time being, we set this fact aside and will later return to this when we discuss proposal for future directions.

The evolution of the eigenvalues are depicted in Fig. 5.4(a), which follow a similar (albeit different) trajectory to the constant phase where $e^{-i\theta\tau} = 1$. Before we turn to their differences, we still find the oscillations of λ_R and the discrete steps formed by λ_I. A closer look, however, reveals that the frequency of the global (λ_R) oscillations have increased compared to Fig. 5.3(a). A second difference depicted in Fig. 5.3(a) is the juxtaposition between the discrete jumps formed by λ_R and the continuous 'curve' formed between $\Delta\omega = -0.2 \to -0.12$ and $\Delta\omega = 0.12 \to 0.2$. The 'curve' appears to lay over the discrete jumps. In addition, Fig. 5.4(a) shows an asymmetry about the

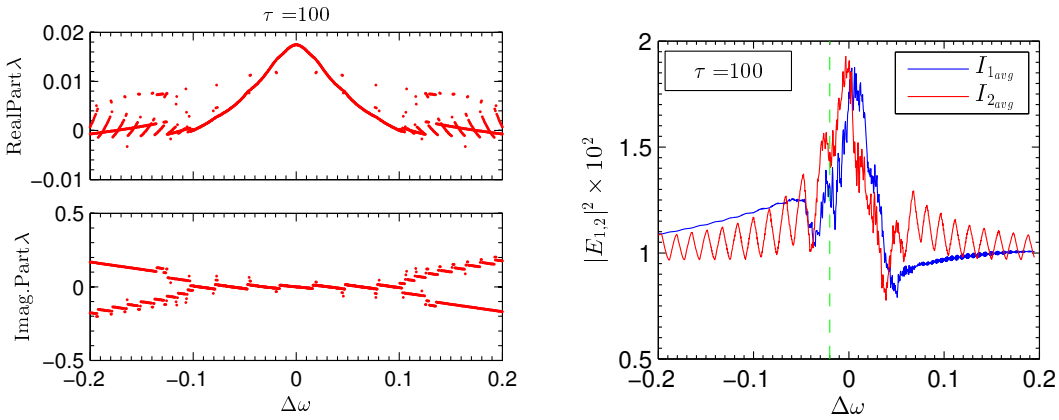

(a) (b)

Figure 5.4. (a) Trajectories of the eigenvalues when $\kappa = 0.1$ for finite delay of $\tau = 100$ and varying phase $\theta\tau$. (b) Simulations of the SCL intensities (I_1 and I_2) for $\kappa = 0.02$, $P_1 = P_2 = 0.01$, and $\tau = 100$ with varying phase $\theta\tau$.

$\lambda_I = 0$ axis. The asymmetry is introduced via the procedure of scanning only one laser. It is remarkable that both features, the increased frequency and continuous 'curve', are captured by the simulations shown in Fig. 5.4(b). Shown in the red solid line, the intensity of SCL2 ($I_{2_{avg}}$) undergoes global oscillations in the unbroken region ($|\Delta\omega| > \kappa$). In the same region, the average intensity of SCL1 ($I_{1_{avg}}$) exhibits a steady growth with no oscillations. The continuous 'curves', or evolution, of λ_R in Fig. 5.4(b) predict the behavior of I_1, while the discrete jumps of λ_R predict the behavior of I_2. Since the system is rendered infinitely dimensional due to the time-delay, writing an analytic solution is nearly impossible outside of steady-state regimes. Therefore, the simulations or bifurcation analysis is employed to gain insight into the dynamics. However, we point out the remarkable predictive ability of the PT-model given the complexity of the system.

This agrees well with the simplified PT-model which captures these characteristics. In the next section, we experimentally verify these PT-transitions, as well as the

effects of the time-delay on the global intensity. In particular, we explore the effects of different time-delays on the period of the global intensity oscillations.

Before discussing the experimental results, we outline the method for determining the eigenvalues. The zero delay ($\tau = 0$) case is straightforward, and we use these values for the initial "guess" when numerically solving the two finite delay cases. In both cases, Eqns. (5.9) and (5.10), the determinant is calculated and then separated into real and imaginary components from the ansatz $\lambda = \lambda_R + i\lambda_I$. Given the initial "guess", we solve the two coupled equations,

$$\Delta\omega^2 + \lambda_R^2 - \lambda_I^2 - \kappa^2 \mathrm{e}^{-2\lambda_R\tau} \cos\left(2\left(\lambda_I + \theta\right)\tau\right) = 0, \tag{5.11a}$$

$$2\lambda_R\lambda_I + \kappa^2 \mathrm{e}^{-2\lambda_R\tau} \sin\left(2\left(\lambda_I + \theta\right)\tau\right) = 0. \tag{5.11b}$$

If the delay is zero ($\tau = 0$), then the solutions are those determined by Eqn. (5.8). When examining Eqns. 5.11, it becomes clear that more than one solution may exist. We attempt to determine all the solutions by systematically varying the initial values. Finally, we discard all solutions except those that are associated with the largest positive and negative real eigenvalues, which ultimately determine the global behavior after a long temporal evolution. The dependence of the eigenvalues on the phase θ and time-delay τ are not straightforward. Therefore, we wait to discuss the effects of the phase and time-delay until the experimental results have been presented.

5.4 Experimental Design

Figure 5.5 is a schematic of the experimental configuration consisting of two single mode (HL7851G) semiconductor lasers (SCL1 and SCL2), an external cavity consisting of two beam-splitting mirrors (BS1 and BS2) which optically couples the two SCLs, and an external control of the coupling strength κ via the variable neutral density filter (VND). The SCLs are identical, except for their free-running optical frequencies and threshold pump currents. The transmission through the VND is determined by an independent laser (L3) and photodiode (PD3) which allows us to calibrate the experimental and theoretical coupling strength, $\kappa \equiv \left(1 - r^2\right) / \left(r\tau_{in}\right) \xi\tau_p$,

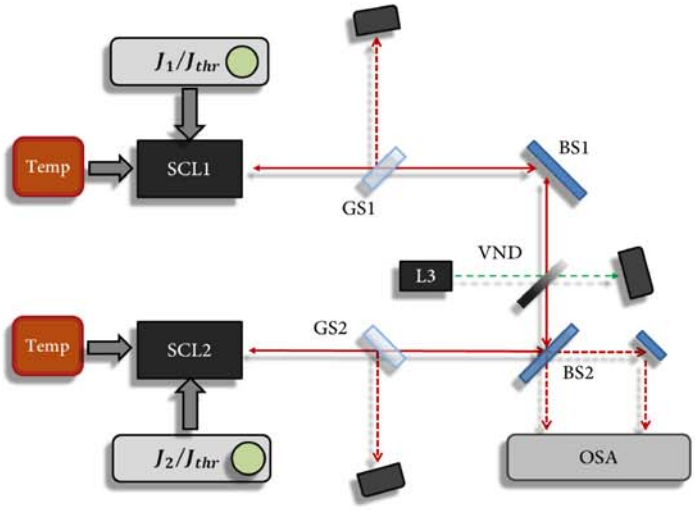

Figure 5.5. Experimental set-up. SCL: semiconductor laser, GS: glass slide, M: mirror, VND: variable neutral density filter (mounted on a translation stage), L3: laser used to quantify experimental coupling strength, PD: photodiodes, $P_{1,2}$: pump current controller

where r is the reflectivity of the external laser facet, ξ^2 is the fraction of optical power transmitted by all the optical elements, τ_{in} is the internal laser round-trip time, and τ_p is the photon lifetime. Once the transmission through the VND is recorded, ξ^2 can be determined since all the other optical elements are fixed. This model assumes that the fractional power is entirely coupled into the active region of the SCL. Due to comparative sizes of the beam profile ($> 100\,\mu$m) and the active region ($\approx 10\,\mu$m), only a portion of the power is coupled into the active region of the SCL.

Cheng et. at. showed that the measured fractional power (κ) needed to be scaled by a factor of 10^{-1} in order to accurately describe the dynamics [92]. Hence, the coupling strength (κ) used in the simulations is a semi-free parameter. This means that ξ^2 is experimentally determined, and then scaled up to a factor of 10^{-1} in order to match the simulations. Once the scaling factor is determined, we keep this fixed for all experimental trials in order to stay consistent. For the remaining parameters we use those found in Ref. [92]. The experiment is designed such that the coupling

strengths to the two lasers are equal, and a Farady-rotator (not shown) is placed in the coupling beam path to ensure that self coupling is eliminated. The glass slides (GS1 and GS2) independently reflect a portion (8%) of the intensity from SCL1 and SCL2, and the measurement of the laser intensities is performed using two 1 GHz photo-diodes (PD1 and PD2) in conjunction with a 1 GHz oscilloscope. The current and temperature of the lasers are stabilized to an accuracy of 0.01 mA and 0.01 C, respectively.

The two lasers are bidirectionally coupled to each other, and then the temperature to SCL1 is scanned at a slow rate ($<$ 10 Hz). The intensities of both lasers are continuously monitored with photodiodes. The important parameters, κ and $\Delta\omega$, can be varied experimentally via the VND and the temperature of SCL1, respectively.

It is important to point out that different behavior occurs if the coupling strength is unequal or in the extreme case of uni-direction coupling. If the two lasers are uncoupled, then the intensity of SCL2 remains a constant and the intensity of SCL1 decreases in proportion to the temperature increase. In case of unidirectional coupling, the intensity of the "slave" follows an intensity profile identical to those reported in injection studies [97, 98].

5.5 Experimental Procedure

In this section we discuss the experimental procedures used to vary the parameters $\Delta\omega$ and κ that induce a PT-transition.

5.5.1 Temperature Variation

We first begin by varying $\Delta\omega$. For our experimental laser diode near room temperature, the optical emission frequency is proportional to the temperature of active region. Since the experimental procedure requires that we change the temperature of the SCL by less than 4°C, it is safe to assume a linear dependence of the emission frequency on the temperature. Ideally, one could simultaneously control the tempera-

ture of both SCLs. This procedure would induce a frequency difference, and have the ability to keep the optical phase accumulation ($e^{-i\theta\tau}$) a constant. The temperature controllers (Thorlabs TEC2000) allow you to externally control the *set* temperature. However, this does not guarantee that the *actual* temperatures of the diodes follow the same trajectory. This trajectory depends on the PID controller as well as the mounting fixture of the diode.

The two mounts are not identical, and even with similar PID setting the two temperatures follow different trajectories. One may be able to resolve this issue by adjusting the PID controls such that they follow (almost) identical trajectories, or purchase/build two identical mounts. As of now, only one SCL is adjusted. We point out that the temperature variation creates an intensity change because the threshold current necessary for lasing is dependent on the SCL temperature. The temperature dependence of the optical frequency and intensity can be approximated by the following linear relationships,

$$\omega(T) = \omega_0 - k_T T, \tag{5.12a}$$

$$I(T) = I_{thr} + \eta_T T, \tag{5.12b}$$

where $k_T = 20\,\mathrm{GHz/C}$ and $\eta_T = 0.15\,\mathrm{mW/C}$. k_T is experimentally determined by scanning the temperature of one SCL while monitoring the intensity through a fixed 2 GHz free spectral range Fabry-Perot etalon. When n number of peaks are observed through the etalon, the proportionality constant can then be determined by the relationship, $k_T = (2\,\mathrm{GHz})\, n/\Delta T$, where ΔT is the scanned temperature. In order to determine η_T, the scanned temperature and the emitted laser light are recorded. The linear relationship can be directly determined from this measurement $\Delta I/\Delta T$.

5.6 Experimental Results

Above the PT-threshold ($|\Delta\omega| > \kappa$), the PT-model and subsequent simulations indicate that the inclusion of a finite time-delay causes global intensity oscillations corresponding to fluctuations in the sign ($\pm$) of λ_R . In order to verify these oscilla-

tions experimentally, we replicate the procedure of scanning the frequency detuning ($\Delta\omega$) while keeping all other parameters constant. The typical experiment involves operating the two SCLs at a constant injection current approximately 3% above their respective threshold values. This guarantees the SCL remains above threshold when the temperature is scanned. The injection current is tuned to a precision of 0.01 mA to ensure that output power of each SCL is identical.

The optical spectrum of the uncoupled (free-running) SCLs are independently measured by an HP 7554 optical spectrum analyser . The temperature to one laser is scanned and recorded. Using Eqn. (5.12a) along with temperature measurements and wavelengths, we calculate the frequency detuning, $\Delta\omega$. The temperature, coupling strength, and the two intensities are simultaneously recorded resulting in an intensity profile. The photo-diode is operated with a large load resistor in order to decrease the bandwidth (< 1 GHz). This bandwidth, along with the scan rate of the oscilloscope, act to time-average the intensity.

Figure 5.6(a) shows the experimental intensity profiles of SCL1 and SCL2 for a cavity length of L = 27 cm ($\tau = 90$). The temperature of SCL2 (blue) is scanned while the intensities are recorded on separate photo-diodes. We normalize the measured intensity with respect to the minimum intensity value in order to contrast the fractional growth of each SCL intensity. For the same parameter values, the simulations and eigenvalues are calculated and depicted in Fig. 5.6(b) and Fig. 5.6(c), respectively. The PT-transition occurs at $|\Delta\omega| \approx \kappa = 0.02$ indicated by the vertical green line in the simulations (Fig. 5.6(b)).

We point out the experiment's excellent agreement with the simulations and PT-model, which depict the global intensity oscillations above the PT-threshold ($|\Delta\omega| > \kappa$). Remember that the global oscillations correspond to the fluctuations of the real components of the eigenvalues (λ_R) in the PT-model, shown in Fig. 5.6(c). These oscillations exist because of the time-delay. We also find the PT-transition near $\Delta\omega \approx 0.05$ in the experimental profile marked by a global increase in the intensity of both SCLs.

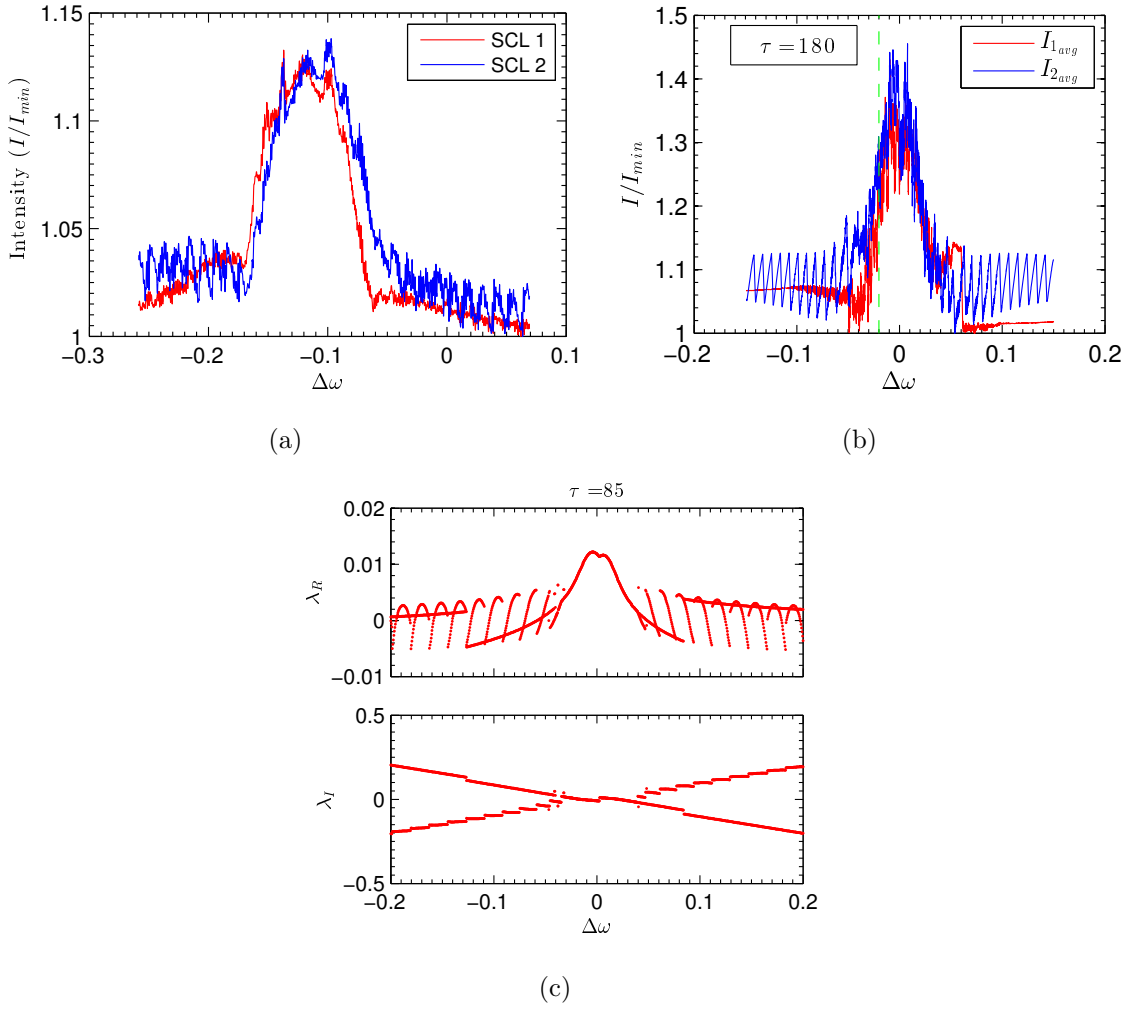

Figure 5.6. Profiles recorded for a cavity length $L = 27\,\text{cm}$, $P_1 = 41.5\,\text{mA}$, $P_2 = 45.1\,\text{mA}$, and VND at 260°

To investigate the effects of the time-delay, we arrange the cavity mirrors (BS1 and BS2) such that the external cavity length is L = 51 cm (τ = 170). It is worth noting that, although the VND is fixed, the coupling strength (κ) varies with the cavity length. This occurs because of the beam expansion, however slight, that is present due to the elliptical beam shape of a SCL. Once more, we fix the coupling strength at κ = 0.02 and vary the frequency detuning $\Delta\omega$ via the temperature to SCL1. The experimental and simulated profiles along with the eigenvalues are shown

in Fig. 5.7. Comparing the experimental intensity profiles in Fig. 5.7 to the previous

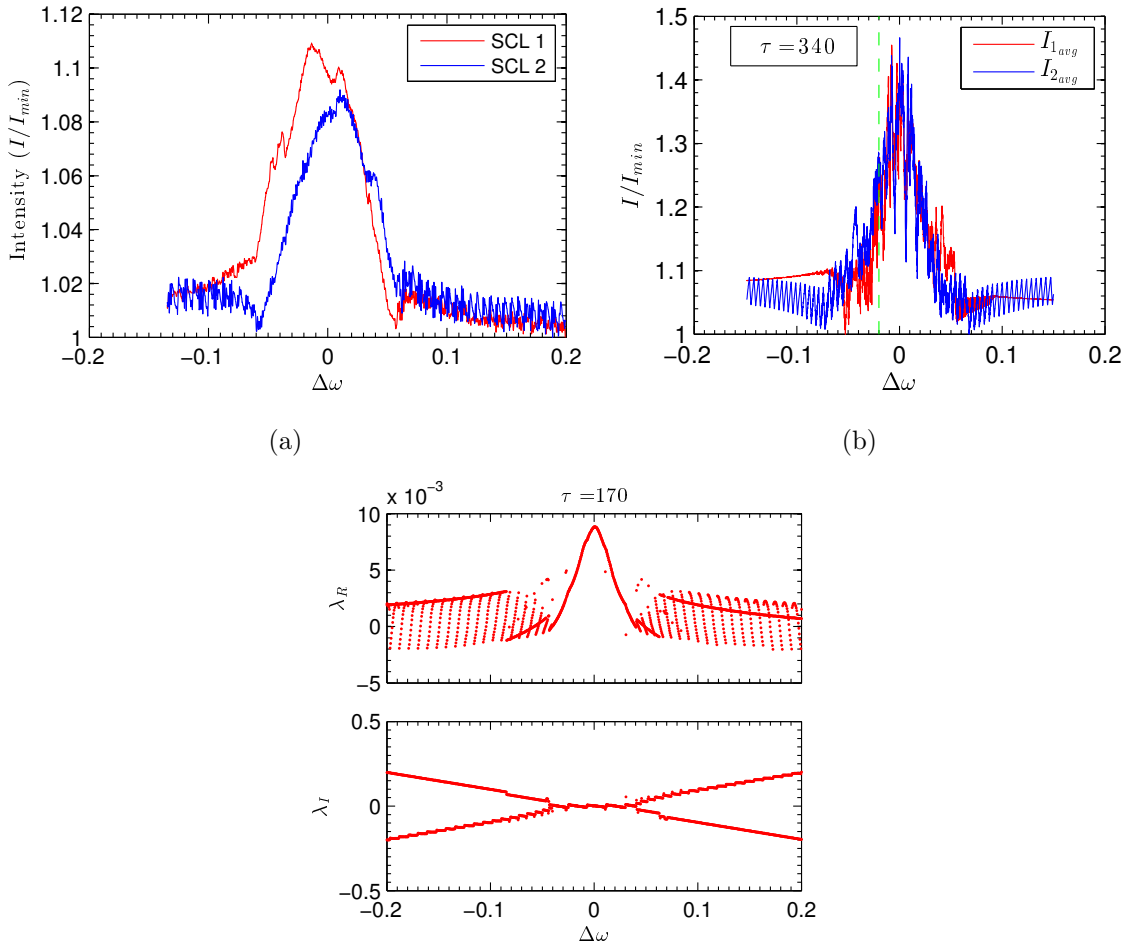

Figure 5.7. Profiles recorded for a cavity length $L = 51\,\text{cm}$, $P_1 = 41.5\,\text{mA}$, $P_2 = 45.1\,\text{mA}$, and VND at 260°

case of a smaller time-delay (Fig. 5.6), we find two clear distinctions.

First, the frequency of the global oscillations increased with an increasing time-delay. This can be observed by comparing the number of oscillations that occur in a given frequency detuning range, for example between $\Delta\omega = 0.05 \rightarrow 0.15$ shown in Fig. 5.6 and Fig. 5.7. The dependence of λ_R on κ, shown in Eqn. (5.11), is quite complex. However, an intuition for the dependence of the oscillations on τ can be

gleaned by examining the eigenvalue evolution shown in Fig. 5.7(c). Above threshold, $|\Delta\omega| > \kappa$, the imaginary eigenvalues (λ_I) vary linearly. λ_R in Eqn. (5.11b) must fluctuate signs ($\pm$) in order to satisfy the equality. The RHS term, $\sin(2(\lambda_I + \theta)\tau)$, varies in sign, therefore the LHS term, $2\lambda_R\lambda_I$, must vary in sign as well. This is possible only if the sign of λ_R changes. In addition, it is clear that the frequency of the RHS term depends linearly on τ.

Second, the amplitude of the oscillations decreases, which can be observed by comparing the two cases, Fig. 5.6 and Fig. 5.7. When $\tau = 180$, the global oscillations vary by approximately 4%, shown in Fig. 5.7, whereas the smaller delay (Fig. 5.6) shows a variance of approximately 8%. These features are manifested in the simulations and eigenvalues, shown in Fig. 5.7(b) and Fig. 5.7(c), respectively. The decrease in amplitude is a consequence of the first difference, i.e. an increase frequency of the global oscillations. As λ_R continues to increase, the amplitude of the intensity follows. This increase continues until a change in sign is required. Thus, a larger $\Delta\omega$ span results in a larger amplitude of the intensity.

Furthermore, this trend continues as the cavity length (time-delay) is increased. We show another example of the intensity profiles and eigenvalues for a cavity length of L = 74 cm ($\tau = 240$). Again, the frequency of the global oscillations increase while the amplitude of the oscillations decrease when the time-delay is larger. Once more, the experiments agree well with the simulations and PT-model shown in Fig. 5.8. In general, these trends continue and we find in the limit of large delay that the eigenvalues converge to the case of zero delay ($\tau = 0$). The relationship between the frequency of oscillations and τ can be experimentally verified up to a distance of $L \approx 150$ m, as beam divergence is unavoidable. An increasingly longer cavity results in larger divergence and a decrease in the coupling strength. When approaching the limit of zero delay ($\tau = 0$), limiting constraints are the size optical components resulting in a minimum cavity length of $L \approx 25$ cm. These constraints can be improved by optically coupling through fiber, but this results in challenges of its own. In the next

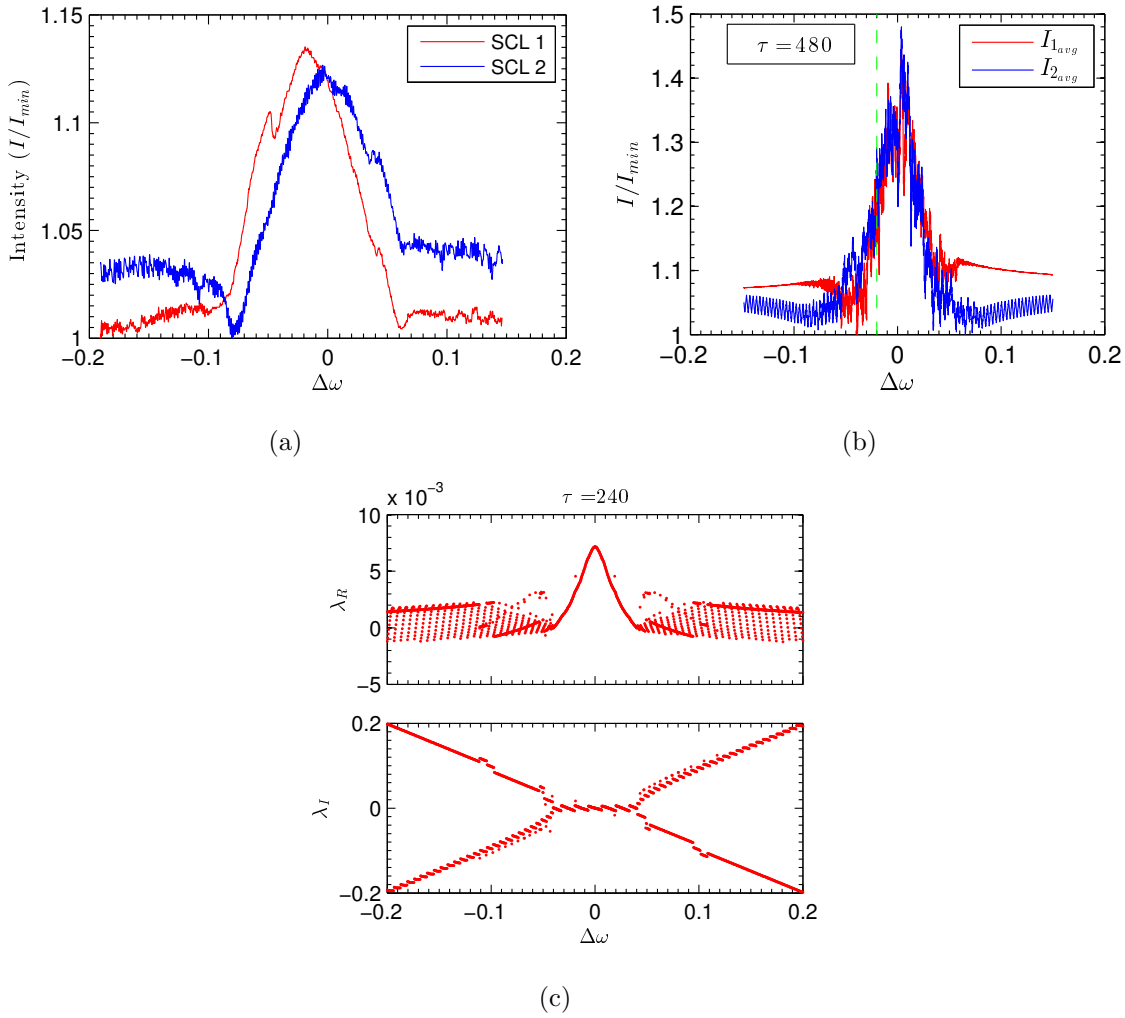

Figure 5.8. Profiles recorded for a cavity length $L = 74\,\text{cm}$, $P_1 = 41.5\,\text{mA}$, $P_2 = 45.1\,\text{mA}$, and VND at 220°

section, we examine an alternative method to elicit the PT-transition by varying the coupling strength while keeping $\Delta\omega$ constant.

5.6.1 Varying the coupling strength

At first glance, the eigenvalues of the system, $\lambda_{1,2} = \pm\sqrt{\kappa^2 - \Delta\omega^2}$, suggests that either PT parameter, κ or $\Delta\omega$, can be varied to induce a PT-transition. We turn our attention to the former case, wherein the coupling strength κ is scanned. To gain an intuition for the difference in this procedure, we show the simulated intensity profiles for zero delay ($\tau = 0$) at five different frequency detunings ($\Delta\omega$). Examining

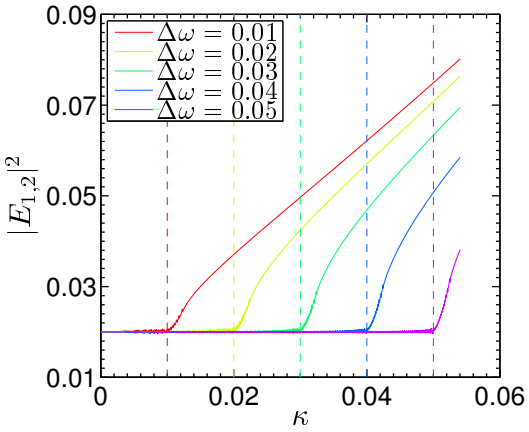

Figure 5.9. Simulated intensity profiles and eigenvalues for varying coupling strenth κ. The solid colored lines in (a) correspond to the intensity profiles which are simulated for five different $\Delta\omega$ of 0.01 (red), 0.02 (yellow), 0.03 (green), 0.04 (blue), and 0.05 (purple). The dashed vertical lines indicate the onset of growth predicted by the PT-symmetric model.

Fig. 5.9, it is clear there is an excellent agreement between the simplified PT model and the simulated rate equations for zero delay. The abrupt growth of the intensity occurs at the predicted PT-symmetric location ($|\Delta\omega| = \kappa$), which is indicated by the vertical dashed lines in Fig. 5.9. We remind the reader that the profiles represent the time-average of the intensity while κ is scanned.

To explore the effects of a finite time-delay, we implement this procedure experimentally such that $\Delta\omega$ is fixed while the coupling strength (κ) is varied via the VND. A third laser (SCL3) is directed through the VND at the same spatial location as

the coupled beam but at different angles. The intensity of SCL3 is recorded. A relationship between the recorded SCL3 intensity through the VND and the fractional coupled power is determined. Intensity profiles are recorded while scanning the parameter κ. Figure 5.10 shows an example of the intensity profiles and eigenvalues for a cavity length of L = 24 cm (τ = 85). The expected PT-transition, $\kappa = |\Delta\omega|$, for

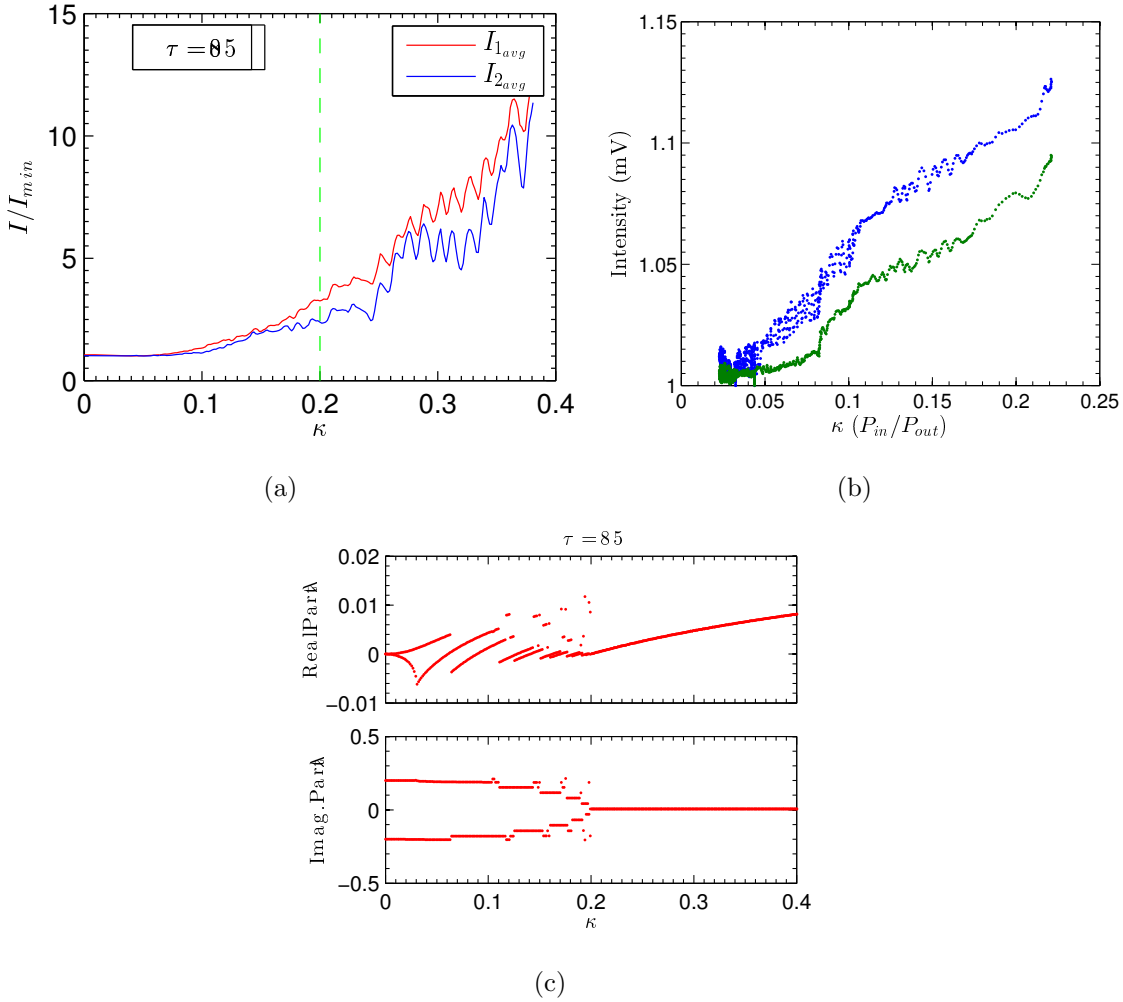

Figure 5.10. Varying κ and keeping $\Delta\omega$ fixed

zero delay is indicated by the vertical (green) dashed line in the simulation profile shown in Fig. 5.10(a). It is clear that the simulated intensities of the SCLs, shown in

Fig. 5.10(a), grow before PT-transition. Figure 5.10(b) shows the experimental profile which agrees well with the simulations. The eigenvalues, shown in Fig. 5.10(c), show that the onset of growth is present at small coupling strengths, which is indicated by the positive values of λ_R.

The discrete steps in Fig. 5.10(c) are distinguished from former eigenvalues when $\Delta\omega$ is scanned. Tracing the evolution of λ_R, it becomes apparent that the sign is not required to change, i.e. moving left to right it is possible for λ_R to remain positive. In addition, the step-size length, measured in terms of κ, changes as κ approaches the frequency detuning, $|\Delta\omega| = 0.2$. Although this is present in the former case, where $\Delta\omega$ is varied, the change is more pronounced.

These differences arise because of the asymmetry introduced by the delay. The time-delay is associated with the coupling term, which is represented by the off-diagonal elements in the matrix notation (Eqn. (5.10). Due to the presence of the eigenvalue, the off-diagonal term is no longer linearly dependent on κ since λ is κ dependent. This gives rise to the non-reciprocal nature of the eigenvalues. In addition, the effects of the time-delay are accounted for in the phase accumulation described by the term $e^{-i\theta\tau}$. This term provides another avenue to explore in future studies. Before discussing future outlooks, we examine the connection between the PT-transition and phase locking/drifting of oscillators, in particular coupled semiconductor lasers.

5.7 PT-transition and Phase Locking

In the case of zero delay ($\tau = 0$), Longhi noted that the PT-transition of a non-linear PT-symmetric dimer is ultimately associated with the phase locking/drifting condition of coupled lasers [94]. To connect the simplified PT-model to the phase locking condition, one can begin by casting the complex electric fields into two components containing a real amplitude and real phase modulation term, which takes the following form,

$$E_{1,2}(t) = A_{1,2}(t)e^{i\phi_{1,2}(t)}. \tag{5.13}$$

After inserting Eqn. (5.13) into the full rate equation model and separating the real and imaginary components, we obtain the time evolution of the phases,

$$\dot{\phi_{1,2}}(t) = \alpha N_{1,2} \mp \Delta\omega + \kappa \frac{A_{2,1}(t-\tau)}{A_{1,2}(t)} \sin(\theta\tau + \phi_{2,1}(t-\tau) - \phi_{1,2}(t)). \tag{5.14}$$

Ultimately, we are interested in the phase locking/drifting condition. This can be determined by finding the parameter space such that the locking condition, $\Delta\dot{\phi} = 0$, is satisfied. Eqn. (5.14) is used in order to write out the time derivative of the phase difference, $\Delta\phi = \phi_1 - \phi_2$,

$$\begin{aligned}\dot{\Delta\phi}(t) = \alpha(N_1 - N_2) - 2\Delta\omega + \kappa \left(\frac{A_2(t-\tau)}{A_1(t)} \sin(\theta\tau + \phi_2(t-\tau) - \phi_1(t)) \right) \\ - \kappa \left(\frac{A_1(t-\tau)}{A_2(t)} \sin(\theta\tau + \phi_1(t-\tau) - \phi_2(t)) \right).\end{aligned} \tag{5.15}$$

We follow a similar approach used to motivate the 2x2 PT-model. We begin by assuming the carrier inversions are negligible ($N_{1,2} \approx 0$), and the time-delay is zero ($\tau = 0$). The lasers operate under identical conditions, which governs the equivalence between the SCLs intensities ($A_1 = A_2$). This drastically simplifies Eqn. (5.15), which reduces to

$$\dot{\Delta\phi}(t) = -2\Delta\omega + 2\kappa \ \sin(\Delta\phi(t)). \tag{5.16}$$

Thus the condition $|\Delta\omega| < \kappa$ must be satisfied for phase locking to occur. We note that Eqn. (5.16) corresponds to the Adler equation for coupled oscillators.

To highlight the effects of phase locking on the dynamics and the connection with the PT-transtion, we examine two cases. All parameters are fixed, and the system evolves in time. Above the PT-threshold, $|\Delta\omega| > \kappa$, we calculate the time-series of the intensities ($I_{1,2}$), phases ($\phi_{1,2}$), and carrier inversions ($N_{1,2}$), which are shown in Fig. 5.11. We point out that *oscillating* intensities ($I_{1,2}$) are identical. The same is true for the time series of the frequency difference $\Delta\dot{\phi}$. The oscillations are anticipated since the eigenvalues above threshold are complex. The relationship between the intensity and carriers are shown in Fig. 5.11, which captures the time dependence of the inversions ($N_{1,2}(t)$) and the exchange of energy between the intensity and inversion, which are $\approx \pi$ out of phase. Below the PT-threshold, $|\Delta\omega| < \kappa$, the phase

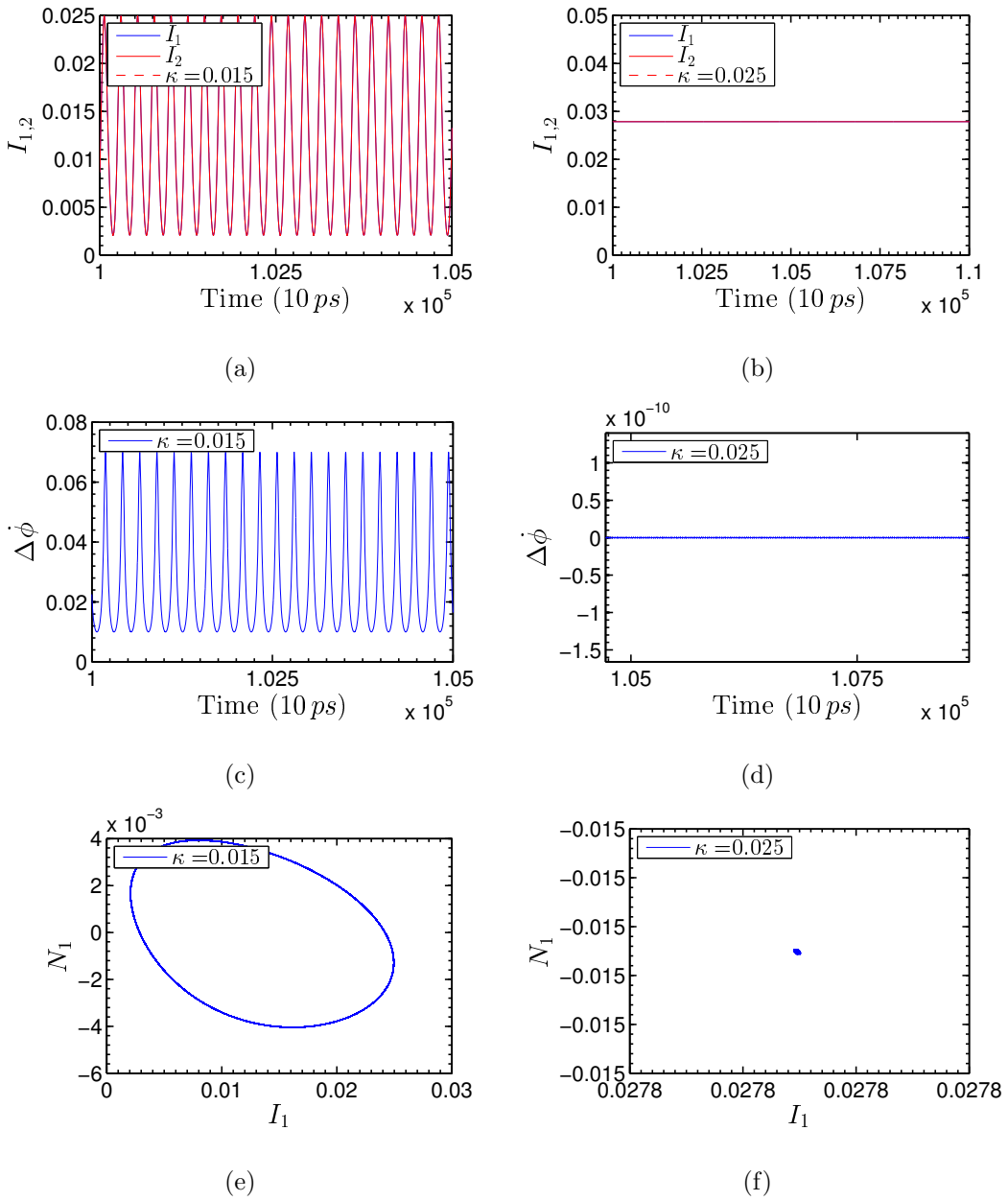

Figure 5.11. Simulated phase plane of the inversion N_1 and intensity I_1, intensity time-series, and phase relationship time-series for identical pump currents ($P_1 = P_2 = 0.012$) and zero delay ($\tau = 0$). All parameters are fixed. The top row corresponds to $|\Delta\omega| = 0.020 > \kappa = 0.015$ and the bottom row when $|\Delta\omega| = 0.020 < \kappa = 0.025$

is locked, indicated by the phase difference ($\Delta\dot{\phi} = 0$) shown in Fig. 5.11(d). The intensities and inversions are constant. All these observations are in good agreement with the Wick-rotated PT-symmetric dimer mentioned in [94], wherein the connection between the PT dimer and Adler equations are discussed.

In order to bring us one step closer to the experimental design, we scan the frequency mismatch $\Delta\omega$ but keep all other parameters fixed including the pump currents at $P_1 = P_2 = 0.012$. Once more, we examine two time-scales in the dynamics; one is the fast dynamics which show the frequency oscillations, and the second is the steady-state behavior, which is found by calculating a moving time-average. Since the experiment setup places a limit on both the detector speed and bandwidth of the oscilloscope, the time average is the observed experimental phenomenon. We show this behavior in the simulated intensity, inversion, and phase profiles for this configuration in Fig. 5.12, where the blue profile corresponds to the fast dynamics and the red profile the time average. As mentioned, κ is fixed at a value of 0.02, hence we expect oscillations when $|\Delta\omega| > \kappa$ and a phase locking/constant intensity when $|\Delta\omega| < \kappa$. This is clearly depicted in Fig. 5.12 where the vertical red line corresponds to the PT-symmetry breaking point. Moving from left to right, after this location the phase is locked ($\Delta\dot{\phi} = 0$) and the intensity does not oscillate, rather there is a growth in the intensity. This growth occurs because of the additional photons from the coupled SCL. This is also represented by the depletion of the inversion ($N_{1,2} < 0$) in Fig. 5.12(b). Although the eigenvalues are not shown, we have performed this analysis and it accurately captures the movement from the imaginary plane to the real plane at the expected PT-transition.

To ensure that condition $|\Delta\omega| = \kappa$ arises because of bi-direction coupling, we examine the extreme case of uni-directional coupling, referred to as injection. Using similar rate equations to those outlined in Section 2, one can show the condition, $\sqrt{1+\alpha^2}\sqrt{P_x/P_L}$, must be satisfied for steady-state solutions to exist. In the case of injection, $|\nu|$ is the is frequency difference between the master laser and slave laser. P_x and P_L are the intensities the master and slave, respectively. Hence, the mechanism

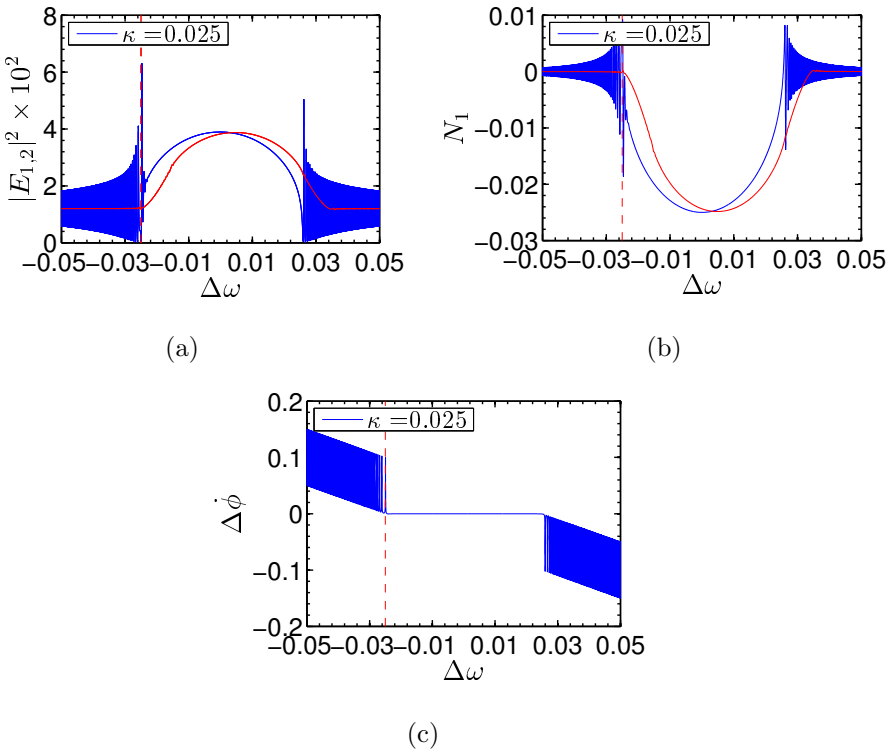

Figure 5.12. Simulated intensity profiles for fixed pump currents ($P_1 = P_2 = 0.015$) when only the frequency mismatch $\Delta\omega$ is scanned from -0.05 to 0.05. The intensity, inversion, and phase profiles are simulated for a coupling strength, $\kappa = 0.025$. The red vertical line represents the theoretical $\mathcal{PT}$transition.

for phase locking is different when considering optical injection. For injection, one must take into account the dependence of the intrinsic coupling between the amplitude and phase of light which is expressed by the α-parameter. In practice this implies that the phase locking occurs at larger frequency detuning $\Delta\omega$ compared to the coupled oscillator model. When considering the coupled model, a dependence on α exists when the carrier inversions are no longer equal ($N_1 \neq N_2$), which can be seen in Eqn. (5.15). As their difference ($N_1 - N_2$), the first term containing α becomes significant. We discuss these effects in the next Section.

5.8 Pump Current Variation

It is important to examine our initial experimental procedure, wherein the pump current (in contrast to temperature) was modified to one of the SCLs. This procedure provides a parameter space where the PT-model accurately describes the experimental phenomenon and where the approximations used to arrive at the simplified model breakdown. This section introduces the experimental procedure and compares the results with the simulations and PT-model. We show what parameters lead to the breakdown of the model and discuss their relevance to the previous sections.

The scanned pump current induces changes in the emitted laser intensity and optical frequency. The dependence of the intensity and frequency on the adjusted pump current (ΔP), is given by Eqns. (5.17),

$$\omega(\Delta P) = \omega_0 - k\Delta P, \tag{5.17a}$$

$$I(\Delta P) = I_{thr} + \eta_s \Delta P, \tag{5.17b}$$

where ω_0 is the frequency at threshold, and ΔP is the pump current with the threshold pump current subtracted. The slopes are intrinsic characteristics of the SCL, and were determined to be $k = 1.84\,\mathrm{GHz/mA}$ and $\eta_s = 0.55\,\mathrm{mW/mA}$. The variations in the optical frequency were a desired effect since, ultimately, we wanted to control the frequency difference ($\Delta\omega$) between the two lasers. However, the intensity changes proved problematic. In order for the PT-symmetry breaking condition to hold, the intensities of the two SCLs need to be approximately equal ($I_1 \approx I_2$).

Fig. 3.2 shows a set of typical results for two different coupling strengths of (a) $\kappa = 0.0027$ and (b) $\kappa = 0.014$. In Fig. 3.2, SCL1 is operated at 2% above threshold and SCL2 is initially at 30% above threshold. The frequency detuning is large compared to the coupling strength ($|\Delta\omega| > \kappa$). The pump current to SCL2 is then decreased slowly (< 10 Hz) from $P_2 = 1.3$ to $P_2 = 0.8$, consequently decreasing the frequency mismatch $\Delta\omega$. Figure 5.13 depicts the experimental and simulated intensities of both lasers intensities, Int_1 (blue) and Int_2 (green), as the pump current P_2 is decreased. We show two cases for different coupling strengths to highlight the excellent agreement

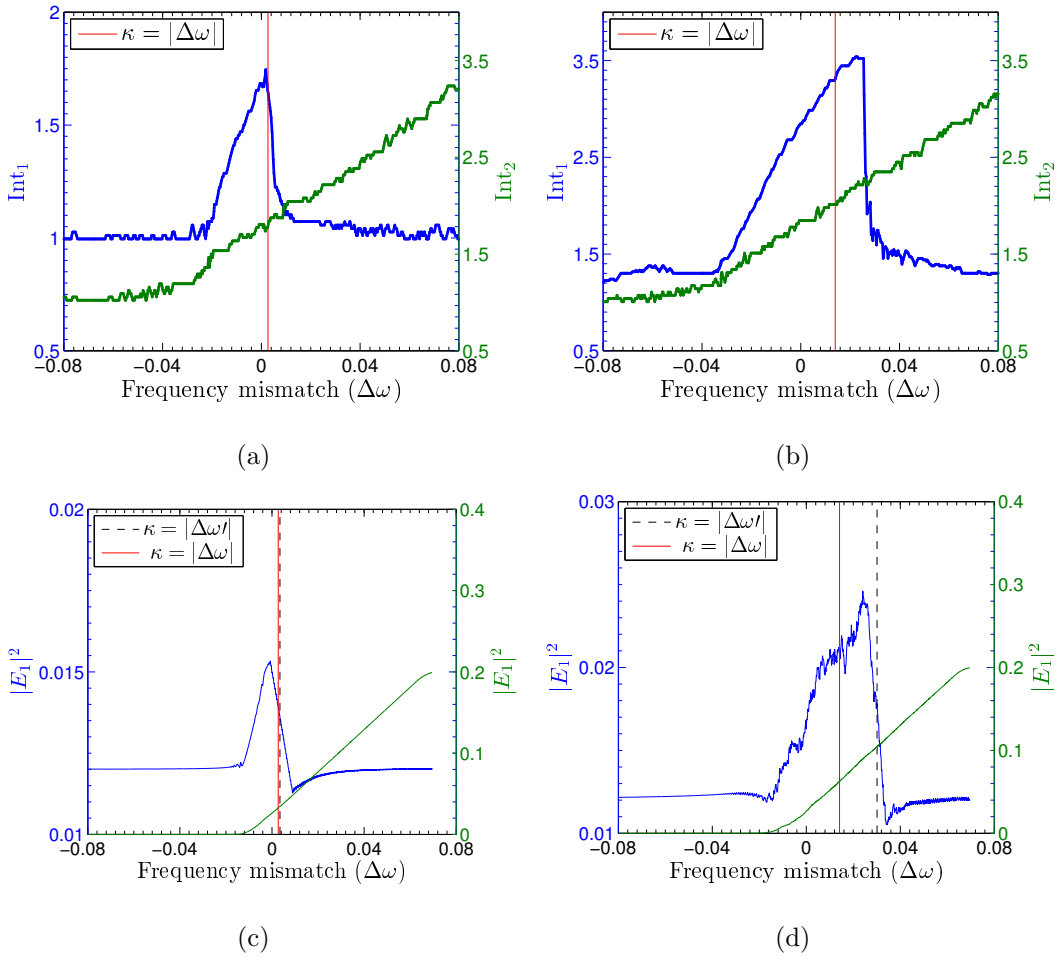

Figure 5.13. Experimental (top row) and numerical (bottom row) intensities of SCL1 (blue) and SCL2 (green) when the coupling strength is $\kappa = 0.0027$ (a,c) and $\kappa = 0.014$ (b,d). The pump current P_2 is decreased from $P_2 = 1.3$ to $P_2 = 0.8$. The vertical lines indicated the location when $\Delta\omega = \kappa$ (black dashed) and when phase breaking occurs $\dot{\phi}(t) = \Delta\omega' \neq 0$ (red solid).

between theory and experiment and to demonstrate the parameter window where the system accurately mimics a PT-symmetric model. Examining Fig. 5.13, it is clear that as P_2 is decreased, the intensity of SCL2 decreases and the intensity of SCL1 remains constant until a critical pump current is reached when a sudden growth of intensity occurs. This abrupt increase in intensity marks the PT-threshold. In order

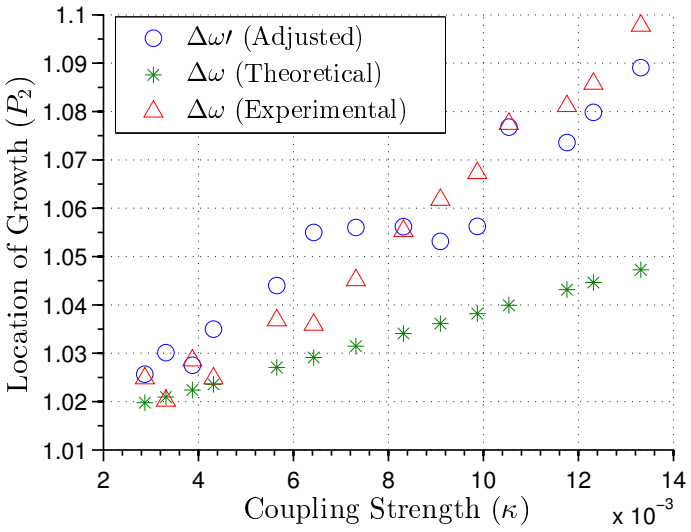

Figure 5.14. Experimental plot of the pump current value where the onset of growth begin for increasing coupling strength κ values, which are marked with red diamonds. The blue circles correspond to the simulated location where phase locking is broken ($\dot{\phi}(t) \neq 0$). The green stars represent the theoretical PT-transition ($\kappa = |\Delta\omega|$).

to determine the phase breaking location, shown in Fig. 5.13(c) with the black dashed line, we first calculated the phase which is extracted from the complex electrics fields $E_{1,2}(t)$. The time derivative of the phase difference is calculated and we find when this value is no longer zero ($\Delta\dot{\phi}(t) \neq .0$). This data agrees well with the experiments shown in Fig. 5.13(a). Finally, Fig. 5.14 also shows the predictions of the simplified model, and it is clear that while the agreement is good at low coupling strengths, there is a marked departure from the experiments and the predictions of the full model at higher coupling strengths. It is, however, remarkable, that the full model contains within it the PT-symmetric behavior information despite the full model not being the typical PT-symmetric model.

We note that as κ becomes small ($\kappa \to 0$) an experimental determination of the injection current at which there is an abrupt intensity growth becomes harder to detect because the magnitude of the intensity growth is too small detect. Hence, we

are not able to check the exact convergence of the experimental and numerical results at very small couplings. Since the numerical calculations are performed without quantum noise, the PT-phase transition is easily detected in the simulation and is manifested as an onset of growth in the intensity profile. Although the deviation from the simplified theoretical PT-model appears when the coupling strength is large, the presence of an EP is predictable at larger couplings because we have been able to ignore the time delay between the SCLs. This approximation was valid because we were interested in the global behavior ($E_{1,2}(t) = E_{1,2}(t-\tau)$) before the onset of growth and the implemented procedure produces rapid variations in the phase accumulation $\theta\tau$ which are averaged out and hence have little affect on the onset of intensity growth.

There are a couple of important observations that one can make here - (i) for weak coupling, the PT-threshold is reached when the intensities of SCL1 and SCL2 are equal, whereas for stronger coupling the intensities are not equal at the PT-threshold, (ii) increasing the coupling strength increases the frequency detuning at which the PT-threshold occurs. Qualitatively, at this point, the results suggest that the PT-threshold is strongly effected by the strength of the optical coupling.

We now examine the eigenvalues of a modified PT-model that includes the affects of a non-zero inversion ($N_{1,2} \neq 0$). To obtain the eigenvalues shown in Eqn.(5.18),

$$\Delta\omega^2 - \kappa^2 e^{-2\lambda\tau+2i\theta\tau} + \lambda^2 - \alpha^2 N^2 + 2i\alpha N^2 + N^2 - 2i\alpha\lambda N - 2\lambda N = 0, \qquad (5.18)$$

the full set of rate equations were solved as J_2 was scanned from $1.3J_{thr}$ to $0.8J_{thr}$ and the array of $N_{1,2}$ values were stored. These values of $N_{1,2}$ were then inserted into the rate equations for the electric fields at each step, n, that corresponds to a decrease in the pump current P_2. At each step of $P_2(n)$, the complex eigenvalues are determined and stored. After scanning the pump current P_2, a complete map of the eigenvalues is produced, shown in Fig. 5.15, which displays both eigenvalues $\lambda_{1,2}$ along the real and imaginary plane. Figure 5.15(a) shows the eigenvalues when the feedback strength is $\kappa = 0.0027$, and the color spectrum along each step corresponds to the pump current $P_2(n)$ at that location. We start by examining the evolution of each eigenvalue $\lambda_{1,2}$ individually shown in Fig. 5.15. We remind the reader that this figure represents the

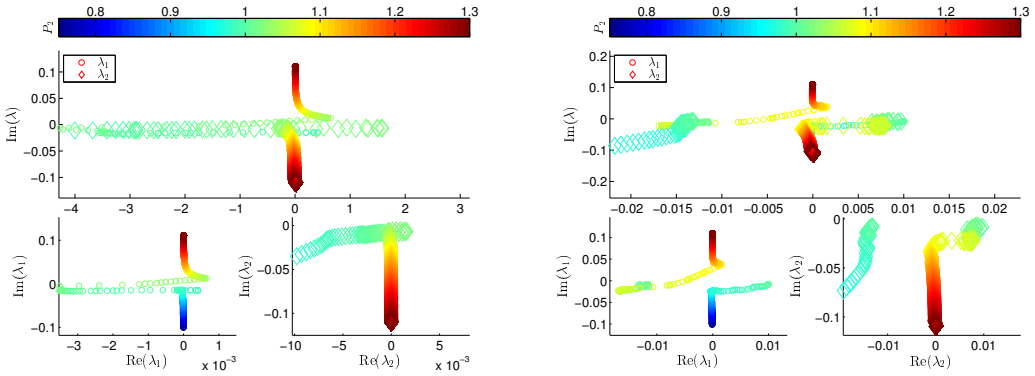

(a) (b)

Figure 5.15. Same parameters as Fig. 5.13. Evolution of eigenvalues for the two coupling strength $\kappa = 0.003$ (a) and $\kappa = 0.017$ (b). The color profile corresponds to the pump current P_2 which is directly proportional to the frequency mismatch $\Delta\omega$. Each eigenvalue, λ_1 and λ_2, is shown depicted separately in (a2,b2) and (a3,b3), respectively, and the superposition is found in (a1,b1). Note that the avoided crossing in (a), which occurs for a pump current of $P_1 \approx 1.05$, occurs at $\lambda \approx 0$, thus indicating PT-symmetry breaking.

eigenvalues movement for the experimental and simulated profiles shown in Fig. 5.15 and Fig. 5.13(c), respectively.

Initially λ_1 (a2) is purely imaginary ($Im(\lambda_1) \approx 0.01$ and $Re(\lambda_1) \approx 0$), which corresponds to oscillatory behavior of the intensity. Since we are taking a time average these oscillations are smoothed out resulting in the steady-state behavior shown in Fig. 5.5a,c. As the pump current decreases, $Im(\lambda_1)$ decreases while the real part remains zero ($Re(\lambda_1) \approx 0$). At the critical value when $\kappa = |\Delta\omega|$, λ_1 becomes real and $Re(\lambda_1)$ suddenly increases while the imaginary component is negligible ($Im(\lambda_1) \approx 0$), which corresponds to the abrupt growth in the intensity. At this point, the PT-symmtery is broken because the carrier densities become non-negligible. One sees this by continuing to trace this evolution, where $Re(\lambda_1)$ becomes negative and eventually returns to zero ($Re(\lambda_1) = 0$). We note that Fig. 3.3c follows a similar trajectory except the eigenvalue λ_2 begins at a purely negative value. Figure 3.3(a1), which is

a superposition of the two plots Fig. 3.3(a2,a3), shows an avoided crossing which is typical of exceptional point (EP) behaviors. The EP occurs at the PT-symmetric location $\lambda_{1,2} = 0$.

Turning our attention to Fig. 3.3b, which is produced when the coupling strength is $\kappa = 0.014$, it is clear that the avoided crossing is still present, however the location of the EP is slightly shifted from the PT-breaking transition ($\lambda_{1,2} = 0$). The abrupt change in λ_2, shown in Fig. 3.3b3, occurs at a complex value, i.e. λ_2 has a non-zero real component, rather than a purely imaginary value. This highlights our observation that the PT-symmetric model (Eq. (5.5)) is valid for small feedback strengths κ. The shift in the EP from the PT-symmetric case is a result of the non-negligible carrier densities. Since the coupling strength is large, the expected intensity growth should occur at a larger pump current P_2. The larger values of P_2 and κ creates an asymmetry between the carrier densities ($N_1 \neq N_2$) and $N_1 > 0$. Therefore, the approximations used to obtain the simplified model are no longer valid and Eq. (5.6) no longer reduces to the PT model. However, it is interesting to note that even at larger coupling strengths ($\kappa > 0.004$), the avoided crossing, which is typical of EP behavior, continues to be present.

5.9 Conclusion

This chapter discussed the experimental realization of PT-symmetry breaking in time-delayed optically coupled SCLs. Even with a time-delay, the system retained the signatures of a PT-transition which were predicted by the modified PT-model. The model we developed incorporated the delayed field by augmenting the standard PT-model with a delayed term. The delayed term was included in the off diagonal term, or coupling term, of the 2x2 model. We examined the unique features that emerged because of the delay. In particular, the eigenvalues underwent discrete jumps as the PT parameters were continuously scanned. We showed that the discrete jumps in the real part of the eigenvalues were manifested as global intensity oscillations in the

unbroken region. This unexpected result was confirmed by simulating the intensities of the SCLs using the full rate equations model. In addition, we showed that the frequency of the global oscillations depended linearly on the magnitude of the time-delay. Overall, we highlighted the excellent features that coupled SCLs offer as a test-bed for future PT studies, and possible avenues to explore which only a delayed system can offer.

6. Summary

This dissertation describes our investigations on the nonlinear dynamics that arise in a semiconductor laser due to optical feedback. We implemented two schemes of optical feedback. The first scheme subjects the laser to optical feedback from two external cavities (or two loops), wherein each cavity contains a spectral filter. We referred to this as two filtered optical feedback (FOF). Using two FOF, we experimentally demonstrate the ability to elicit and control unique dynamics in the optical emission frequency (wavelength) of the laser. We observe frequency oscillations whose period primarily depends on a weighted average of the individual time-delays from each cavity. The "weight" is determined by the ratio of feedback strength from each cavity. These results are confirmed by a deterministic model describing the temporal dynamics of the complex electric field and carrier density of the laser. In addition, an analytic expression can be found which confirms the frequency dependence on the feedback strength. We find that the period of the frequency oscillations are associated with the filtered external cavity modes of the system. It would be worthwhile to determine a more precise relationship between the elicited frequency oscillations and cavity modes. This would allow one to understand all the significant parameters that influence the period of oscillations.

We theoretically observe a period doubling route in the frequency dynamics as the bifurcation parameter (feedback strength) is increased from one cavity. We attempted to trace this route experimentally, but discovered a quantitative difference between the deterministic simulations and experiments for the feedback strength required to induce chaotic dynamics. This motivated us to determine the influence of quantum noise on the period doubling route. We use a stochastic model which is a set of coupled rate equations that include the effects of spontaneous emission and shot noise. One of the more surprising results is that a larger feedback strength is required

in order to induce chaotic dynamics. We find that noise drives the system toward stable attractors. In the presence of noise, the effects of the time-delay on the periodic dynamics are more pronounced. In addition, we examine the influence of noise when the bandwidth of the filters are changed. These results help quantify the bandwidth regimes in which noise plays a significant role in determining the final dynamical state. In particular, when the bandwidth of the filter is larger than the RO frequency, RO dominate the dynamics and the effects of noise are negligible.

The second scheme consists of two time-delayed, optically coupled semiconductor lasers. We demonstrate that coupled SCLs are an excellent test-bed to study parity (P) and time-reversal (T) symmetry breaking. Not only did optically coupled SCLs capture many of the characteristic signatures of PT symmetry breaking, but the time-delay between the lasers introduces novel and surprising features. We develop a simple PT model that includes the effects of the time-delay. The PT model is analogous to a 2x2 Hamiltonian in which the off-diagonal terms account for the coupling between lasers, and the diagonal terms account for the intrinsic dynamics of each laser. By examining the eigenvalues of the PT model, we can predict the global behavior of the SCLs intensities by scanning the PT parameter, i.e. the frequency difference between the lasers. The imaginary and real eigenvalues correspond to oscillations and growth (or decay), respectively, in the intensity of the laser. We experimentally observe intensity oscillations and intensity growth by scanning the temperature of one SCL while recording the intensity of each SCL. The experimental intensity profiles show excellent agreement with the movement of the eigenvalues that were predicted by the PT model. In addition, we find agreement with the full rate equation model that includes the dynamics of the carrier inversion and optical field.

The time-delayed PT model also provides viable avenues which have yet to be experimentally explored. We indicated some of these avenues in Chapter 5, but highlight some of the most promising. In particular, the ability to control the phase accumulation of the coupled fields allows one to vary the off-diagonal elements of the 'Hamiltonian' from real to purely imaginary. This could effectively control the non-

Hermicity of the Hamiltonian. The effects of the time-delay on the optical frequency have yet to be experimentally observed. A larger window of the time-delay (cavity lengths) can be explored by changing the current free-space design to a fiber in which the attenuation of the field amplitude is comparatively much smaller.

REFERENCES

REFERENCES

[1] Jeff Hecht. Short history of laser development. *Optical Engineering*, 49(9):091002–091002–23, 2010.

[2] R. N. Hall, G. E. Fenner, J. D. Kingsley, T. J. Soltys, and R. O. Carlson. Coherent light emission from gaas junctions. *Phys. Rev. Lett.*, 9:366–368, Nov 1962.

[3] Nick Holonyak and S. F. Bevacqua. Coherent (visible) light emission from ga(as1xpx) junctions. *Applied Physics Letters*, 1(4), 1962.

[4] Remembering the laser diode. *Nature Photonics*, 6(12):795–795, nov 2012.

[5] G.P. Agrawal and N.K. Dutta. *Semiconductor Lasers*. Springer US, 1993.

[6] Jt Verdeyen. Laser electronics. *Laser electronics/2nd edition/, by JT Verdeyen, ...*, pages 1–9, 1995.

[7] C. Henry. Theory of the linewidth of semiconductor lasers. *IEEE Journal of Quantum Electronics*, 18(2):259–264, Feb 1982.

[8] Daan Lenstra. Relaxation oscillation dynamics in semiconductor diode lasers with optical feedback. *IEEE Photonics Technology Letters*, 25(6):591–593, 2013.

[9] R. Broom, E. Mohn, C. Risch, and R. Salathe. Microwave self-modulation of a diode laser coupled to an external cavity. *IEEE Journal of Quantum Electronics*, 6(6):328–334, Jun 1970.

[10] T. Morikawa, Y. Mitsuhashi, J. Shimada, and Y. Kojima. Return-beam-induced oscillations in self-coupled semiconductor lasers. *Electronics Letters*, 12(17):435–436, August 1976.

[11] I. Ikushima and M. Maeda. Self-coupled phenomena of semiconductor lasers caused by an optical fiber. *IEEE Journal of Quantum Electronics*, 14(5):331–332, May 1978.

[12] R. O. Miles, A Dandridge, A. B. Tveten, H. F. Taylor, and T. G. Giallorenzi. Feedback-induced line broadening in cw channel-substrate planar laser diodes. *Applied Physics Letters*, 37(11):990, 1980.

[13] L. Goldberg, H.F. Taylor, A. Dandridge, J.F. Weller, and R.O. Miles. Spectral Characteristics of Semiconductor Lasers with Optical Feedback. *IEEE Transactions on Microwave Theory and Techniques*, 30(4):401–410, 1982.

[14] K. Vahala. Observation of relaxation resonance effects in the field spectrum of semiconductor lasers. *Applied Physics Letters*, 42(3):211, 1983.

[15] J.H. Osmundsen, B. Tromborg, and H. Olesen. Experimental investigation of stability properties for a semiconductor laser with optical feedback. *Electronics Letters*, 19(25-26):1068, 1983.

[16] Y. C. Chen. Phase noise characteristics of single mode semiconductor lasers with optical feedback. *Applied Physics Letters*, 44(1):10, 1984.

[17] D. Lenstra, B. Verbeek, and A. Den Boef. Coherence collapse in single-mode semiconductor lasers due to optical feedback. *IEEE Journal of Quantum Electronics*, 21(6):674–679, jun 1985.

[18] R. Lang and K. Kobayashi. External optical feedback effects on semiconductor injection laser properties. *IEEE Journal of Quantum Electronics*, 16(3):347–355, Mar 1980.

[19] R. Tkach and A. Chraplyvy. Regimes of feedback effects in 1.5 μm distributed feedback lasers. *Journal of Lightwave Technology*, 4(11):1655–1661, Nov 1986.

[20] S. Donati and R. H. Horng. The diagram of feedback regimes revisited. *IEEE Journal of Selected Topics in Quantum Electronics*, 19(4):1500309–1500309, July 2013.

[21] Konosuke Aoyama, Ryuichi Yoshioka, Nobuhide Yokota, Wataru Kobayashi, and Hiroshi Yasaka. Experimental demonstration of linewidth reduction of laser diode by compact coherent optical negative feedback system. *Applied Physics Express*, 7(12):122701, 2014.

[22] Konosuke Aoyama, Ryuichi Yoshioka, Nobuhide Yokota, Wataru Kobayashi, and Hiroshi Yasaka. Optical Negative Feedback for Linewidth Reduction of Semiconductor Lasers. *IEEE Photonics Technology Letters*, 27(4):340–343, feb 2015.

[23] W. Liang, V. S. Ilchenko, D. Eliyahu, a. a. Savchenkov, a. B. Matsko, D. Seidel, and L. Maleki. Ultralow noise miniature external cavity semiconductor laser. *Nature Communications*, 6:7371, 2015.

[24] Thomas B. Simpson, Jia Ming Liu, Mohammad Almulla, Nicholas G. Usechak, and Vassilios Kovanis. Linewidth sharpening via polarization-rotated feedback in optically injected semiconductor laser oscillators. *IEEE Journal on Selected Topics in Quantum Electronics*, 19(4), 2013.

[25] Thomas B. Simpson, Jia Ming Liu, Mohammad Almulla, Nicholas G. Usechak, and Vassilios Kovanis. Limit-cycle dynamics with reduced sensitivity to perturbations. *Physical Review Letters*, 112(2), 2014.

[26] Jun-Ping Zhuang and Sze-Chun Chan. Tunable photonic microwave generation using optically injected semiconductor laser dynamics with optical feedback stabilization. *Optics letters*, 38(3):344–6, 2013.

[27] Jun-Ping Zhuang and Sze-Chun Chan. Phase noise characteristics of microwave signals generated by semiconductor laser dynamics. *Optics Express*, 23(3):2777, 2015.

[28] Jian-Wei Wu, Bikash Nakarmi, and Yong Hyub Won. Optically tunable microwave, millimeter-wave and submillimeter-wave utilizing single-mode Fabry-Pérot laser diode subject to optical feedback. *Optics Express*, 24(3):2655, feb 2016.

[29] Atsushi Uchida, Kazuya Amano, Masaki Inoue, Kunihito Hirano, Sunao Naito, Hiroyuki Someya, Isao Oowada, Takayuki Kurashige, Masaru Shiki, Shigeru Yoshimori, Kazuyuki Yoshimura, and Peter Davis. Fast physical random bit generation with chaotic semiconductor lasers. *Nature Photonics*, 2(12):728–732, nov 2008.

[30] Thomas E. Murphy and Rajarshi Roy. Chaotic lasers: The world's fastest dice. *Nature Photonics*, 2(12):714–715, dec 2008.

[31] M Sciamanna and K A Shore. Physics and applications of laser diode chaos. *Nature Photonics*, 9(3):151–162, 2015.

[32] Claudio R. Mirasso, Pere Colet, and Priscila García-Fernández. Synchronization of chaotic semiconductor lasers: Application to encoded communications. *IEEE Photonics Technology Letters*, 8(2):299–301, 1996.

[33] S Sivaprakasam and K a Shore. Demonstration of optical synchronization of chaotic external-cavity laser diodes. *Optics letters*, 24(7):466–8, 1999.

[34] I Fischer, Y Liu, and P Davis. Synchronization of chaotic semiconductor laser dynamics on subnanosecond time scales and its potential for chaos communication. *Physical Review A*, 62(1):art. no.–011801, 2000.

[35] C. Masoller. Anticipation in the synchronization of chaotic semiconductor lasers with optical feedback. *Physical Review Letters*, 86(13):2782–2785, 2001.

[36] S Tang and J M Liu. Experimental verification of anticipated and retarded synchronization in chaotic semiconductor lasers. *Physical review letters*, 90(19):194101, 2003.

[37] Anbang Wang, Yuncai Wang, and Hucheng He. Enhancing the bandwidth of the optical chaotic signal generated by a semiconductor laser with optical feedback. *IEEE Photonics Technology Letters*, 20(19):1633–1635, 2008.

[38] Neus Oliver, Thomas Jüngling, and Ingo Fischer. Consistency Properties of a Chaotic Semiconductor Laser Driven by Optical Feedback. *Physical Review Letters*, 114(12):123902, mar 2015.

[39] Hiroyuki Someya, Isao Oowada, Haruka Okumura, Takahiko Kida, and Atsushi Uchida. Synchronization of bandwidth-enhanced chaos in semiconductor lasers with optical feedback and injection. *Optics Express*, 17(22):19536, 2009.

[40] A Locquet, F Rogister, M Sciamanna, P Mégret, and M Blondel. Two types of synchronization in unidirectionally coupled chaotic external-cavity semiconductor lasers. *Physical review. E, Statistical, nonlinear, and soft matter physics*, 64:4, 2001.

[41] Y. Liu, Y. Takiguchi, P. Davis, T. Aida, S. Saito, and J. M. Liu. Experimental observation of complete chaos synchronization in semiconductor lasers. *Applied Physics Letters*, 80(23):4306–4308, 2002.

[42] Apostolos Argyris, Dimitris Syvridis, Laurent Larger, Valerio Annovazzi-Lodi, Pere Colet, Ingo Fischer, Jordi García-Ojalvo, Claudio R. Mirasso, Luis Pesquera, and K. Alan Shore. Chaos-based communications at high bit rates using commercial fibre-optic links. *Nature*, 438(7066):343–346, nov 2005.

[43] Mirvais Yousefi and Daan Lenstra. Dynamical behavior of a semiconductor laser with filtered external optical feedback. *IEEE Journal of Quantum Electronics*, 35(6):970–976, 1999.

[44] A. P A Fischer, Mirvais Yousefi, D. Lenstra, Michael W. Carter, and Gautam Vemuri. Experimental and theoretical study of semiconductor laser dynamics due to filtered optical feedback. *IEEE Journal on Selected Topics in Quantum Electronics*, 10(5):944–954, 2004.

[45] Alexis P. a. Fischer, Mirvais Yousefi, Daan Lenstra, Michael W. Carter, and Gautam Vemuri. Filtered Optical Feedback Induced Frequency Dynamics in Semiconductor Lasers. *Physical Review Letters*, 92(2):023901, 2004.

[46] H. Erzgräber, D. Lenstra, B. Krauskopf, A. P. A. Fischer, and G. Vemuri. Feedback phase sensitivity of a semiconductor laser subject to filtered optical feedback: Experiment and theory. *Physical Review E*, 76(2):026212, aug 2007.

[47] Hartmut Erzgräber and Bernd Krauskopf. Dynamics of a filtered-feedback laser: influence of the filter width. *Optics Letters*, 32(16):2441, aug 2007.

[48] Hartmut Erzgräber, Bernd Krauskopf, and Daan Lenstra. Bifurcation Analysis of a Semiconductor Laser with Filtered Optical Feedback. *SIAM Journal on Applied Dynamical Systems*, 6(1):1–28, jan 2007.

[49] Song-Sui Li and Sze-Chun Chan. Chaotic Time-delay Signature Suppression in a Semiconductor Laser with Frequency-detuned Grating Feedback. *IEEE Journal of Selected Topics in Quantum Electronics*, PP(99):1–1, 2015.

[50] George Gray and Rajarshi Roy. Noise in nearly-single-mode semiconductor lasers. *Physical Review A*, 40(5):2452–2462, 1989.

[51] Mirvais Yousefi, Daan Lenstra, and Gautam Vemuri. Nonlinear dynamics of a semiconductor laser with filtered optical feedback and the influence of noise. *Physical review. E, Statistical, nonlinear, and soft matter physics*, 67(4 Pt 2):046213, 2003.

[52] V. Pal, J.S. Suelzer, A. Prasad, G. Vemuri, and R. Ghosh. Semiconductor laser dynamics with two filtered optical feedbacks. *IEEE Journal of Quantum Electronics*, 49(3):340–349, 2013.

[53] Miguel C. Soriano, Jordi García-Ojalvo, Claudio R. Mirasso, and Ingo Fischer. Complex photonics: Dynamics and applications of delay-coupled semiconductors lasers. *Rev. Mod. Phys.*, 85:421–470, Mar 2013.

[54] Alexander Többens and Ulrich Parlitz. Dynamics of semiconductor lasers with external multicavities.

[55] M.W. Lee, P. Rees, K.A. Shore, S. Ortin, L. Pesquera, and A. Valle. Dynamical characterisation of laser diode subject to double optical feedback for chaotic optical communications. *IEE Proceedings - Optoelectronics*, 152(2):97, 2005.

[56] A N Pisarchik and F R Ruiz-Oliveras. Dynamics of a Semiconductor Laser with Two External Cavities. *PIERS ONLINE*, 3(4), 2007.

[57] Ning Jiang, Wei Pan, Lianshan Yan, Bin Luo, Shuiying Xiang, Lei Yang, and Di Zheng. Isochronal chaos synchronization of semiconductor lasers with multiple time-delayed couplings. *Journal of the Optical Society of America B*, 28(5):1139, may 2011.

[58] Shui Ying Xiang, Wei Pan, Ai Jun Wen, Nian Qiang Li, Li Yue Zhang, Lei Shang, and Hui Xing Zhang. Conceal Time Delay Signature of Chaos in Semiconductor Lasers With Dual-Path Injection. *IEEE Photonics Technology Letters*, 25(14):1398–1401, jul 2013.

[59] Lina Jaurigue, Oleg Nikiforov, Eckehard Schöll, Stefan Breuer, and Kathy Lüdge. Dynamics of a passively mode-locked semiconductor laser subject to dual-cavity optical feedback. *Physical Review E*, 93(2):022205, feb 2016.

[60] David Orrell and Leonard A Smith. Visualizing bifurcations in high dimensional systems: the spectral bifurcation diagram. *International journal of bifurcation and chaos*, 13(10):3015–3027, 2003.

[61] Joseph S Suelzer, Awadhesh Prasad, Rupamanjari Ghosh, and Gautam Vemuri. Effects of quantum noise on the nonlinear dynamics of a semiconductor laser subject to two spectrally filtered, time-delayed optical feedbacks. *Optics Communications*, 370:209–221, 2016.

[62] PIOTR SŁOWIŃSKI, Bernd Krauskopf, and Sebastian Wieczorek. Mode structure of a semiconductor laser with feedback from two external filters. *Discrete & Continuous Dynamical Systems-Series B*, 20(2), 2015.

[63] Jade Martínez-Llinàs, Xavier Porte, Miguel C. Soriano, Pere Colet, and Ingo Fischer. Dynamical properties induced by state-dependent delays in photonic systems. *Nature Communications*, 6:7425, jun 2015.

[64] P. Slowiski, B. Krauskopf, and S. Wieczorek. Mode structure of a semiconductor laser with feedback from two external filters. pages 69971K–69971K–8, apr 2008.

[65] P Slowiski, B Krauskopf, and S Wieczorek. Solution structure and dynamics of a semiconductor laser subject to feedback from two external filters. In *Proc. SPIE*, volume 7720, pages 77200K–77200K–11, 2010.

[66] Rebecca L Honeycutt. Stochastic runge-kutta algorithms. i. white noise. *Physical Review A*, 45(2):600, 1992.

[67] C Masoller. Numerical investigation of noise-induced resonance in a semiconductor laser with optical feedback. *Physica D: Nonlinear Phenomena*, 168:171–176, 2002.

[68] Thomas Erneux, Geertje Hek, Mirvais Yousefi, and Daan Lenstra. The injection laser limit of lasers subject to optical feedback. In *Photonics Europe*, pages 303–311. International Society for Optics and Photonics, 2004.

[69] Carl M. Bender and Stefan Boettcher. Real spectra in non-hermitian hamiltonians having pt symmetry. *Phys. Rev. Lett.*, 80:5243–5246, Jun 1998.

[70] Carl M. Bender, Dorje C. Brody, and Hugh F. Jones. Complex extension of quantum mechanics. *Phys. Rev. Lett.*, 89:270401, Dec 2002.

[71] Carl M. Bender, Daniel W. Hook, Peter N. Meisinger, and Qing-hai Wang. Complex correspondence principle. *Phys. Rev. Lett.*, 104:061601, Feb 2010.

[72] G. Scolarici and L. Solombrino. On the pseudo-hermitian nondiagonalizable hamiltonians. *Journal of Mathematical Physics*, 44(10), 2003.

[73] Dorje C Brody. Consistency of pt-symmetric quantum mechanics. *Journal of Physics A: Mathematical and Theoretical*, 49(10):10LT03, 2016.

[74] Ali Mostafazadeh. Pseudo-hermiticity versus pt symmetry: The necessary condition for the reality of the spectrum of a non-hermitian hamiltonian. *Journal of Mathematical Physics*, 43(1), 2002.

[75] Christian E Rüter, Konstantinos G Makris, Ramy El-Ganainy, Demetrios N Christodoulides, Mordechai Segev, and Detlef Kip. Observation of parity–time symmetry in optics. *Nature Physics*, 6(3):192–195, 2010.

[76] Tsampikos Kottos. Optical physics: Broken symmetry makes light work. *Nature Physics*, 6(3):166–167, 2010.

[77] Alois Regensburger, Christoph Bersch, Mohammad-Ali Miri, Georgy Onishchukov, Demetrios N Christodoulides, and Ulf Peschel. Parity-time synthetic photonic lattices. *Nature*, 488(7410):167–171, 2012.

[78] J. T. Cole, K. G. Makris, Z. H. Musslimani, D. N. Christodoulides, and S. Rotter. Twofold $\mathcal{PT}$ symmetry in doubly exponential optical lattices. *Phys. Rev. A*, 93:013803, Jan 2016.

[79] Nicolas X. A. Rivolta and Bjorn Maes. Symmetry recovery for coupled photonic modes with transversal pt symmetry. *Opt. Lett.*, 40(16):3922–3925, Aug 2015.

[80] Hamidreza Ramezani, Tsampikos Kottos, Vassilios Kovanis, and Demetrios N. Christodoulides. Exceptional-point dynamics in photonic honeycomb lattices with $\mathcal{PT}$ symmetry. *Phys. Rev. A*, 85:013818, Jan 2012.

[81] Martin Wimmer, Alois Regensburger, Mohammad-Ali Miri, Christoph Bersch, Demetrios N Christodoulides, and Ulf Peschel. Observation of optical solitons in pt-symmetric lattices. *Nature communications*, 6, 2015.

[82] Liang Feng, Zi Jing Wong, Ren-Min Ma, Yuan Wang, and Xiang Zhang. Single-mode laser by parity-time symmetry breaking. *Science*, 346(6212):972–975, 2014.

[83] Hui Jing, S. K. Özdemir, Xin-You Lü, Jing Zhang, Lan Yang, and Franco Nori. $\mathcal{PT}$-symmetric phonon laser. *Phys. Rev. Lett.*, 113:053604, Jul 2014.

[84] Hossein Hodaei, Mohammad-Ali Miri, Matthias Heinrich, Demetrios N. Christodoulides, and Mercedeh Khajavikhan. Parity-time–symmetric microring lasers. *Science*, 346(6212):975–978, 2014.

[85] Chong Yidong. Nonlinear optics: asymmetry from symmetry. *Nature Physics*, 10(5):336–337, 2014.

[86] Jun John Sakurai and Jim Napolitano. *Modern quantum mechanics*. Addison-Wesley, 2011.

[87] Josep Mulet, Cristina Masoller, and Claudio R Mirasso. Modeling bidirectionally coupled single-mode semiconductor lasers. *Physical Review A*, 65(6):063815, 2002.

[88] Javier M Buldú, Raúl Vicente, Toni Pérez, Claudio R Mirasso, MC Torrent, and J Garcıa-Ojalvo. Periodic entrainment of power dropouts in mutually coupled semiconductor lasers. *Applied physics letters*, 81(27):5105–5107, 2002.

[89] H Erzgräber, D Lenstra, B Krauskopf, E Wille, M Peil, I Fischer, and W Elsäßer. Mutually delay-coupled semiconductor lasers: Mode bifurcation scenarios. *Optics communications*, 255(4):286–296, 2005.

[90] Cristian Bonatto, Bryan Kelleher, Guillaume Huyet, and Stephen P. Hegarty. Transition from unidirectional to delayed bidirectional coupling in optically coupled semiconductor lasers. *Phys. Rev. E*, 85:026205, Feb 2012.

[91] Leandro Junges and Jason AC Gallas. Stability diagrams for continuous wide-range control of two mutually delay-coupled semiconductor lasers. *New Journal of Physics*, 17(5):053038, 2015.

[92] Yasutoshi Takeuchi, Rui Shogenji, and Junji Ohtsubo. Chaotic dynamics in semiconductor lasers subjected to polarization-rotated optical feedback. *Applied Physics Letters*, 93(18), 2008.

[93] W. Fader. Theory of two coupled lasers. *IEEE Journal of Quantum Electronics*, 21(11):1838–1844, Nov 1985.

[94] Stefano Longhi. Phase transitions in wick-rotated pt-symmetric optics. *Annals of Physics*, 360:150–160, 2015.

[95] Jonathan Erwin Forde. *Delay differential equation models in mathematical biology*. PhD thesis, The University of Michigan, 2005.

[96] H.-J. Wünsche, S. Bauer, J. Kreissl, O. Ushakov, N. Korneyev, F. Henneberger, E. Wille, H. Erzgräber, M. Peil, W. Elsäßer, and I. Fischer. Synchronization of delay-coupled oscillators: A study of semiconductor lasers. *Phys. Rev. Lett.*, 94:163901, Apr 2005.

[97] R. Lang. Injection locking properties of a semiconductor laser. *IEEE Journal of Quantum Electronics*, 18(6):976–983, Jun 1982.

[98] F. Mogensen, H. Olesen, and G. Jacobsen. Locking conditions and stability properties for a semiconductor laser with external light injection. *IEEE Journal of Quantum Electronics*, 21(7):784–793, Jul 1985.

VITA

VITA

The youngest of three boys, Joseph (Joe) was born in 1984 to Phillip and Phyllis Suelzer in Fort Wayne Indiana. He spent most of his childhood playing outside, building various contraptions out of legos, or "making" up games with friends. It was not uncommon to hear such questions as, "what is at the end of the universe?" posed by his father at the dinner table, in which the boys chimed in their answer.

Throughout primary school, Joe enjoyed all of his courses. His aptitude for and interest in mathematical subjects began to emerge in secondary school. Upon graduating high school, he remained in Fort Wayne to enroll at Indiana-Purdue University Fort Wayne (IPFW) as an engineer major. After his second year, he switched his major from engineering to physics, and his fascination for the subject never waned. He began research with Dr. Mark Masters, who encouraged him to present and publish his work. It was in Dr. Master's AMO lab that Joe got his first taste of the joys and pains of scientific research.

During his time at IPFW, he and his brother (Jerry) started a screen printing business which proved to be an essential experience for both of them. After graduating from IPFW, Joe met his (future) wife, Deanna Rose, who "required" tutoring for her math course. Joe spent the next 1.5 years helping run the business, substitute teaching, and performing research in Dr. Master's lab. Although the business experienced much success, Joe and his brother knew that different vocations were awaiting them. Jerry took on the poverty asked of him to become a brother of the Church, while Joe took on the poverty asked of him by graduate school.

A little over 6.5 years after starting graduate school, still filled with gratitude and wonder at what was given to him and his wife (now four children), Joe defended his PhD on April 12th 2016. His next adventure awaits him in Dayton, Ohio where he begins a NRC postdoc at the Air Force Research Laboratory.